

CHARGE-INDUCED ACTUATION IN CARBON NANOTUBES AND RESISTANCE
CHANGES IN CARBON NANOTUBE NETWORKS

By

JENNIFER ANN SIPPEL-OAKLEY

A DISSERTATION PRESENTED TO THE GRADUATE SCHOOL
OF THE UNIVERSITY OF FLORIDA IN PARTIAL FULFILLMENT
OF THE REQUIREMENTS FOR THE DEGREE OF
DOCTOR OF PHILOSOPHY

UNIVERSITY OF FLORIDA

2005

Copyright 2005

by

Jennifer Ann Sippel-Oakley

To my parents, Richard and Cynthia Sippel

ACKNOWLEDGMENTS

I would like to extend my deepest gratitude to my advisor, Dr. Andrew Rinzler. He has an amazing amount of enthusiasm for the pursuit of knowledge in the field of carbon nanotubes. He was always encouraging throughout the course of a frustrating and difficult experiment. As a teacher, he was patient and thorough. For these things I am extremely grateful. His support and encouragement are the reason I am receiving this degree. If I could make the same choice over again I would not hesitate to pick him as my advisor.

I would also particularly like to thank former group members Dr. Zhihong Chen and Dr. Amol Patil for close collaboration and friendship during our graduate careers. Additionally I am grateful to current and former group members Dr. Hidenori Tashiro, Jacob Alldredge, Zhuangchun Wu, Lex Kemper, Daniel Ranken, Daniel Barrow and Jonathon Logan.

I owe thanks to Dr. Art Hebard for use of laboratory equipment and also for always being a friendly and helpful resource. Thanks are due to Hung-Ta Wang, Byoung Sam Kang, Dr. Fan Ren and Dr. Steve Pearton for collaboration on the nanotube hydrogen sensor.

Many thanks go to my parents, Rick and Cindy Sippel, who have always supported me in all aspects of my life. I am eternally grateful for that and for their unconditional love.

Finally I would like to thank my husband, Garrett Oakley. He is a fellow scientist and a great dancer. His love and support have guided and uplifted me during my graduate career.

TABLE OF CONTENTS

	<u>page</u>
ACKNOWLEDGMENTS	iv
LIST OF TABLES	viii
LIST OF FIGURES	ix
ABSTRACT	xii
 CHAPTER	
1 INTRODUCTION	1
2 CARBON NANOTUBE BACKGROUND.....	3
2.1 Growth Methods of Carbon Nanotubes	3
2.2 Carbon Nanotube Structure.....	4
3 MOTIVATION AND THEORY FOR INDIVIDUAL CARBON NANOTUBE ACTUATION	11
3.1 Electromechanical Actuation	11
3.2 Macro-Scale Carbon Nanotube Actuators	11
3.3 Bond Length Changes in Intercalated Graphite.....	13
3.4 Theoretical Work for Bond Length Changes in Carbon Nanotubes.....	17
4 PREPARATION OF AND EXPERIMENTAL MEASUREMENTS ON SUSPENDED CARBON NANOTUBE SAMPLES.....	22
4.1 Fabrication of Suspended Carbon Nanotube Structures	22
4.1.1 Substrate Preparation	23
4.1.2 Carbon Nanotube Deposition and Growth.....	24
4.1.2.1 Deposition of Laser Ablation Grown Nanotubes from Solution	24
4.1.2.2 Chemical Vapor Deposition Grown Nanotubes	27
4.1.3 Electrode Patterning.....	29
5.1.4 Etching	33
5.1.5 Release Procedure.....	34

	4.1.6 Identification of Suspended Nanotubes	37
	5.1.7 Final Sample Preparations	38
	4.2 Experimental Procedure.....	39
5	RESULTS AND DISCUSSION OF CHARGE INDUCED ACTUATION OF SUSPENDED CARBON NANOTUBES.....	51
	5.1 Results of Actuation Measurements	51
	5.2 Discussion of Results.....	58
6	CONDUCTANCE CHANGES IN CARBON NANOTUBES DUE TO HYDROGEN	66
	6.1 Carbon Nanotube Sensor Background.....	66
	6.2 Carbon Nanotube Sensor Fabrication	69
	6.3 Resistance Changes from Metal Deposition	72
	6.4 Conductance Changes due to Hydrogen Exposure	76
	6.4.1 Pure SWCNT Samples.....	76
	6.4.2 SWCNT Samples Coated with Sputtered Pd	78
	6.4.3 SWCNT Samples Coated with Thermally Evaporated Pd.....	80
	6.4.4 Thin Pd Film	82
	6.4.5 Conclusion	82
APPENDIX	SPECTROELECTROCHEMICAL STUDY OF CARBON NANOTUBE THIN FILMS.....	84
	A.1 Carbon Nanotube Experiment.....	85
	A.2 Experimental Section	87
	A.3 Results and Discussion.....	88
	A.4 Conclusions	89
	LIST OF REFERENCES	91
	BIOGRAPHICAL SKETCH	96

LIST OF TABLES

<u>Table</u>	<u>page</u>
4-1 Resistance before and after processing steps	36
5-1 Summary of data from sample 1	53
5-2 Summary of data for sample 2.	55
5-3 Summary of all data from sample 3	56
6-4 Summary of the actuator data.....	58
6-1 Resistance changes of nanotube samples with sputtered Pd	72
6-2 Resistance changes on SWCNT films with thermally evaporated Pd	73
6-3 Conductance changes in sputtered Pd/SWCNT	80

LIST OF FIGURES

<u>Figure</u>	<u>page</u>
2-1 Hexagonal graphite lattice showing the unit vectors \mathbf{a}_1 and \mathbf{a}_2 .	7
2-2 Unit cells of graphite.	8
3-1 Macro-scale actuator.	12
3-2 Strain values for bucky paper actuators films versus applied potential.	13
3-3 Strain versus charge transfer curve for graphite.	15
4-1 Actuation experimental setup.	23
4-2 Aligned carbon nanotubes from Triton-X solution	26
4-3 Nanotubes on silicon.	28
4-4 Metal deposition on resists.	29
4-5 Scope trace of electrodes.	30
4-6 Nanotubes after lithography	32
4-7 Processing steps for suspended carbon nanotube samples.	35
4-8 Suspended carbon nanotube images.	37
4-9 Map of the created marks.	38
4-10 Cross sectional schematic of chip mounted on AFM puck.	40
4-11 Free-space drift of a bare tip and a paralyne coated tip in aqueous 1M NaNO ₃	43
4-12 Identifying mark created in the SEM	43
4-13 Force calibration curves against two surfaces.	47
4-14 Illustration of a force calibration curve against a hard surface and nanotube.	48
4-15 Nanotube under tension.	49

4-16	Plot of δy versus y for $L_0=430\text{nm}$ and $\delta L/L=0.0001$.	50
5-1	Nanotube sample 1.	52
5-2	Sample 1 data.	52
5-3	Nanotube sample 2.	54
5-4	Sample 2 data	54
5-5	Nanotube sample 3.	55
5-6	Sample 3 data	56
5-7	Data of the Z Movement and applied voltage while the AFM was suspended in free space	57
5-8	Data of Z Movement and applied voltage while the AFM tip was in contact with the bottom of the trench.	57
5-9	Hydrated Cl^- and Na^+ ions	60
5-10	Density of states for a (10,11) SWCNT.	63
6-1	Electrode pattern on micro-device nanotube sensor.	69
6-2	Nanotube thin films	70
6-3	SWCNT thin film sensor wired for measurement	71
6-4	Pd coated nanotube films	75
6-5	Micro-sensor device current vs. time measurement.	77
6-6	7nm film current vs. time measurement.	77
6-7	25nm film current vs. time measurements.	78
6-8	Micro-device sensor coated with sputtered Pd current vs. time measurements.	79
6-9	7nm film with sputtered Pd current vs. time measurements	79
6-10	25nm film with sputtered Pd current vs. time measurements.	80
6-11	7nm film with thermally evaporated Pd current vs. time measurement.	81
6-12	Thin Pd film current vs. time measurements.	82
A-1	Spectroelectrochemical cell	86

A-2	Fermi Level of a semiconducting (12,8) SWCNT	87
A-3	Percent Transmittance vs. Wavelength for SWCNT thin-film at various positive applied potentials.....	89
A-4	Percent Transmittance vs. Wavelength for SWCNT thin-film at various negative applied potentials.....	90

Abstract of Dissertation Presented to the Graduate School
of the University of Florida in Partial Fulfillment of the
Requirements for the Degree of Doctor of Philosophy

CHARGE-INDUCED ACTUATION OF SUSPENDED CARBON NANOTUBES AND
RESISTANCE CHANGES IN CARBON NANOTUBE NETWORKS

By

Jennifer A. Sippel-Oakley

May 2005

Chair: Andrew G. Rinzler
Major Department: Physics

In 1999 it was demonstrated that macroscopic films comprised of single wall carbon nanotubes exhibited dimensional changes with charge injection onto the films. A fundamental mechanism was proposed for this effect related to the dimensional changes observed in graphite intercalation complexes upon charge transfer doping with the intercalant species. The major fraction of this thesis concerns experiments at the single nanotube level designed to test the validity of this mechanism. The metals compatible with our fabrication processes inevitably p-dope the nanotubes resulting in smaller dimensional changes. Additionally, there are contact barriers that prevent the injection of electrons onto the nanotubes. Although the proposed mechanism may still be responsible for the results seen in the nanotube films, the effect is too small to be consistently measured in individual nanotubes.

The conductivity of a carbon nanotube can be varied by exposure to various chemicals having utility in chemical sensing applications. We use thin films of carbon

nanotubes to exploit this effect. The films are made sensitive to hydrogen by association with palladium metal. Such sensors operate at room temperature with very low power dissipation of ~ 0.25 mV.

CHAPTER 1 INTRODUCTION

Carbon nanotubes are quasi one-dimensional structures with the high mechanical strength of graphite and have the useful attribute of occurring in either semiconducting or metallic variants. These qualities have caused an explosion of research since their discovery in the soot of fullerene production by Ijima¹ in 1991. These first nanotubes were multi-walled carbon nanotubes (MWCNTs) consisting of at least two graphene cylinders nested one within the next.

This discovery prompted efforts to produce single wall carbon nanotubes (SWCNTs) and prompted much theoretical effort on the properties of such tubes. The addition of metal catalyst particles to the carbon starting material was found to be the key and production of SWCNTs was first established by Bethune *et al.*² and Ijima and Ichihashi³ in 1993. All the nanotubes used in our work were SWCNTs.

In a standard description, a carbon nanotube is a graphene sheet rolled into a seamless cylinder. As the name implies, the nanotubes have a diameter around a nanometer. In general, they have a length of a few microns but there have been recent reports of nanotubes with lengths of up to centimeters.⁴ Much of the fascination with nanotubes arises from the fact that they can be either semiconducting or metallic depending on the orientation the hexagonal graphene lattice relative to the nanotube axis. Coupled with this property is the extremely high Young's modulus (1 TPa)⁵ and tensile strength (estimated at 45 GPa)^{6,7} of nanotubes. They are also stable at high temperatures and show strong resistance to most chemicals.

Our study addresses two specific effects in carbon nanotubes that could lead to useful applications. One proposed application for carbon nanotubes is electromechanical actuators. In 1999, a carbon nanotube film showed dimensional changes with charge injection.⁸ This behavior was attributed to an effect seen in intercalated graphite compounds whereby the carbon-carbon bond length is modified by charge transfer to graphite's π orbital system. The first part of this thesis describes efforts to observe dimensional changes due to charge injection in an individual nanotube and determine if the proposed mechanism was really responsible for the effect seen in the nanotube films.

Conductance of nanotubes can be manipulated by the interaction with other molecular species. This led to the second focus of our study, resistance changes in nanotube films as a way of hydrogen detection. Nanotube films were made sensitive to hydrogen by the addition of palladium particles and H_2 levels as low as 10 ppm were detected.

CHAPTER 2 CARBON NANOTUBE BACKGROUND

2.1 Growth Methods of Carbon Nanotubes

As the interest in carbon nanotube research grew, so did the need for increased quantities of high-quality nanotubes. Several methods were developed for their production. The first method is arc-discharge or carbon arc. In this setup, two carbon rods are used as electrodes with a small separation (about 1mm) and a high dc current is passed between them while in a helium atmosphere. The high currents passing between the carbon electrodes ignite plasma of the helium gas, and temperatures exceed 3000°C. Carbon is evaporated from the anode and then condenses to form nanotubes. This method can be used to grow MWNT or SWNT if a metal catalyst (usually a transition metal) is added to the carbon electrode. The high temperatures at which growth occurs ensure high-quality nanotubes with few defects. However, many byproducts (such as fullerenes) and amorphous carbons are produced and must be removed by purification.

The second method of nanotube growth is laser ablation (first demonstrated by Thess *et al.*).⁹ This was the first method to produce nanotubes on the scale of several grams per run. Early work in the actuation project and all work with nanotube sensors used SWCNTs grown by this process. With this method, a pulsed laser is used to vaporize a graphite target within a heated tube furnace (temp 1100-1200°C). To achieve SWNT growth metal catalyst material is mixed with the graphite target. A flow of inert gas carries the nanotubes downstream to a cooled copper collector. This method also requires purification to remove the byproducts generated during growth. Both the arc-

discharge method and laser ablation method form nanotubes that tend to be aggregated in ropes (several nanotubes bundled together by van der Waals forces). Although vigorous sonication of solutions containing these nanotubes can help break up the bundles, it is difficult to isolate individual nanotubes using material from these growth processes.

This leads to the next method of growing nanotubes: chemical vapor deposition (CVD). Most nanotubes used to measure nanotube actuation were grown by CVD. The method involves placing a sample with metal catalysts into a furnace (growth temperatures between 500-1000°C) and flowing a carbon feedstock gas (usually a hydrocarbon gas) over the sample. The presence of the metal catalysts causes the dissociation of the hydrocarbon feedstock gas. The metal particles become supersaturated with carbon and precipitate nanotubes. It has been found by transmission electron microscopy (TEM) that the nanotube diameter corresponds to the diameter of the catalyst particles.¹⁰ Catalyst islands can even be lithographically patterned onto silicon substrates for more controlled placement of the nanotube growth.¹¹

A fourth growth method (developed recently) involves decomposition of carbon monoxide at high pressures (between 1 and 10 atm) and is commonly referred to as HiPCO.¹² Catalyst particles are provided by the thermal decomposition of iron pentacarbonyl $\text{Fe}(\text{CO})_5$ which produces iron clusters in the gas phase. This process produces tubes with smaller average diameters and less variation than tubes produced by the first three methods.

2.2 Carbon Nanotube Structure

Carbon nanotubes were predicted to be either semiconducting or metallic in 1992 soon after their discovery.^{13,14,15} However, this was only verified experimentally 6 years

later by scanning tunneling microscopy (STM)^{16,17}. Many techniques (such as STM, TEM and scanning electron microscopy) have verified nanotube structure as that of a seamless graphene-like cylinder. STM has proved a useful tool to study nanotubes since it can reveal a nanotube's chirality.

This section gives some basic background on the physical and resulting electronic structure of SWCNTs. The treatment here is a summary of that developed by Saito *et al.* in Chapter 3 of reference 18. Nanotubes are most easily described by their chiral vector, \mathbf{C}_h .

$$\mathbf{C}_h = n\mathbf{a}_1 + m\mathbf{a}_2 \quad (2-1)$$

The chiral vector denotes the circumference of the nanotube and connects two crystallographically equivalent sites on the planar graphite sheet. In other words, a nanotube can be envisioned as the cylinder formed from rolling up a sheet of graphene by connecting the tip to the tail of the chiral vector. As shown in Figure 2-1, the vectors \mathbf{a}_1 and \mathbf{a}_2 are two non-orthogonal unit vectors, the combination of which can span any point on the hexagonal graphite lattice and have the following relations

$$\mathbf{a}_1 \cdot \mathbf{a}_1 = \mathbf{a}_2 \cdot \mathbf{a}_2 = a^2, \quad \mathbf{a}_1 \cdot \mathbf{a}_2 = a^2/3 \quad (2-2)$$

where $a = 1.44\text{\AA} \times 3^{1/2} = a_{C-C} \times 3^{1/2}$. a is the lattice constant of the graphite sheet and a_{C-C} is the carbon-carbon bond distance. In x and y coordinates, the real-space unit vectors are represented by $\mathbf{a}_1 = (3^{1/2}a/2, a/2)$ and $\mathbf{a}_2 = (3^{1/2}a/2, -a/2)$. Thus the diameter of the nanotube is given by

$$d_t = L/\pi = (\mathbf{C}_h \cdot \mathbf{C}_h)^{1/2}/\pi = 3^{1/2}a_{C-C}(m^2 + mn + n^2)^{1/2}/\pi \quad (2-3)$$

The translation vector \mathbf{T} is orthogonal to \mathbf{C}_h and parallel to the nanotube axis. It is the shortest repeat distance along the axis. It is defined to be the unit vector of a nanotube and is represented as

$$\mathbf{T} = t_1 \mathbf{a}_1 + t_2 \mathbf{a}_2 \quad (t_1 \text{ and } t_2 \text{ are integers}) \quad (2-4)$$

Since \mathbf{T} and \mathbf{C}_h are orthogonal by definition, we use $\mathbf{C}_h \cdot \mathbf{T} = 0$ to calculate t_1 and t_2 .

$$\begin{aligned} (n\mathbf{a}_1 + m\mathbf{a}_2) \cdot (t_1\mathbf{a}_1 + t_2\mathbf{a}_2) &= (2n + m)t_1 + (2m + n)t_2 = 0 \\ t_1 &= (2m + n)/d_R \quad t_2 = -(2n + m)/d_R \end{aligned} \quad (2-5)$$

where d_R is the greatest common divisor of $(2m + n)$ and $(2n + m)$. Introducing d as the greatest common divisor of n and m gives d_R as

$$\begin{aligned} d_R &= d \text{ if } n-m \text{ is not a multiple of } 3d \\ &= 3d \text{ if } n-m \text{ is a multiple of } 3d \end{aligned} \quad (2-6)$$

The unit cell of a nanotube is the rectangle defined by the vectors \mathbf{T} and \mathbf{C}_h . The number of hexagons contained in this unit cell is determined by the area of the unit cell ($|\mathbf{C}_h \times \mathbf{T}|$) divided by the area of a hexagon ($|\mathbf{a}_1 \times \mathbf{a}_2|$) and is given in terms of (n,m) by the equation

$$N = 2(m^2 + nm + n^2)/d_R \quad (2-7)$$

Each hexagon contains two carbon atoms, so the total number of carbon atoms in the nanotube unit cell is thus $2N$.

The construction of the nanotube along with its electrical properties is completely determined by the indices (n,m) . Nanotubes are grouped into three categories: zigzag, armchair, and chiral. Both zigzag and armchair nanotubes have special symmetry directions and earn their name from the pattern of the chain of carbon atoms around the circumference. Zigzag nanotubes are those with one of the indices equal to zero, either $(n,0)$ or $(0,m)$. Armchair nanotubes have identical indices, (n,n) . They are both achiral, meaning that the structure of the mirror image is identical to that of the original. Chiral nanotubes are those that fall anywhere between the two types. The chiral angle θ represents the tilt of the hexagons with respect to the nanotube axis. Figure 2-1 shows see that θ can be found by taking the dot product of \mathbf{C}_h and \mathbf{a}_1 .

$$\cos \theta = \mathbf{C}_h \cdot \mathbf{a}_1 / |\mathbf{C}_h| |\mathbf{a}_1| = (2n + m) / 2(n^2 + nm + m^2)^{1/2} \quad (2-8)$$

Zigzag nanotubes have $\theta = 0^\circ$, armchair have $\theta = 30^\circ$, and chiral fall anywhere in between that range.

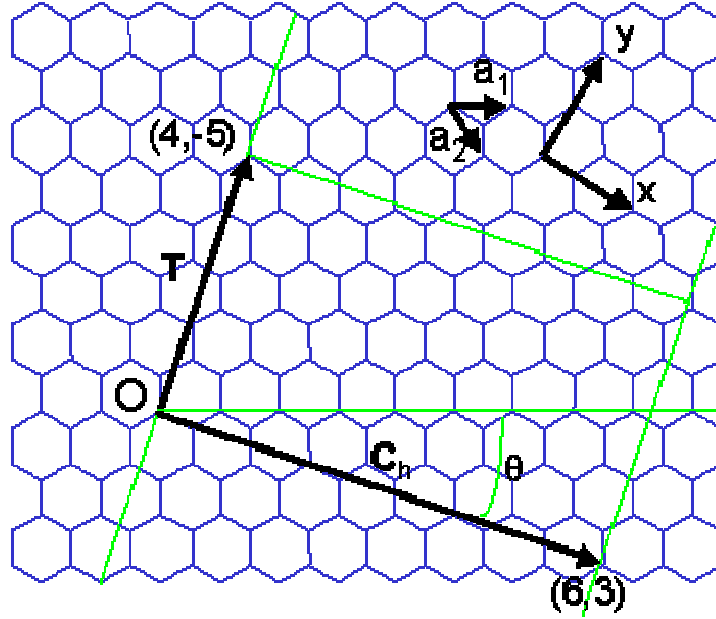


Figure 2-1: Hexagonal graphite lattice showing the unit vectors \mathbf{a}_1 and \mathbf{a}_2 . This image shows the chiral vector, \mathbf{C}_h , and translation vector \mathbf{T} for a (6,3) nanotube

As mentioned, the indices (n,m) determine a nanotubes electrical properties. The electronic structure of carbon nanotubes can be obtained by using the two-dimensional structure of graphite and applying period boundary conditions along the circumferential direction \mathbf{C}_h . The unit structure of graphite contains two inequivalent carbon sites within the hexagonal lattice called points A and B, Figure 2-2A. Real-space lattice vectors were previously defined in x,y coordinates. In reciprocal space, the lattice vectors are $\mathbf{b}_1 = (2\pi/3^{1/2}a, 2\pi/a)$ and $\mathbf{b}_2 = (2\pi/3^{1/2}a, -2\pi/a)$, Figure 2-4B.

When the first Brillouin zone is chosen as the shaded region in Figure 2-2B the highest symmetry is obtained for graphite. In 2-D graphite, the three σ bonds hybridize in an sp^2 configuration. The third $2p^z$ orbital forms covalent π bonds. Generally, only the π

bands are considered when deriving the band structure of graphite. Saito *et al.*¹⁸ used a tight binding model that only considers nearest neighbor interactions to A and B, to get the following dispersion relations for the π band of 2D graphite

$$E_{2Dgraph}(\mathbf{k}) = \varepsilon_{2p} \pm t \cdot \omega(\mathbf{k}) / (1 \pm s \cdot \omega(\mathbf{k})) \quad (2-9)$$

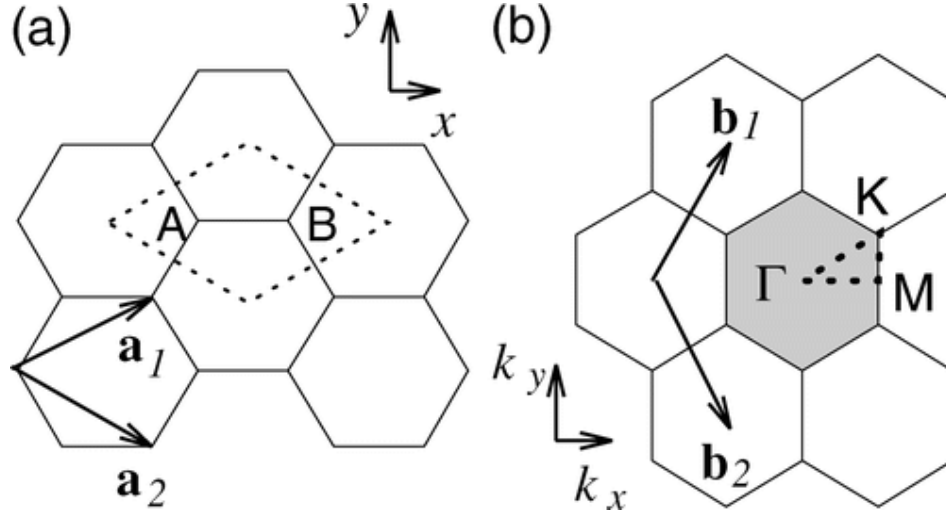


Figure 2-2: Unit cells of graphite. A) The real space unit cell of graphite is defined by the dotted line and contains points A and B. The unit vectors \mathbf{a}_1 and \mathbf{a}_2 are also shown. B) the Brillouin zone in k space for graphite and the reciprocal lattice vectors \mathbf{b}_1 and \mathbf{b}_2 .

The + signs in Equation (2-9) give the values for the bonding π band while, the – signs are for the antibonding π^* band. The parameter ε_{2p} is the orbital energy for the 2p level, s is the overlap integral between the nearest A and B atoms, and t is the transfer integral.

The function $\omega(\mathbf{k})$ has the form

$$\omega(\mathbf{k}) = \{1 + 4\cos(3^{1/2}k_x a/2) \cdot \cos(k_y a/2) + 4\cos^2(k_y a/2)\}^{1/2} \quad (2-10)$$

To get a simple approximation for the electronic structure of graphene the overlap integral s is usually taken to be zero with ε_{2p} also being set to zero. This yields the following expression for the energy dispersion relations.

$$E_{2Dgraph}(k_x, k_y) = \pm t \{1 + 4\cos(3^{1/2}k_x a/2) \cdot \cos(k_y a/2) + 4\cos^2(k_y a/2)\}^{1/2} \quad (2-11)$$

Plotting the energy dispersion relations for graphite reveal that the bonding and anti-bonding π bands meet at the K point; thus graphite is considered a zero-gap semiconductor (the density of states is zero at the Fermi level).

Previously the chiral vector \mathbf{C}_h and translation vector \mathbf{T} for a carbon nanotube were defined. The corresponding reciprocal lattice vectors \mathbf{K}_1 (in the circumferential direction) and \mathbf{K}_2 (along the direction of the nanotube axis) are calculated by the expression $\mathbf{R}_i \cdot \mathbf{K}_i = 2\pi\delta_{ij}$ (\mathbf{R}_i are the lattice vectors in real-space corresponding to \mathbf{C}_h and \mathbf{T}) giving

$$\begin{aligned} \mathbf{C}_h \cdot \mathbf{K}_1 &= 2\pi & \mathbf{T} \cdot \mathbf{K}_1 &= 0 \\ \mathbf{C}_h \cdot \mathbf{K}_2 &= 0 & \mathbf{T} \cdot \mathbf{K}_2 &= 2\pi \end{aligned} \quad (2-11)$$

This leads to

$$\mathbf{K}_1 = (-t_2\mathbf{b}_1 + t_1\mathbf{b}_2)/N \quad \text{and} \quad \mathbf{K}_2 = (m\mathbf{b}_1 - n\mathbf{b}_2)/N \quad (2-12)$$

Because of the translational symmetry of \mathbf{T} , wave vectors in the direction of \mathbf{K}_2 are continuous for an infinitely long nanotube. In the circumferential direction there are N wave vectors $\mu\mathbf{K}_1$ ($\mu = 0, 1, \dots, N-1$), which means N discrete k vectors. When the allowed k vectors in the circumferential direction include the K point (where the valence band and conduction band meet), the nanotube will be metallic. This occurs for the condition $(n-m)=3i$ (where i is an integer). Otherwise the nanotube will be semiconducting.

The armchair tubes (n,n) are all metals with a finite density of states at the Fermi level. Chiral tubes with $(n-m)=3i$ technically have a tiny gap that opens up at the Fermi level due to tube curvature effects. However this gap is so small that at room temperature these tubes can be considered metallic. The band gaps of semiconducting nanotubes are inversely proportional to the nanotube diameter. The size of the band gap depends on how close the allowed k values are to special K point. The larger the diameter of a nanotube the more k values there are. Thus the spacing between the k points decreases

and the values get closer to the K point resulting in a smaller band gap. The one-dimensional nature of the nanotubes leads to peaks in the density of states known as van Hove singularities. Semiconducting tubes that are slightly doped (as is often the case) can have their Fermi levels shifted into the first Van Hove singularity. Because of this these doped semiconducting nanotubes are often more conductive than the intrinsic metallic nanotubes at room temperature because of the large number of carriers.

CHAPTER 3

MOTIVATION AND THEORY FOR INDIVIDUAL CARBON NANOTUBE ACTUATION

3.1 Electromechanical Actuation

Electromechanical actuators convert electrical energy into mechanical work. The fine motor movement possible with these devices is used in various fields such as laser tuning, vibration cancellation, adaptive optics and micromanipulation. Piezoelectric actuators are the most commonly used devices of this type (one example is the scanner used in atomic force microscopes). Many actuators can only be operated in a limited temperature range or have other physical limitation (piezoelectric actuators must be operated below their Curie temperature and suffer from hysteresis). In 1999, Baughman *et al.*⁸ reported an experiment in which they attempted to use carbon nanotubes (in bulk form) as actuators. The chemical robustness and small dimensions of SWCNTs made them seem like a promising addition to the repertoire of actuator materials. The intriguing results of these macro-scale actuators led to our study aiming to observe actuation in individual SWCNTs..

3.2 Macro-Scale Carbon Nanotube Actuators

Baughman *et al.*⁸ used a macro-scale composite of SWCNTs know as “bucky paper” as a demonstration of their actuator. Bucky paper is formed by vacuum filtering a suspension of carbon nanotubes onto Teflon filter paper. This forms a sheet of tangled nanotubes, which can be peeled off the filter as a freestanding film. One version of the actuator was fashioned by applying equal sized strips of bucky paper to both sides of a

slightly larger piece of double-sided tape as shown in Figure 3-1. Electrodes were attached to both strips in order to inject charge and the bucky paper-tape composite was immersed in an electrolyte solution. The ions in the electrolyte served to screen the charges being injected onto the nanotubes by forming a double layer. Without it, Coulombic repulsion would prevent the injection of significant amounts of charge.

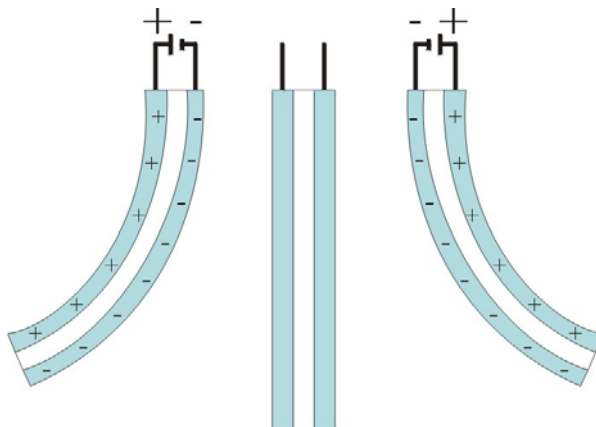


Figure 3-1: Macro-scale actuator.

Voltages of opposite polarity were applied to the two sheets and motion of the tri-layer structure was observed. It appeared that the strip on the negative terminal would elongate and conversely the strip on the positive terminal would contract causing an overall wagging motion as the polarity was flipped back and forth. To actually measure the stress and strain of the bucky paper another setup was employed. The bottom of a freestanding bucky paper was fixed to the bottom of the apparatus while the top was attached to a cantilever. Changes in the length of the nanotube film would deflect the cantilever and an optical sensor detected displacements of the cantilever.

The strain values calculated from the experimental data from this second experiment setup are shown in Figure 3-2. The behavior shown in Figure 3-2 was interpreted as arising from a change in the lattice constant of the nanotube atomic lattice

with charge injection into the nanotube pi-orbital system. This is an effect known to occur in chemically intercalated graphite (described in section 3.3), and Baughman *et al.*⁸ attributed their observations to it.

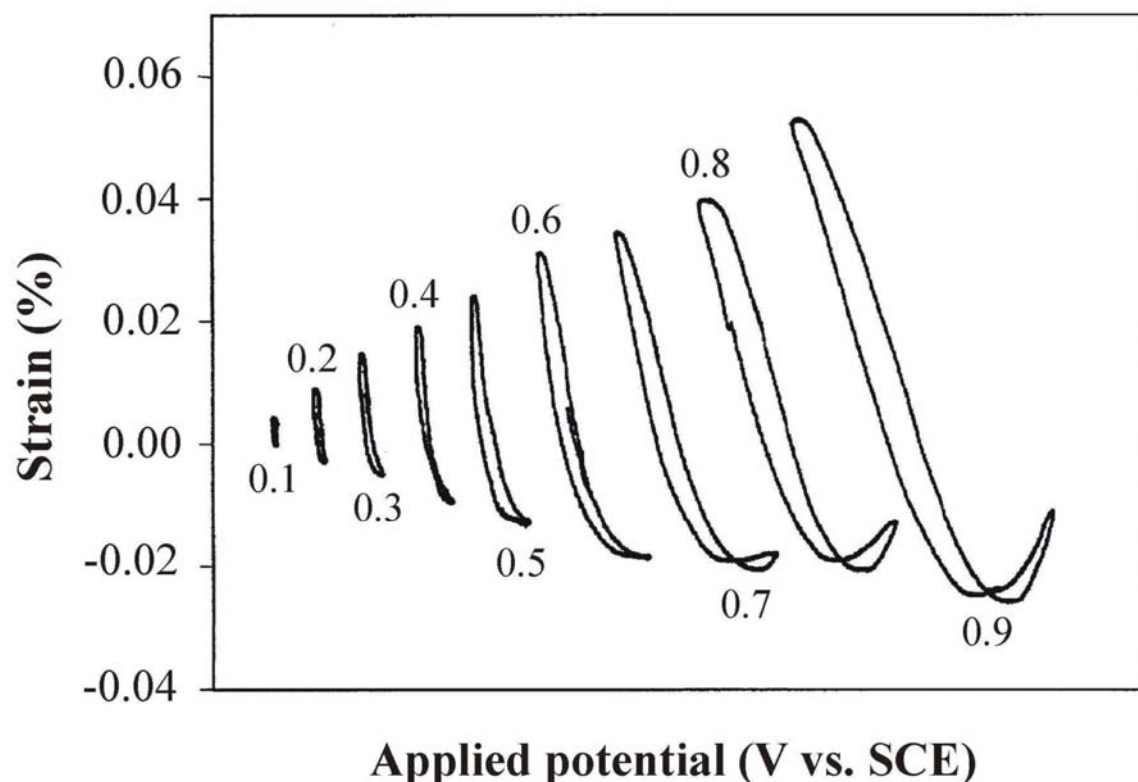


Figure 3-2: Strain values for bucky paper actuators films versus applied potential in 1M NaCl electrolyte solution. The applied potential was symmetric about $V=0$.

3.3 Bond Length Changes in Intercalated Graphite

Graphite intercalations compounds (GICs) are formed by the spontaneous charge-transfer driven insertion of a chemical species, called the intercalant, between layers of the graphite matrix. They are classified by a stage index, n , which represents the number of graphite layers in between intercalant layers. Thus a large stage number would denote a dilute GIC and a stage number of 1 would represent one layer of intercalant for each layer of graphite. The interclants are labeled as acceptor (donor) compounds if they take

(give) electrons from the graphite lattice and this process can vary the free carrier concentration greatly. This in turn can vary numerous electrical and physical properties of the host graphite.

Intercalation compounds undergo not only an expansion along the c-axis due to the additional volume of the intercalants but more interestingly (in the present context) they also show in plane dimensional changes. In 1969 Nixon and Parry¹⁹ showed, through x-ray diffraction, that the C-C bond length expanded due to the intercalation of graphite by the donor species potassium. Following that, measurements on other graphite intercalation compounds were performed using such dopants as Na, Li, Ba, MnCl_2 , and AsF_5 and a strain versus estimated charge transfer curve was generated, Figure 3-4).^{20,21,22,23,24} Doping by donor compounds, i.e. additional electrons in the carbon lattice, resulted in lengthening of the C-C bond, while doping by acceptor compounds resulted in bond shortening (although smaller in magnitude). That the bonds would shorten at all is counterintuitive. Simple Coulombic considerations from the additional charges imply an expansion regardless of the charge sign (since the Coulomb force is quadratic). Coulombic repulsion of the additional charges would try to expand the host in an effort to separate the charges. However, a quantum mechanical effect shifts the minimum graphite lattice constant from the point of zero charge transfer to the hole doped side. After the compilation of the charge transfer vs. strain curve some models were proposed to explain this behavior.^{25,26,27,28} It is these changes in the carbon-carbon bond length as a result of charge transfer that is the proposed mechanism for carbon nanotube actuation.

In 1981, Pietronero and Strässler first attempted to model the effect of additional charge in a single graphite layer using tight binding energy calculations.²⁵ They noted

that two effects would occur from this additional charge per carbon atom. First, this additional charge would cause a change in the occupancy of the π states and thus a modification of the bond order (in molecular orbital theory the bond order is defined as the number of bonding electrons less the number of anti-bonding electrons all divided by 2). Second, since the atomic potential has changed, a modification of all the tight binding matrix elements will arise. Additional electrons in the anti-bonding π orbitals weaken the C-C bond and causing bond lengthening. Also included in their work is the change in total energy due to Coulomb repulsion of the charged atoms (the dominating effect).

Graphite C-C Bond Length Vs. Charge Transfer

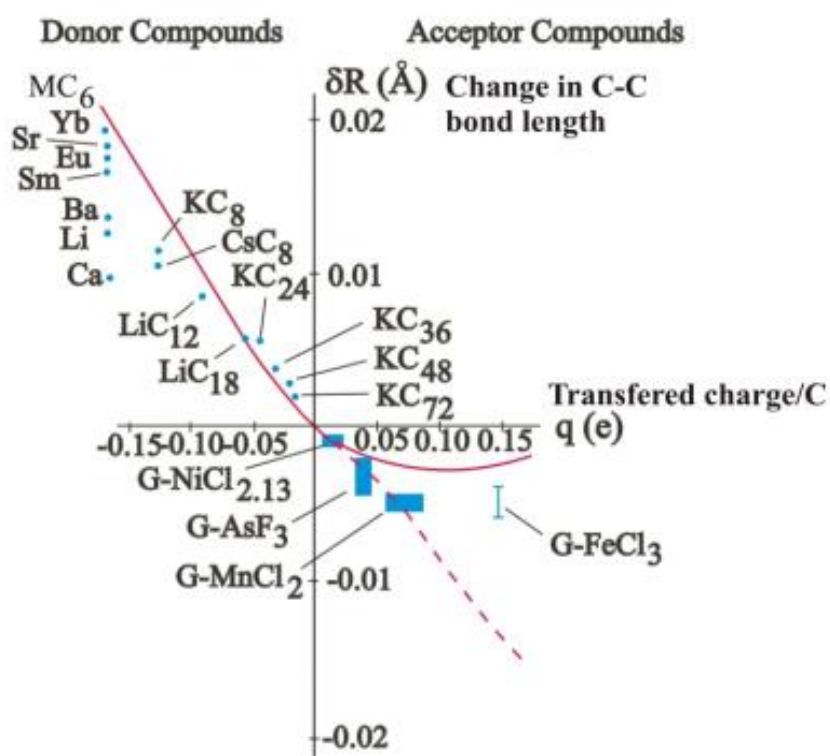


Figure 3-3: Strain versus charge transfer curve for graphite

This work was soon followed by Kertesz²⁶ and Kertesz *et al*²⁷, who also used tight binding theory to ascribe the bipolar nature of the strain of graphite intercalations

compounds to second neighbor anti-bonding interactions. The inclusion of only nearest neighbor contributions would result in expansion for both electron and hole injection so this interaction was needed to explain the observed results.

The next significant work was done by Chan *et al.*²⁸ who used density functional theory to focus on the changes induced in graphite solely as a result of the charge exchange with the intercalants. For the higher stage GIC's they assumed that the bounding layers had the same in plane lattice parameter as those next to the intercalants. In other words, the strain is shared uniformly among all the graphite layers. This was noted in experiment¹⁹ and supported by energy considerations. It would take far greater energy to assume different lattice parameters for the bounding and interior layers than would be required to make all the layers assume the same parameter. Using this approach, Chan *et al.* also noticed a previously unrecognized mechanism that could not be obtained from rigid-band models. Not only does the donated charge reside in the π orbitals but their theory also suggests a depletion of charge from the σ bonds. The external potentials from donor species appear to cause electron transfer from the σ to π bonds further weakening the C-C bond and increasing the bond length.

All previous experimental work estimated the amount of charge transfer from the intercalants to the graphite and the theoretical calculations were based upon this estimate. In most instances, it was assumed that the charge transfer would be nearly complete. This work performed an experiment in which the intercalation compounds were placed on a charge transfer scale and thus the actual charge transfer could be measured and correlated with the associated bond length changes. Although their experimental setup dictated that they use neutron diffraction, which is lower in resolution than x-ray

diffraction, the experiment showed that the previous assumptions about the amount of charge transfer were within reason.

3.4 Theoretical Work for Bond Length Changes in Carbon Nanotubes

Since carbon nanotubes have the structure of a graphene sheet rolled up into a tube it was only a matter of time before theoretical calculations were performed to predict the strain from charge transfer to nanotubes. Just as a SWCNT's electrical properties differ from that of graphite as a function of chirality, the predicted dimensional changes are predicted to differ from graphite as a function of chirality. In general, it appears that the exception is the armchair nanotubes (n,n). For this flavor of nanotube one of the allowed k values always passes through the K point where the occupied π and unoccupied π^* bands meet, just like in graphite. Since the electronic properties are similar to graphite so should be the dimensional changes due to transferred charge. Several groups differed on the predicted behaviors. The following paragraphs summarize these predictions and highlight some of the salient differences in the predicted response of SWCNTs compared to graphite.

Gartstein *et al.*²⁹ studied bond length changes in nanotubes from the modulation of electron hopping integrals. As tight binding models from graphite and carbon nanotubes are charge conjugated symmetric in the nearest neighbor hopping approximation they included second order hopping to account for the asymmetric actuation response going from positive to negative charge injection. They predicted oscillating dimensional changes as a function of chirality, with most nanotubes showing typical bond length expansion upon electron injection but some small diameter SWCNTs showing contraction for electron injection. The magnitude of the dimensional change (for the

same amount of charge transfer) also varies with the chirality. Their results predict some semiconducting nanotubes will show strains 3-4 times larger than those in graphite and other tubes will show substantially decreased responses.

A subsequent paper by Gartstein *et al.*³⁰ extended their previous work on the effect of charge injection on the geometries of nanotubes. Those results are surprising since they are markedly different than the response in graphite. They predict that a (10,0) and a (16,0) will show contraction upon both hole and electron injection and conversely, that a (11,0) and a (17,0) tube will expand for both signs of doping. Also at a certain charge injection level the response appears to reverse for the (16,0) and (17,0) nanotubes. It should be noted that Coulombic effects, which are quadratic in their effect and certainly play the dominant role at large values of charge transfer, were not taken into consideration in these calculations.

Verissimo-Alves *et al.*³¹ also examined charge transfer induced dimensional changes for a limited number of nanotubes. They carried out *ab initio* calculations with the density functional theory and pseudopotential frameworks using a numerical-atomic-orbitals basis set. They used those calculations to generate strain versus charge transfer curves for graphite, metallic (5,5) and (12,0) nanotubes, and a semiconducting (11,0) nanotube. The predictions for the (12,0) tube and graphite appear very similar but the (5,5) nanotube differs in that it appears to show a significantly increased elongation for negative charge injection but diminished contraction for electron withdrawal. The results for the (11,0) nanotube predict expansion for both signs of charge injection. Strain calculations (at charge transfer of 0.01 electrons/C atom) for several zigzag semiconducting nanotubes with $n=3i-1$ (i is an integer) predict that SWCNT's with a

diameter smaller than that of the (23,0) tube (diameter = 1.8 nm) will expand for both positive and negative charge injection. Larger diameters switch back to the behavior seen in graphite (contraction for hole injection). Their analysis is that this behavior can be explained by the position of the atomic level of the π orbital state of carbon, ϵ_{2p} , with respect to the Fermi level. According to tight binding calculations, inclusion of next nearest neighbor effects raises the energy eigenvalues at the K points above the ϵ_{2p} level. Anything above ϵ_{2p} is anti-bonding and anything below is bonding. Thus, (if the Fermi level is above ϵ_{2p}) adding electrons causes expansion and withdrawing them causes contraction. If enough electrons are withdrawn the Fermi level will fall below ϵ_{2p} and into the bonding regime. At this point if further electrons are withdrawn the bond length will expand. For large band gaps, the Fermi level is below ϵ_{2p} . So for small diameter (large band gap) nanotubes, they predict the Fermi level will lay below ϵ_{2p} and demonstrate only expansion from charge injection. As the diameter increases, and the band gap decreases, and the semiconducting tubes should revert back to graphene-like behavior.

In 2002, a work by Sun *et al.*³² calculated strain versus charge curves for different varieties of achiral nanotubes (armchair (n,n) and zigzag (n,0)) using a uniform background charge to represent counterions in order to more closely reflect the conditions in the actuation experiments. They used density functional theory and the generalized gradient approximation. Nanotubes were grouped into four categories: (n,n), (n=3i,0), (n=3i + 1,0) and (n=3i + 2,0). These results predicted ambipolar behavior for all SWCNTs with the exception of the extremely small diameter (5,0) nanotube. In that case the response was expansion for both positive and negative charge injection.

The following year (2003) these authors used density functional theory to calculate the effect of charge injection on the geometries of achiral tubes as a function of diameter.³³ Their approach in this case differentiated between two different types of bonds, b_1 , which are those orientated mainly around the diameter and b_2 , which are those orientated mainly along the nanotube axis.

In armchair nanotubes b_1 is orthogonal to the tube axis (parallel to the diameter) and b_2 has components both parallel and orthogonal to the axis. Conversely, for the zigzag nanotubes b_2 is parallel to the nanotube axis while b_1 has the mixed components. Unlike graphene, their calculations predicted that the bond length's b_1 and b_2 would be different from each other with $b_1 > b_2$ in almost all cases. The larger value of b_1 is a result of the curvature and the differences in lengths between the two bonds decreases with increasing diameter. The differences between b_1 and b_2 are smaller for the armchair tubes than the zigzag tubes of the same diameter and decrease with increasing nanotube diameter. They calculated how these differing bonds would change with the addition of charges and then computed the overall strain for several charged nanotubes at charge injection levels of $q = \pm 0.01 e/\text{carbon}$

These results show some contradictions to their previous work. One example is that the small diameter $(3i + 2, 0)$ nanotubes will show expansion for both signs of charge injection, something not shown in their earlier publication but similar to the predictions of Verissimo-Alves *et al.*³¹ However, these results indicate the $(3i + 2, 0)$ family will revert to bipolar behavior starting with diameters greater than or equal to that of the $(14, 0)$ nanotube while Verissimo-Alves *et al.* predict this behavior won't resume until the nanotube diameter is at least as large as the that of the $(23, 0)$ SWCNT. Another interesting

result of this work is that the predictions for the $(3i + 1, 0)$ series of nanotubes show a larger magnitude of contraction for electron withdrawal compared to expansion for electron donation. This asymmetry goes the opposite way in graphite.

There are quite a few discrepancies between the different theoretical calculations published in the literature. As another example, the results for the (10,0) tube with $q = \pm 0.1$ e/carbon in the work Garstein *et al.*³⁰ predict contraction for both signs of charge injection (something not seen in any other theoretical work) while the calculations of Sun *et al.*^{32,33} predict a response for the (10,0) tube more similar to graphite with contraction for positive charge injection and expansion for electron injection, also for $q = 0.01$ e/carbon. These papers show that there is much interest in nanotube dimensional changes caused by charge injection. Our work was started prior to the publication of these theoretical works and was motivated by the bucky paper actuator experiment. The goal was to observe charge induced actuation in individual nanotubes to determine if that was the mechanism responsible for the effect witnessed by Baughman *et al.*⁸

CHAPTER 4

PREPARATION OF AND EXPERIMENTAL MEASUREMENTS ON SUSPENDED CARBON NANOTUBE SAMPLES

To measure dimensional changes in a SWCNT we devised an experiment that would allow injection of charge onto an individual nanotube while measuring the resulting small changes in its length. The experimental arrangement devised to do this is illustrated in Fig. 4-1. Shown there is a nanotube suspended over a micro-machined trench in a silicon substrate where the nanotube is pinned at its ends by metal electrodes.⁷ Like the bucky paper actuator setup, this experiment was also performed in an electrolyte solution. Charge injection onto the nanotube occurred via a potential applied to the pinning electrodes versus a counter electrode in the electrolyte solution. To measure length changes, the suspended nanotube was pre-tensioned by a modest force applied at its center with the tip of an AFM cantilever. This deflected the center of the nanotube from the top of the trench while simultaneously deflecting the AFM cantilever from its set point equilibrium position. If the nanotube lengthened, its center would deflect further into the trench to be detected by the corresponding relaxation of the AFM cantilever. If the nanotube shortened, the tip would in contrast be forced upwards increasing the deflection of the cantilever from its set point position.

4.1 Fabrication of Suspended Carbon Nanotube Structures

Fabrication of samples consisted of depositing nanotubes (either out of solution or growing by CVD) onto silicon and lithographically patterning electrodes on top of the SWCNTs. The nanotubes were suspended by a wet chemical etch of the underlying silicon. Details are described in the following sections.

4.1.1 Substrate Preparation

Commercially available p-type <100> silicon wafers with a thermal oxide layer were used as the substrates. Wafers were coated with Shipley S1813 photoresist to avoid silicon dust contamination prior to dicing into 1 cm^2 pieces used for suspended nanotube sample fabrication. To strip photoresist from the 1 cm^2 pieces the chips were rinsed with acetone, bathed in acetone for 10 minutes, rinsed with acetone again, rinsed with methanol, rinsed with 18 MOhm deionized water (DI) and finally blown dry with N_2 gas.

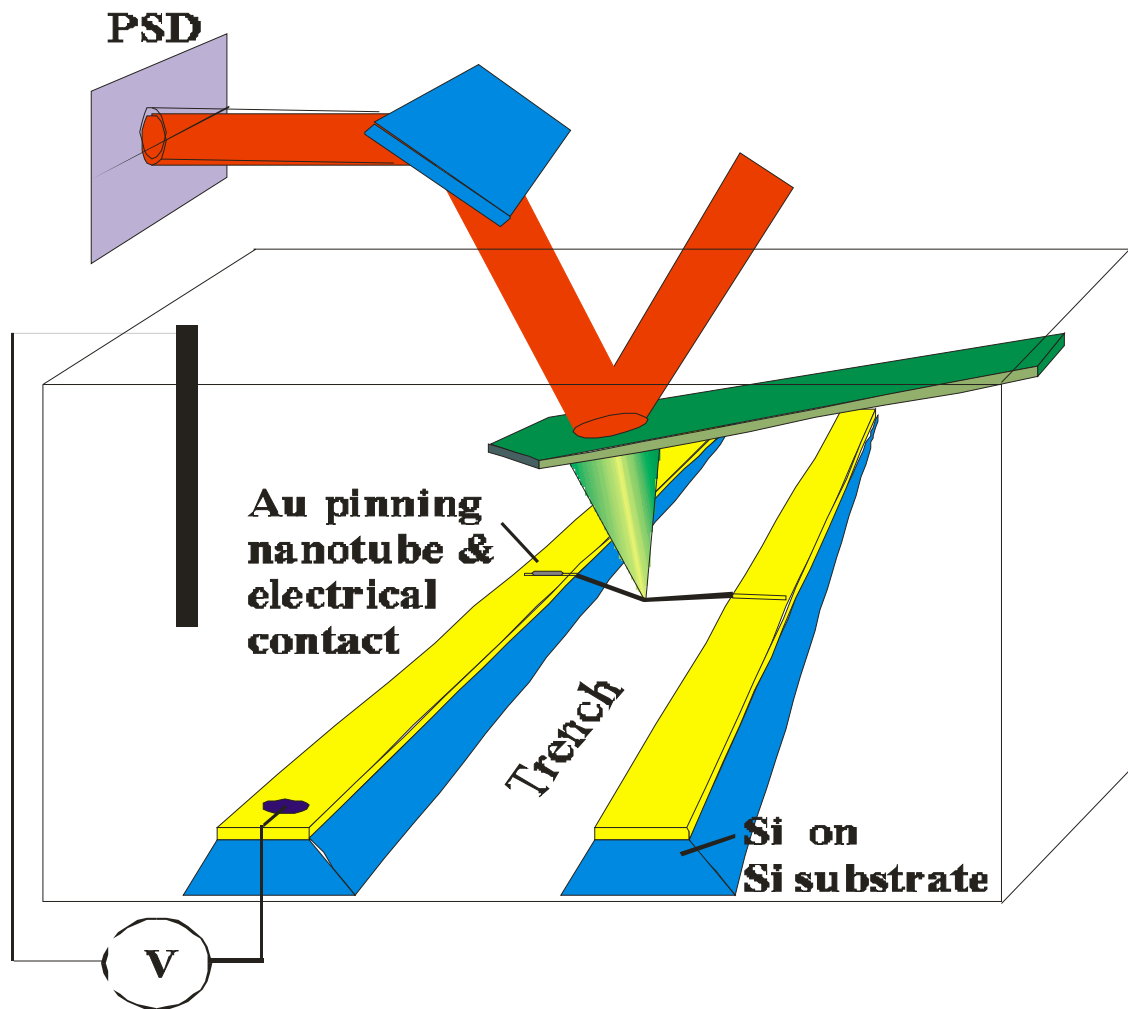


Figure 4-1: Actuation experimental setup.

4.1.2 Carbon Nanotube Deposition and Growth

Early samples in this work were fabricated by depositing purified laser ablation grown SWCNT's out of solution onto a silicon substrate. However, longer nanotubes were required and later samples used SWCNT's grown by CVD. Both methods are described here.

4.1.2.1 Deposition of Laser Ablation Grown Nanotubes from Solution

The first step in this approach is to get the nanotubes on the silicon surface. Walters *et al.*⁷, who had also fabricated suspended nanotube structures, used purified³⁴ pulsed laser vaporization grown nanotubes that were suspended in N,N-dimethylformamide and deposited this onto silicon chips that had a 100nm thermal oxide layer. To date, there are no known solvents for SWCNTs. Some solvents, such as N,N-dimethylformamide or 1,2 –dichlorobenzene, can form quasi stable solutions which will suspend the nanotubes for short periods of time³⁵ but the density of the nanotubes is very limited. The nanotubes tend to form bundles with each other while in solution. As Brownian motion causes individual nanotubes to encounter each other in liquid, the strong van der Waals interactions between the sidewalls causes the nanotubes to aggregate into bundles. Thus, deposition from these metastable suspensions rarely results in individual nanotubes. Additionally, if the tubes are deposited in a manner that allows the solvent they are suspended in to evaporate, any impurities within the solvent will be left on the sample.

Nanotubes can be suspended in aqueous solution with the aid of surfactants. Sodium dodecyl sulfate, Triton X-100 and most recently sodium dodecylbenzene sulfonate have been used for this purpose.^{36,37} Originally I used purified³⁴ Tubes@Rice material that was suspended in a 1% Triton X-100 solution and deposited on bare silicon

surfaces from solution. Following purification, the nanotubes are kept in a slightly basic solution of Triton-X in deionized water. This solution was vacuum filtered onto a Teflon membrane, forming a film of nanotubes on the membrane. This film was washed with 1% Triton X-100 in DI water and allowed to dry. A small amount of this film was torn off and immersed in an aqueous 0.5% Triton X-100 mixture. The solution was placed in an ultra-sonicator bath for typically 10 minutes. This action broke up the strip of bucky paper into individual and small bundles of nanotubes.

The 1 cm² silicon chips were subjected to a buffered oxide etch (BOE) diluted 1:1 with deionized water to remove the thermal oxide layer. This left the samples with a hydrophobic H-terminated silicon surface. These chips were subsequently placed in a small vial and covered with a few milliliters of the nanotube/Triton-X solution. The addition of a drop of concentrated acid (usually nitric acid) interfered with the surfactant's ability to suspend the nanotubes such that after a few minutes the initially homogeneous, particle free solution contained flocculated nanotubes. The nanotubes (which are themselves hydrophobic) that lay close to the silicon surface adhered to the hydrophobic silicon as they exited the suspension.

Various techniques in which acid was used to remove the nanotubes from the Triton-X suspension were explored. One method involved placing a silicon chip face down onto several drops of nanotube/Triton-X solution and sliding the chip across a nearby drop of acid. This technique produced depositions in which the nanotubes were aligned in the same direction, as example of which is shown in Figure 4-2. A comparison of the alignment direction and the direction of the acid front as it propagated through the nanotube/Triton-X solution showed the two to be the same. Once the acid removed the Triton-X micelle from the nanotube, the hydrophobic SWCNTs aligned along the acid

front so that as much surface area as possible of the tubes would be out of the water solution.

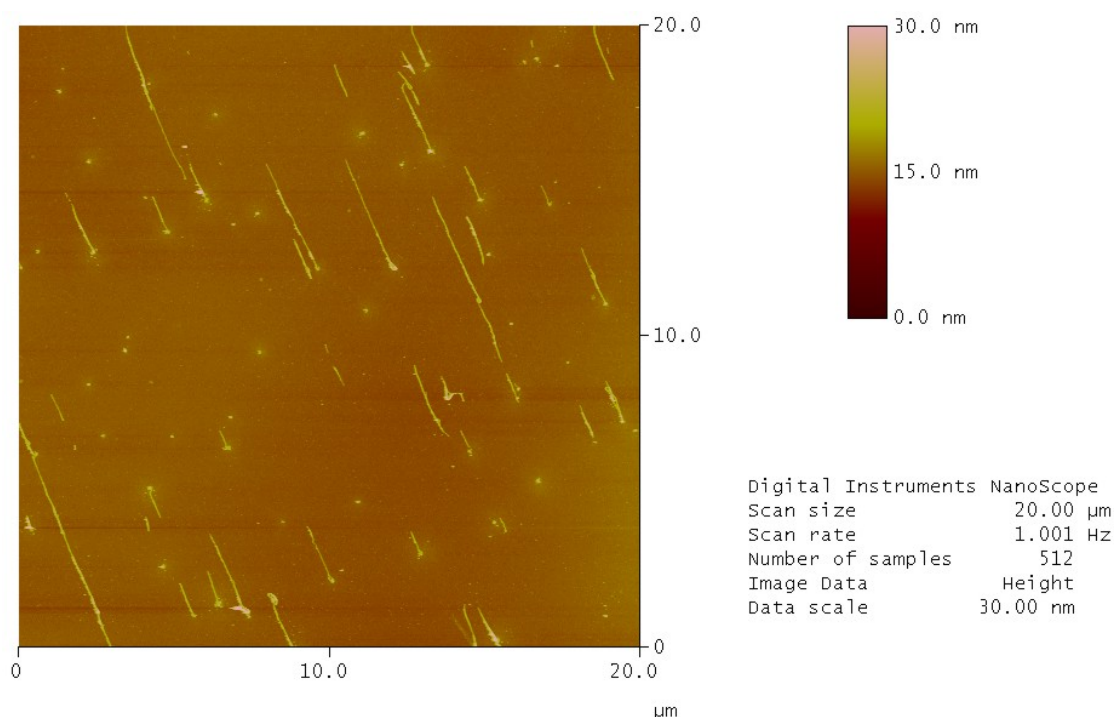


Figure 4-2: AFM image of aligned carbon nanotubes from Triton-X solution

Even though these samples would show high concentrations of nanotubes on the silicon surface, the density of suspended nanotubes after etching was low. As mentioned, nanotubes in solution tend to form bundles. This was certainly the case when the acid was added to the surfactant solution. After being deposited on the surface the laser grown nanotubes were grouped in bundles with very few (if any) individual nanotubes. Moreover, the purification these nanotubes were subjected to can shorten the SWCNTs. During the experiment, samples with nanotubes deposited by this method would often pull apart once tensioned by the AFM probe. This evidence, along with the low density of surviving suspended nanotubes, indicated that even though the ropes of bundled nanotubes would span the width of the trenches, oftentimes the individual nanotubes

comprising that bundle would not. This problem led to a switch to CVD grown nanotubes.

4.1.2.2 Chemical Vapor Deposition Grown Nanotubes

Substrates for CVD growth were diced and cleaned by the same method mentioned above but the buffered oxide etch was omitted so that the samples retained their thermal oxide layer. Additionally the chips were calcined at 1000° C in air for 7 minutes. Iron nitrate nonahydrate (Fisher Scientific, certified A.C.S.) was used as the catalyst.³⁸ and dissolved in 2-propanol (Fisher Scientific, Optima) in concentrations of about 10 µg/ml. Several drops, enough to flood the surface, were dropped onto the chip and the solution was spun dried at 3000 rpm. Growth took place in a 1” diameter tube furnace (Thermolyne F79300, 12” heating zone) using conditions reported by Li *et al.*³⁹ Hydrogen (200 sccm) and argon (300 sccm) were flowed across the chips placed approximately 2 cm downstream of the furnace center while the furnace heated to 900° C. Once at temperature, the argon flow was turned off and methane (200 sccm) and hydrogen (200 sccm) were introduced for 10 minutes. Following growth, the methane and hydrogen flow were stopped, the furnace heat switched off, and the samples were allowed to cooled under flowing argon (300 sccm). The density of the nanotubes grown on the samples was characterized by atomic force microscopy imaging. The CVD grown nanotube samples were superior to those made with deposited laser ablation grown tubes. The CVD grown nanotubes were much longer, sometimes with lengths over 10 microns, and were often individual nanotubes instead of bundles. Since all of the SWCNT’s grown by CVD were likely to survive the processing steps a CVD grown sample with a lower beginning density, like that in Figure 4-3A, would result in higher density of

suspended nanotubes than a sample with a high starting density of nanotubes deposited out of Triton-X suspension, like that in Figure 4-3B.

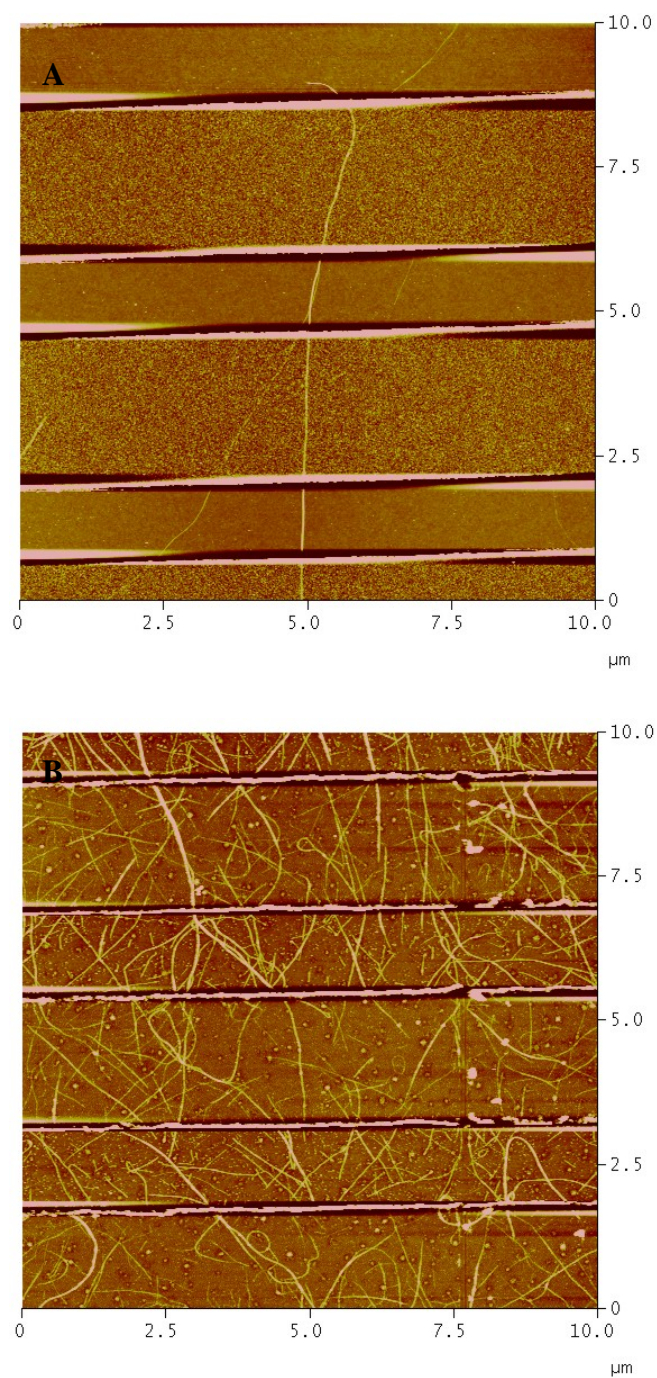


Figure 4-3: AFM images of nanotubes on silicon. A) Nanotubes grown by CVD. B) Nanotubes deposited out of solution.

4.1.3 Electrode Patterning

To make electrical contact to the nanotubes and also pin them in place (so that they could be suspended) metal electrodes were deposited on top of the nanotubes. Patterning was done by photolithography. A recent development in the field has been the formulation of lift off resists (LORs). These resists are not photosensitive but dissolve in the same developer used for the primary resist. The LOR is applied in a thin layer to the substrate to underlie the subsequently spun on photosensitive resist. During the photoresist development step, the exposed edge of the LOR underlying the unexposed (not removed) photoresist is dissolved back resulting in an effective undercut to the photoresist layer. This undercut means that when metal is deposited it is done so discontinuously as illustrated in Figure 4-4.

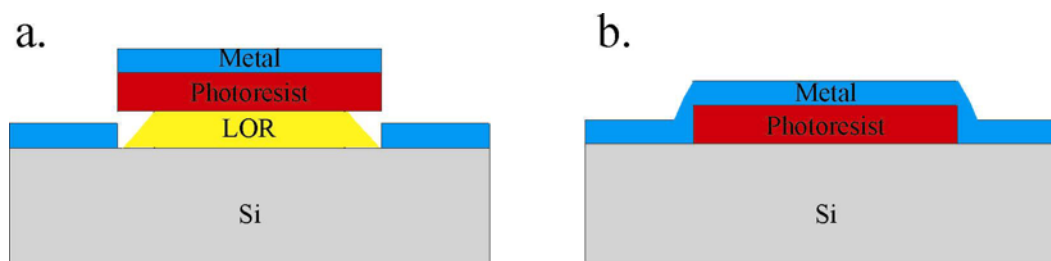


Figure 4-4: Metal deposition on resists. A) Discontinuous metal deposition as a result of using a lift off resist. B) Continuous metal layer using only a standard photoresist.

When using only conventional photoresist, the metal tears at the points where the resist is lifted away causing rough edges on the pattern. The use of LOR permits smooth electrode edges and easier lift off procedure requiring minimal ultrasonication for the lift-off. AFM line scans (essentially cross-sections) of electrodes fabricated both with and without an LOR layer are shown in Figure 4-5.

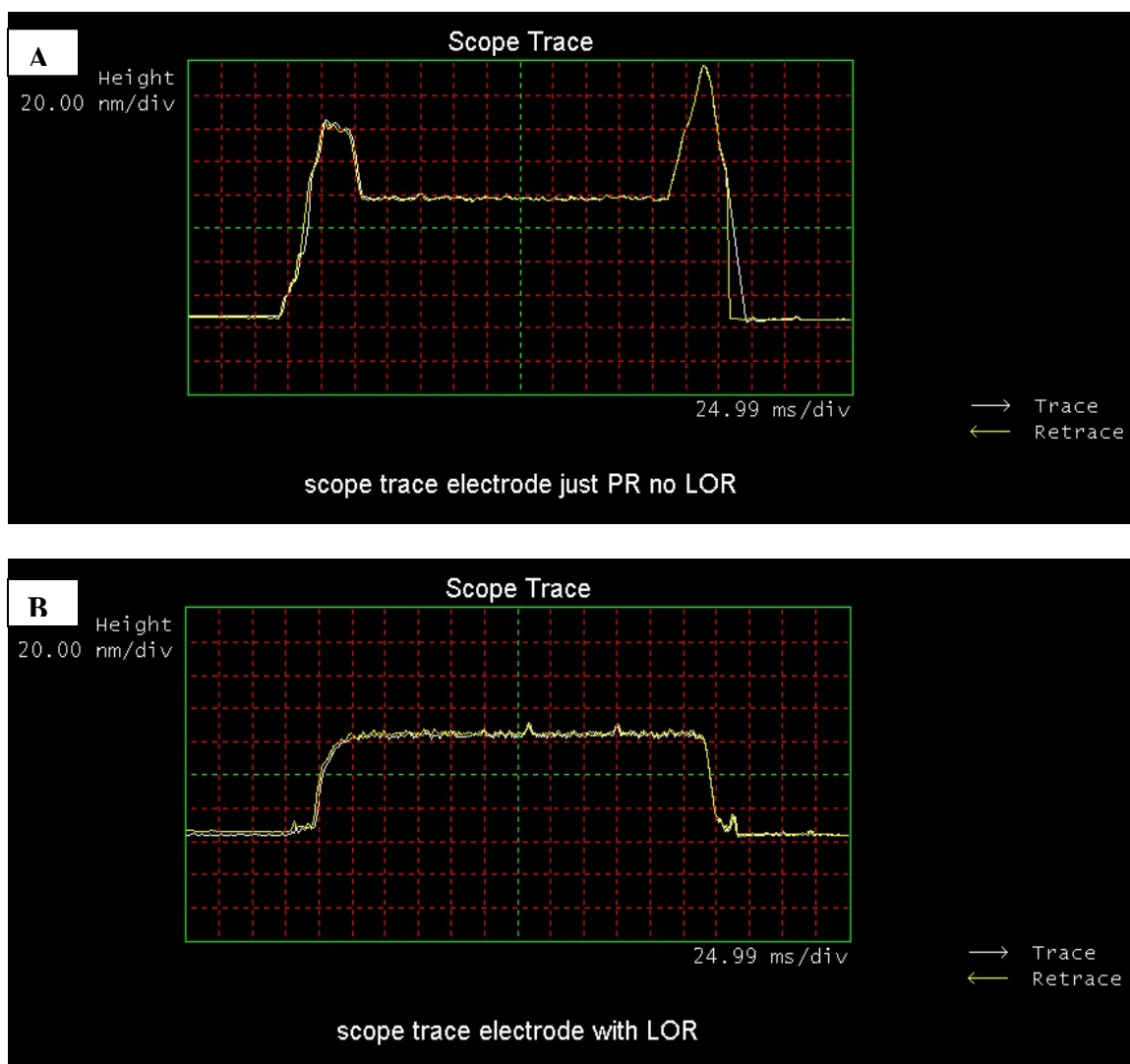


Figure 4-5: AFM scope trace of electrodes. A) No LOR, the flaps of metal at the edges are clearly visible. B) With LOR

During the course of this work, a particular benefit of using LOR with regard to using carbon nanotubes in lithography applications was found. After all the lithography steps, concluding with lift off, the samples were AFM imaged to inspect the surface quality, nanotube density, and metal height. Samples that used an LOR layer contacting the nanotubes had much cleaner carbon nanotubes than samples that only used the Shipley S1813 contacting the nanotubes. It seems that the organic materials in the photoresist have a particular affinity for the nanotubes. Although the surface of the

underlying silicon was very clean the SWNTs appeared to have globs of material stuck to them. Despite submersion in various solvents (photoresist remover, acetone, methanol, etc.), sometimes with sonication and at elevated temperatures, the globules remained attached to the nanotubes. Subjecting the nanotubes to an extended ozone cleaning step (~15 minutes) did help remove much of the material but there is the possibility this could be harmful to the nanotubes and even that did not remove all of the extraneous material.

The components in the LOR do not seem to have the same affinity towards the nanotubes and leave an uncontaminated surface without the need for additional cleaning. So there are two benefits to using LOR during electrode fabrication. The electrodes have smooth edges and standard photolithography can be performed on SWCNTs without being hampered by additional contaminants. Figure 4-6A shows the image of a nanotube on which Shipley S1813 photoresist was used without the LOR layer protecting the nanotubes. The contaminants are clearly visible on the surface of the nanotube. For comparison, Figure 4-6B shows two intersecting nanotubes on a sample where LOR and the same Shipley S1813 photoresist were used. The latter sample is obviously much cleaner.

To prepare the silicon chips with nanotubes on the surface for lithography, the samples were heated in a 110° C oven for 30 minutes to drive off any surface water. Microchem LOR 3B was diluted 1:1 with type G thinner and spun onto the silicon surface at 5000 rpm for 30 seconds. The LOR layer was baked at 170° C for 45 minutes. Shipley S1813 was used as the photoresist and was mixed 3:1 with Shipley Type P thinner. It was spun on at 5000 rpm for 30 seconds which yielded a layer of photoresist ~800nm thick. The photoresist-coated samples were then soft baked at 90° C for 30 minutes. UV exposure was performed with a Karl Suss MA6 mask aligner with a 365nm

UV light source (11 seconds exposure time, 7.4 mW/cm² intensity). Following exposure, the samples were developed in Shipley MF-319 developer (22 seconds), rinsed in deionized water and blown dry with a stream of clean nitrogen gas.

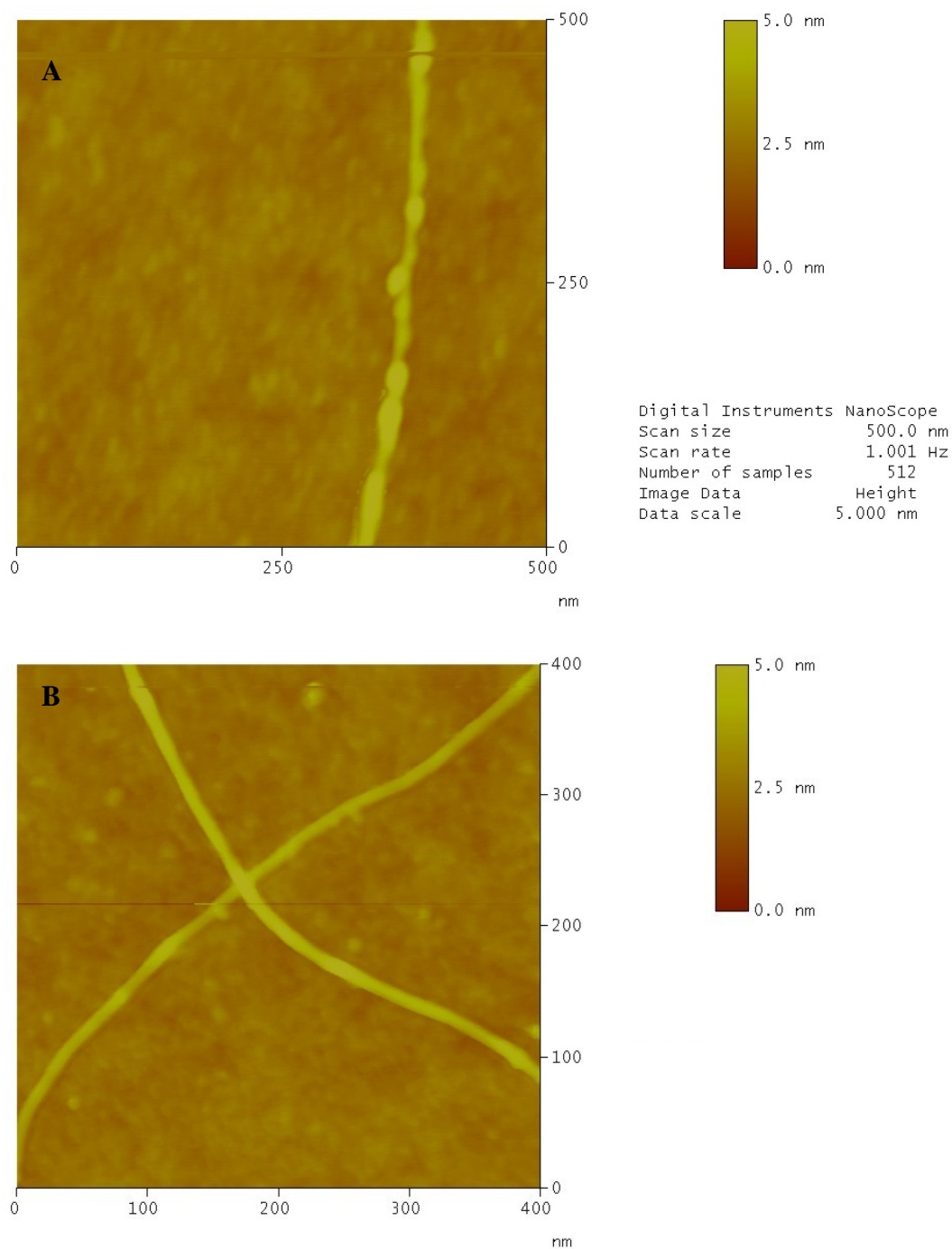


Figure 4-6: AFM images of nanotubes after lithography. A) Nanotube coated with photoresist. B) Nanotubes coated with a layer of LOR under the photoresist

Prior to metallization the samples were subjected to a UV ozone cleaning step for 1 minute. This treatment helped remove any residual organic contamination left on the nanotubes and ensures good adhesion of the metal to the nanotubes. Since the metal acted as the etch mask for the later SiO_2/Si etch, without this treatment, those etchants would chew through the residual photoresist layer, getting under the metal electrodes, to attack the underlying silicon. The next step in sample preparation was metallization. Chrome/Gold and Chrome/Platinum-Iridium were both used as the pinning electrode metals. The chrome/gold layers were grown by thermal evaporation while chrome/platinum-iridium samples were grown by RF magnetron sputtering.

After metallization, a lift off step to remove the rest of the photoresist and unwanted metal was employed. Lift off occurred in Microchem Nanoremove PG. The samples were immersed in the Nanoremove and placed in a 60°C bath for 30 minutes. During the last 10 minutes of that the samples underwent low power ultra sonication to aid the lift off process. High powered or prolonged sonication was found to remove the nanotubes from the surface. AFM images of samples subjected to more powerful sonication show many nanotubes lying under the surface of the electrodes but no nanotubes in the space between. Following the first heated bath, the samples were immersed in fresh nanoremove solution and placed in a 60°C bath for an additional 30 minutes. After lift off, the samples were rinsed in 2-propanol and blown dry with clean nitrogen gas.

5.1.4 Etching

To suspend the nanotubes the underlying silicon was etched away. Samples with an oxide layer were first etched in a 1:1 buffered oxide: deionized water solution. The next step for these samples, and the first step for samples whose oxide layer had previously

been removed, was an anisotropic wet silicon etch. The etchant solution was an aqueous 30% (by weight) potassium hydroxide solution. The KOH solution was mixed 4 parts to 1 with 2-propanol and heated to 60° C. Samples were etched for 90 seconds, which gave a trench depth of around 600 nm. To quench the etching, the samples were moved from the KOH bath to a 60° C deionized water bath and then to a room temperature deionized water bath but were kept submerged during each transfer. A schematic of all processing steps described so far is illustrated in Figure 4-7.

5.1.5 Release Procedure

Location of the nanotubes for the experiment first required imaging the samples in a scanning electron microscope to find the nanotubes. This required that the samples be dry. If the nanotubes samples were removed directly from water to air, the surface tension of the water would pull down the suspended tubes to the bottom of the trenches. Originally we tried the method used by Walters *et al.*⁷. This technique involves slowly exchanging the liquid for successively lower surface tension solvents while keeping the sample immersed the entire time. After etching the water was slowly exchanged for acetone, which was in turn slowly replaced with tetramethylsilane (TMS). TMS has a low surface tension of 10.2 mN/m, or roughly 1/7 the value of water. Once the TMS exchange was complete the samples were removed from the liquid and the TMS was allowed to evaporate. Unfortunately, TMS is difficult to purify and the impurities in the solvent were left on the nanotubes.

To avoid this contamination we developed an alternative approach in which the samples were “freeze dried”. After etching a chip was transferred to a small copper boat filled with water just sufficient to cover the sample. The water was then flash frozen by

placing the boat directly into liquid nitrogen. These frozen samples were then placed in a freeze drier (home built) where the ice was slowly sublimed away

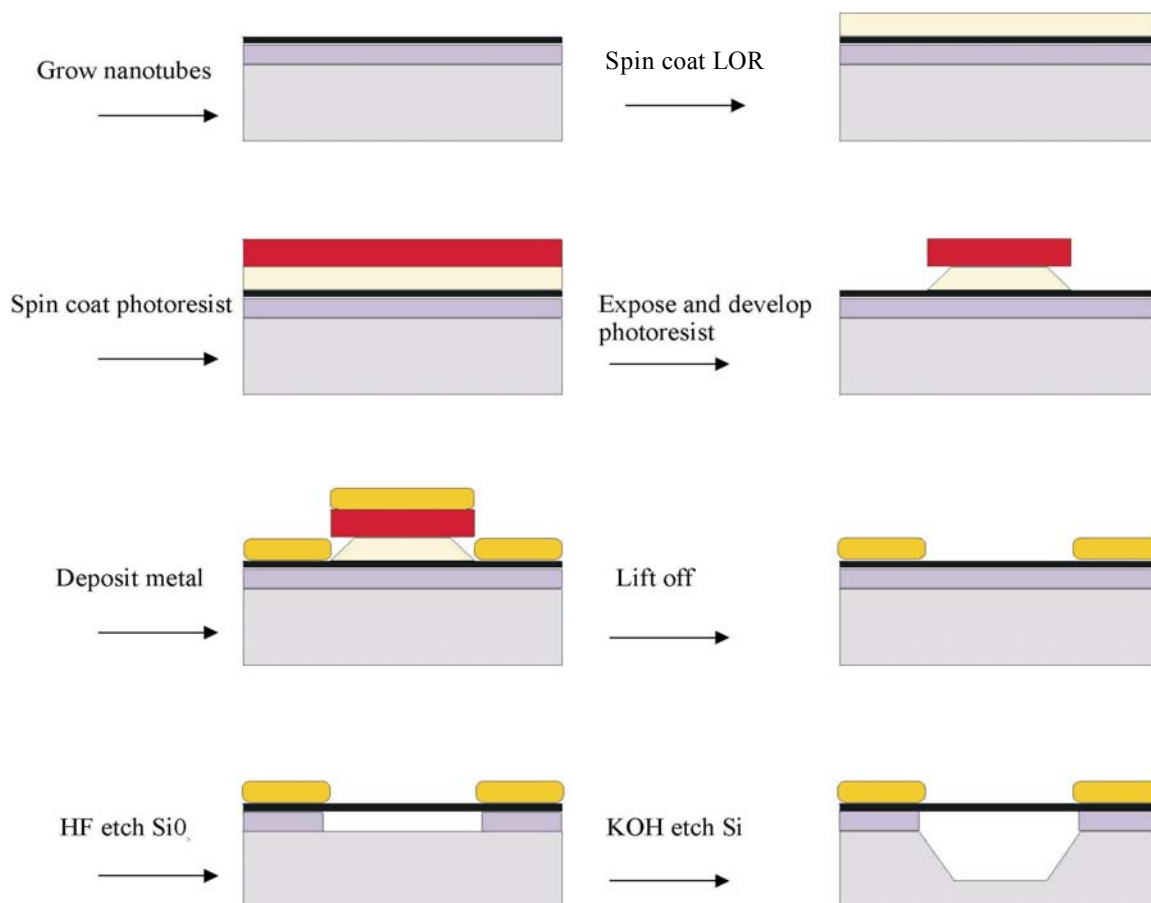


Figure 4-7: Illustration of processing steps for suspended carbon nanotube samples.

A method to determine if these processing steps had an effect on the samples was to measure the resistance between adjacent electrodes (across the nanotubes) before and after the etching steps. For the actual samples numerous nanotubes did not survive the processing, ending up at the bottom of the trench. Since the doped silicon then provided a current path between the adjacent electrodes via these downed tubes these samples could not be used for such measurements. Instead nanotubes were grown by CVD on silicon

with a 600nm oxide layer and a 14 electrode interdigitated pattern (made of thermally evaporated Cr/Pd) deposited on top of the nanotubes. The spacing between electrodes was the same as the pattern used for the actuation measurement samples (~ 1 micron). These test chips went through identical processing steps (HF etch, KOH etch, and TMS release or freeze drying). Since the oxide was much thicker on these samples the HF step did not etch through the oxide layer. The resistance was checked before and after the processing steps for samples that went through the liquid release procedure and freeze dry procedure, Table 4-1. The resistances of the samples did increase but that is likely due to fewer numbers of tubes surviving to connect across electrodes at this stage.

Table 4-1: Resistance before and after processing steps

Sample	Release Procedure	R_{before}	R_{after}	$R_{\text{after}}/R_{\text{before}}$
1	Freeze dry	7.5 k Ω	152 k Ω	20
2	Freeze dry	12.3 k Ω	1470 k Ω	120
3	Freeze dry	3.72 k Ω	23.5 k Ω	6.3
4	Liquid	3.17 k Ω	11.7 k Ω	3.7
5	Liquid	3.54 k Ω	46 k Ω	13
6	Liquid	3.05 k Ω	16.6 k Ω	5.4

Following either of these “release” procedures, samples were imaged by a Hitachi S-4000 field emission scanning electron microscope (SEM) to identify suspended nanotubes. The suspended nanotubes are fairly robust. In addition to imaging by SEM they can also be imaged by tapping mode AFM with no damage. Shown in Figure 4-8 is tapping mode image of a suspended nanotube sample and the corresponding SEM image of the same nanotube.

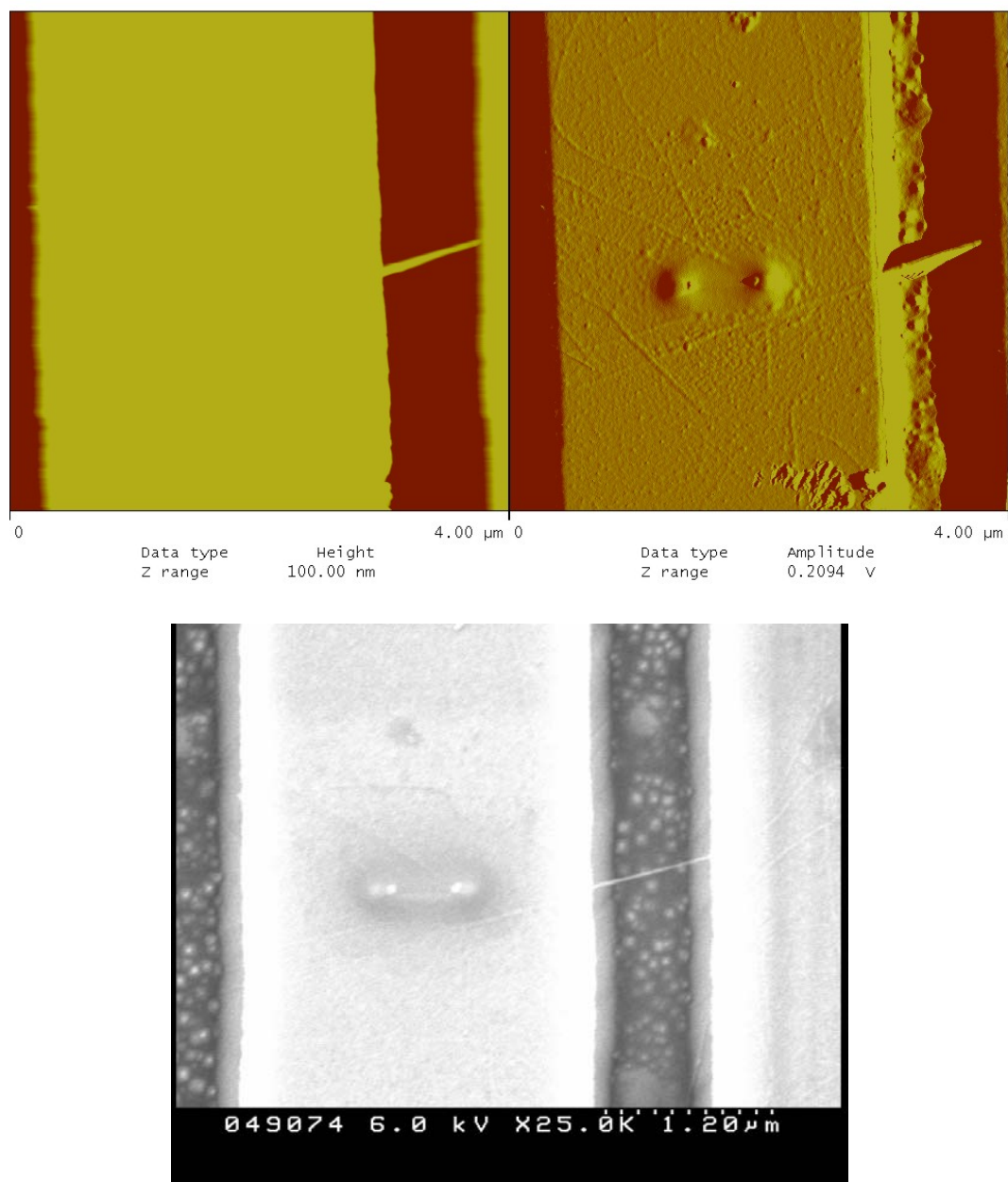


Figure 4-8: Suspended carbon nanotube images. A) Height tapping mode AFM image of a suspended nanotube. It can be clearly seen that the nanotube is suspended and intact. B) AFM deflection image -more detail on the surrounding area can be distinguished. C) SEM image of the same nanotube

4.1.6 Identification of Suspended Nanotubes

One of the difficulties of an experiment such as this is being able to locate the suspended tubes with the AFM tip. Fortunately we were able to exploit an unwanted by product from the SEM to make this process easier. Prolonged exposure of a substrate to

the electron beam in a SEM usually results in the build up of a deposit generated from the breakdown of residual hydrocarbons in the chamber under the electron beam irradiation. After finding a suitable suspended nanotube, we moved directly over to the electrode pinning it and did a prolonged line scan on the electrode. After the mark was deposited a SEM image was taken of the mark and its relative position to the suspended tube. Thus once the mark was found by the AFM tip, the distance to the nanotube could be found by referring to the position of the mark in relation to the nanotube in the SEM image.

Another SEM image was taken referencing the created marks to some type of larger fiduciary marking (such as a corner or defect in the lithography). Thus a map of the marks is produced. An example is shown in Figure 4-9.

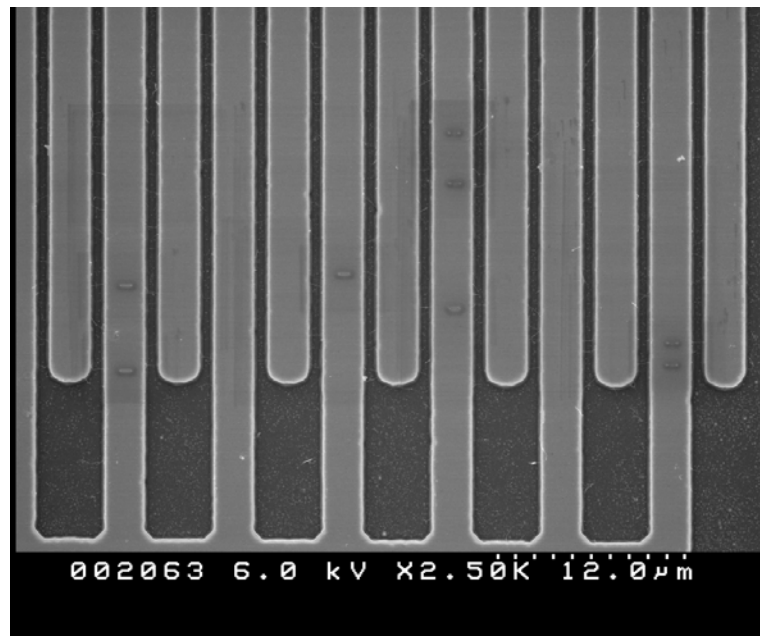


Figure 4-9: SEM image of a map of the created marks.

5.1.7 Final Sample Preparations

After marking the sample, the chip was permanently attached to a polished AFM puck with conducting silver epoxy. The epoxy was carefully molded around the edges of the chip to create smooth sloping walls reaching from the top of the sample down to the

puck. A shadow mask masked off the center electrode area, containing the suspended nanotubes, and metal was deposited over the entire puck/chip assembly. This extra layer of metal electrically connected the large electrode pads (and consequently the small electrodes pinning the nanotubes) to the AFM puck.

Finally, the experiment itself was done in the liquid electrolyte environment and thus, the samples had to be carefully submerged again. In this case, we immersed the chips into the low surface tension TMS. As no liquid evaporates in this procedure, the purity of the TMS is not an issue. In the reverse of the previously mentioned “release” procedure, the liquids were slowly exchanged for those with higher surface tensions with the last liquid being the electrolyte solution used in the experiment. Experiments were performed using 0.1 M to 1 M solutions of NaCl in water, NaNO₃ in water, LiClO₄ in acetonitrile, and LiBF₄ in acetonitrile.

4.2 Experimental Procedure

All experiments were done in an AFM electrochemical cell and a Digital Instruments Nanoscope III AFM. This special AFM tip holder is manufactured out of glass so the laser can still reflect off of the cantilever and reach the split photodiode. The cell has a center chamber with an o-ring groove surrounding it. As the cell is lowered closer to the sample surface the o-ring compresses and forms a seal between the glass sidewalls of the electrochemical cell and also the AFM sample puck. To load the sample in the electrochemical cell, the greased o-ring was submerged into a beaker containing both the immersed sample and the electrolyte. The o-ring was carefully placed on the AFM puck so that it surrounded the mounted silicon chip and is illustrated in Figure 4-10. This allowed removal of the puck from liquid while still keeping the suspended SWCNTs submerged in the small pool of electrolyte within the o-ring walls.

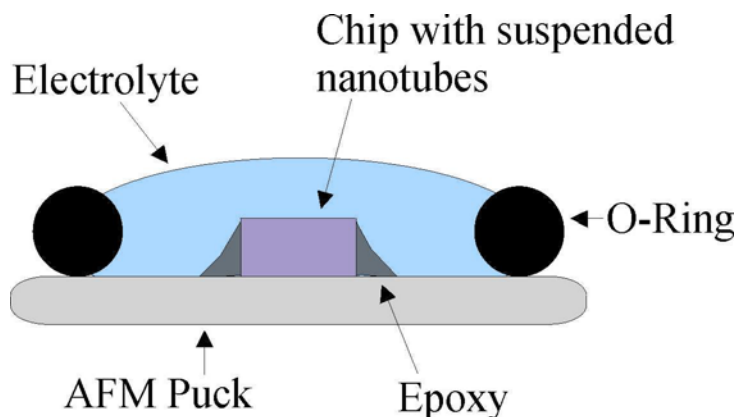


Figure 4-10: Cross sectional schematic of chip mounted on AFM puck during transfer to the AFM.

During the actuator experiment voltages were applied using a three terminal setup with a Princeton Applied Research Potentiostat/Galvanostat model 283. The three terminal arrangement includes a working electrode, a counter electrode, and a reference electrode immerse in an electrolyte. The reaction of interest occurs at the working electrode. Whenever a metal is immersed in a solution a potential drop occurs at the boundary of the electrode and electrolyte. There is no way to independently measure this without introducing another electrode into the solution, which in turn has its own potential drop at the interface. In a two terminal measurement chemical reactions at the working and counter electrodes can cause the potential drop at the interface to be different from the applied potential. Thus the actual difference between the two electrodes is unknown. A reference electrode has high impedance and is chosen so that it provides a stable and reproducible potential against which the working electrode potential can be controlled. Thus any changes that occur in the cell potential occur at the working electrode and not the reference. The reference electrode is designed to reproduce the same potential regardless of the solution the working electrode is in. The counter electrode is an inert metal (usually Pt) that completes the circuit.

The electrochemical cell had 3 ports which we made use of. The first port was connected to a syringe that could be use for adding and exchanging the electrolyte solution. While not in use, the syringe was disconnected and the port sealed. The second port connected to a small glass tube that housed the reference electrode (Ag/AgCl for the aqueous experiments and Ag/Ag^+ for the acetonitrile runs). Between the glass tube and AFM port was a porous Vycor frit. This frit allowed the ions in solution to pass while not allowing solvent exchange. Finally, the third port contained the counter electrode. We opted to use a strip of bucky paper due to its high surface area and thus large capacitance. The working electrode was the nanotube sample and voltage was applied to it through the AFM piezo cap.

Prior to use in the electrochemical cell, the electrolyte solution was sparged with helium. Sparging removes dissolved gases from liquids by bubbling an inert gas through the liquid. Air bubbles have the possibility of interfering with the experiment in a variety of ways. An air bubble above the cantilever can interfere with the laser reaching the photodiode and disrupt the measured signals. An air bubble in either the reference or counter electrode port causes a discontinuity in the electrolyte solution and thus would break the conduction path. In the case of a bubble in the counter electrode line the sample simply would not get the potential we were trying to apply. In the case of a bubble in the reference electrode line the potentiostat would apply the maximum voltage between the counter and working electrode and destroy the nanotube sample. The electrolyte solution was sparged for about 15 minutes before loading.

Upon loading the sample and tip into the liquid environment we observed an enourmous drift in the free space deflection signal of the cantilever. After an initial huge drift the deflection signal change would slow down but not completely dissipate. This

has often been attributed to thermal drift in the literature. However, this explanation is completely inadequate since the cantilever is better thermally coupled to its environment in a liquid than it is in air. This drift was far too large to allow performance of the experiment requiring that its source be determined to continue. We ultimately determined that this drift was due to chemical interactions between the tip and the liquid surroundings. The heat from the laser reflecting off the metal-coated backside of the cantilever would increase the rate of these reactions and would often etch the reflective coating. To fix this problem, we deposited (in a home built system) a thin (~50nm) conformal layer of parylene C on the tip.⁴⁰ Parylene C is a polymer deposited from the vapor phase that is both chemical inert and electrically insulating. The basic procedure for parylene deposition involves subliming the dimer, di-para-Xylylene, in a moderate temperature zone (95°C), decomposing the dimer into the monomer in a high temperature zone (680°C), and spontaneous polymerization of the polymer on a cooled surface (20°C). By isolating the tip from the solution we eradicated the drift, yielding a stable deflection signal. Figure 4-11 shows the drift of the free space deflection signal over 3 hours for two tips, one bare tip and one coated with parylene, in aqueous 1M NaNO₃. The AFM tips were calibrated by the reference cantilever method⁴¹ after application of the parylene coating.

To find the marked nanotubes with the AFM, the tip was engaged on the large electrode pads in the near a fiduciary mark. Once the end of the electrode was found, the tip was translated down the electrode (by the amount indicated from the SEM map) until the mark was located. The marks are quite large (heights of several hundreds of nanometers and lengths around a micron) and are easily imaged with the AFM, Figure 4-

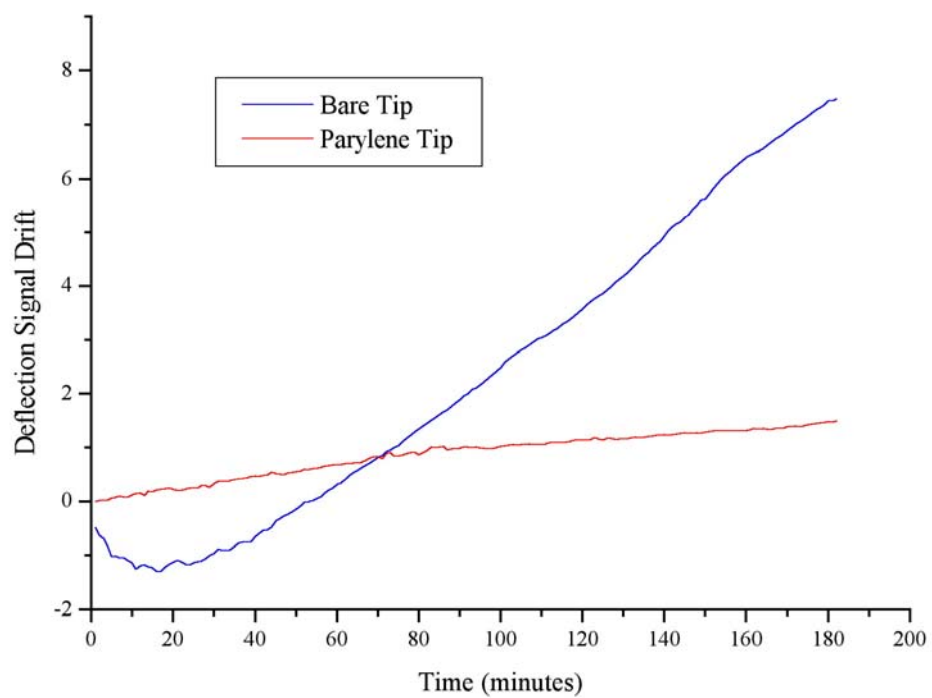


Figure 4-11: Free-space drift of a bare tip and a paralyne coated tip in aqueous 1M NaNO_3

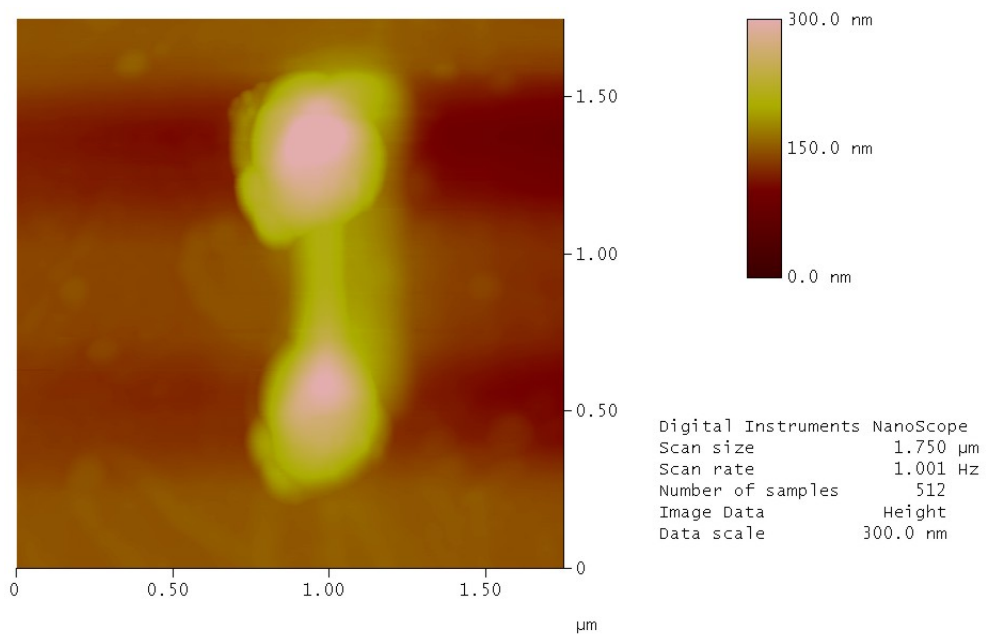


Figure 4-12: AFM image of identifying mark created in the SEM

AFM imaging performed in the fluid environment was done in contact mode. Contact mode AFM uses a soft cantilever that is in intimate contact with the surface while the sample is rastered back and forth. In the Digital Instruments Multimode AFM the piezo motion is all that of the sample stage (the tip is stationary except for its Z deflection caused by interaction with the sample). A laser is bounced off the back of the cantilever (which has been coated with a reflective metal) to a split photo diode detector. Before the tip is contacted with the surface to be imaged, the position of the detector is usually adjusted so that the measured laser intensity striking the top portion of the split photo diode equals that striking the bottom portion (the free space value is set to zero). Once in contact, the stage will move upward deflecting the tip until the signal on the split photodiode reaches the deflection setpoint set by the user. The amount of force exerted by the cantilever on the sample is determined by the difference between the free space setpoint and the deflection setpoint. While engaged with the surface, vertical deflections of the cantilever are detected as differences in the laser intensity on the top and bottom halves of the split photodiode. The force applied by the cantilever is equivalently that of a spring, $F=Kx$, with the bending force constant, K , of the cantilevers being calibrated prior to use and x being the actual tip deflection.

After located the mark, we used the AFM in an unconventional way to make contact with the nanotube. If the deflection setpoint is set to a value below the free space deflection the sample will move down away from the tip in an effort to decrease the value measured by the photodiode to the user defined setpoint. Once the mark was found the scan size was set to zero, the feedback gain was reduced (to make the rate of piezo response to differences between the setpoint and the signal slow) and the deflection setpoint was chosen to be below the free space signal in order to move the sample away

from the tip. To stop the Z motion once the tip was disengaged from the surface the feedback gain was set to zero. At this point the X and Y positions of the stage were adjusted such that the tip would be placed directly over the suspended SWCNT. To guarantee minimal stress to the nanotube a low setpoint just above the free space value was chosen and the gains were set to a very low level. This caused the stage to be brought up very slowly as the nanotube came in contact with the tip. Once the tip reached its setpoint while tensioning the nanotube, the gains were raised back to their original value.

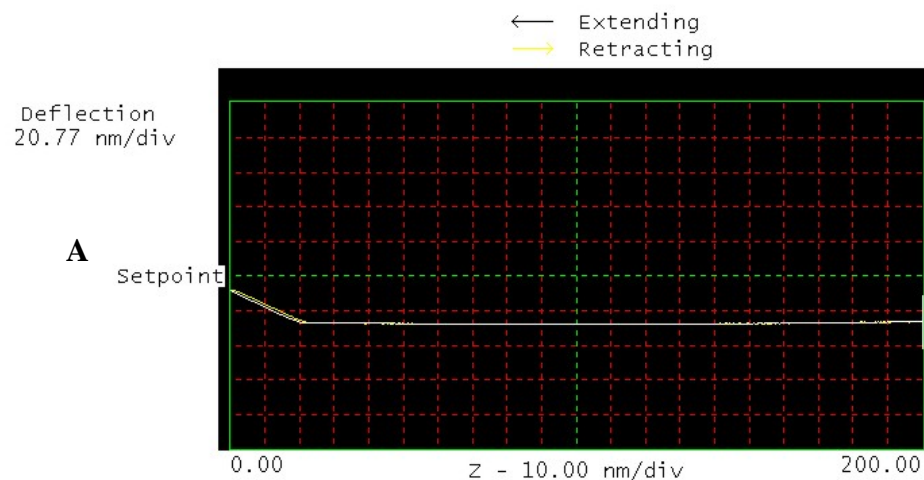
To accurately find the nanotube, the tip was lifted and lowered several times while making small increments along the length of the trench until the highest spot, and thus the position of the nanotube, was located. Once found by this method, force calibration curves against the nanotube were taken to extract essential information and to verify that the object the tip located was truly a nanotube. Force calibration mode is a useful feature within contact AFM. In this mode the sample stage is repeatedly moved up and down while plotting the tip deflection against the Z position of the stage as shown in Figure 4-13A.

The right side of the plot corresponds to the stage being furthest from the tip. The white line is the deflection signal of the cantilever as the stage moves toward the tip and the yellow is the deflection as the stage retreats. The deflection signal remains flat until a surface is hit, at which point the tip begins to deflect. The stage will move until the tip reaches the user-defined setpoint.

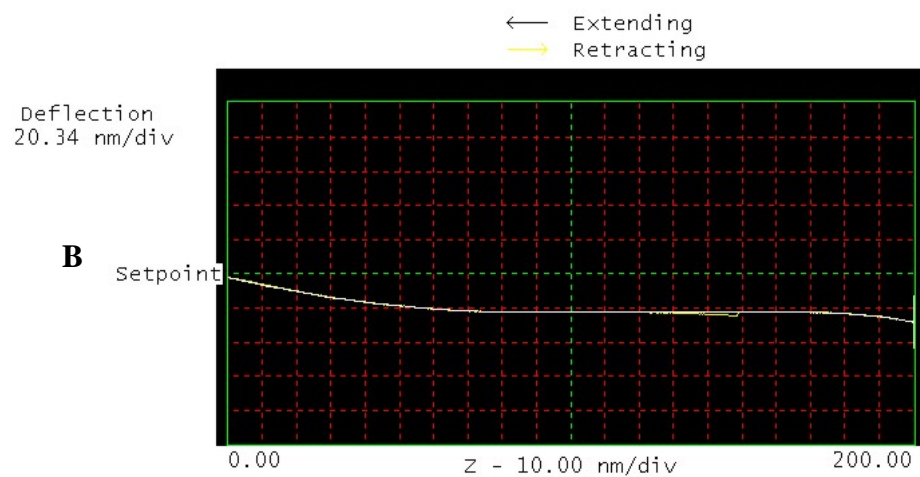
Against a hard surface the tip deflection will equal the Z movement, as any movement by the stage will cause the same amount of deflection in the tip (this permits calibration of the tips Z deflection signal in volts to a distance since the displacement of

the piezoelectric stage, per volt applied to it is known). However, against an object that stretches, like a nanotube, the Z movement will be greater than the tip deflection, the difference being the amount of vertical deformation of the object. A schematic drawing of the tip against both a hard surface and a nanotube is shown in Figure 4-14. This difference made it easy to recognize a nanotube being tensioned versus say the bottom of the trench. Because they are elastic, when the tip first comes in contact with the tube it stretches easily. The nanotube becomes harder to stretch as the tip continues to press on it and the curve begins to straighten. Figure 4-13A is a force calibration curve against a metal electrode while Figure 4-13B shows a force calibration curve against a suspended SWCNT using the same tip as in Figure 4-13A.

The force causing this stretch is calculated by multiplying the force constant of the cantilever (measured before loading the sample) by the deflection of the tip. The number of nanotubes in a rope can be approximated from parameters derived from the force calibration curve.



Digital Instruments NanoScope
 Ramp channel Z
 Ramp size 200.0 nm
 Scan rate 1.969 Hz
 Z scale 207.7 nm



Digital Instruments NanoScope
 Ramp channel Z
 Ramp size 200.0 nm
 Scan rate 1.001 Hz
 Z scale 203.4 nm

Figure 4-13: Force calibration curves against two surfaces. A) Against a hard surface. B) Against a suspended nanotube

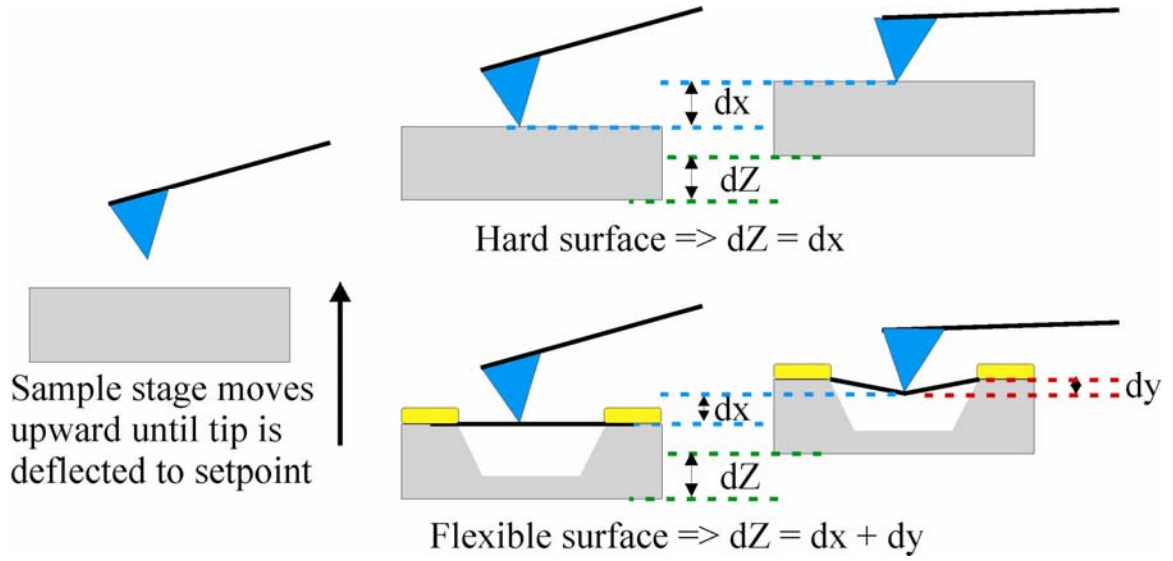


Figure 4-14: Illustration of a force calibration curve against a hard surface and nanotube.

The original vertical stretch of the nanotube, the initial deflection designated by y and illustrated in Figure 4-15, is calculated by subtracting the deflection of the tip from the Z movement of the sample stage while the tip and nanotube are in contact. Simple statics considerations give the force needed to deflect the nanotube a vertical distance y as,

$$F := 2 \cdot k \cdot \left[1 - \frac{L_0}{\left(y^2 + L_0^2 \right)^{\frac{1}{2}}} \right] \cdot y \quad (4.1)$$

k is defined as

$$k = Y \cdot A / L_0 \quad (4.2)$$

Y is the Young's modulus (10^{12} Pa) for graphene. A is the cross sectional area of the nanotubes under tension. The cross sectional area for one nanotube is the van der Waals thickness for graphite ($t = 0.34 \times 10^{-9}$ m) multiplied by the circumference of the nanotube ($\pi \cdot d$ where d is the diameter of the tube) Thus the total cross sectional area for a rope of

nanotubes is $n \cdot t \cdot \pi \cdot d$ where n is the total number of nanotubes in the rope. This gives the following expression for k .

$$k := \frac{n \cdot Y \cdot t \cdot d \cdot \pi}{L_0} \quad (4.3)$$

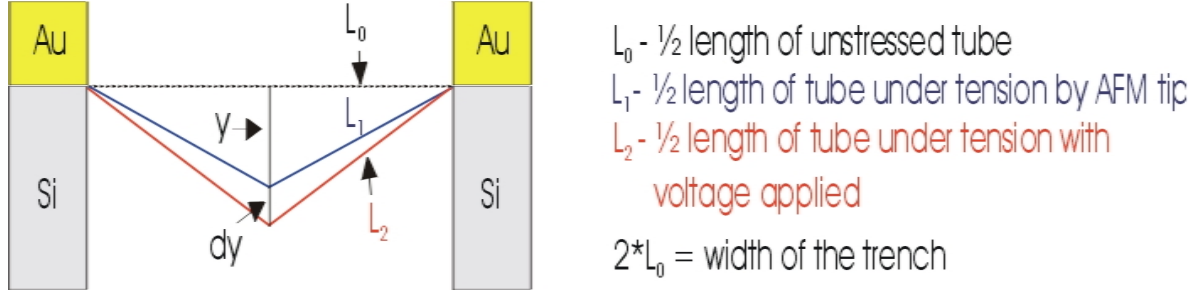


Figure 4-15: Diagram of nanotube under tension.

The parameter y is essential to calculating the observed actuation. The tensioned length of the nanotube is $L_1 = (L_0^2 + y^2)^{1/2}$ where L_0 is the same as mentioned above. Any actuation of the nanotube will cause a deflection of the cantilever by dy as the tube lengthens or contracts. Using dy we can calculate the new length of the tensioned tube as $L_2 = (L_0^2 + (y+dy)^2)^{1/2}$. Thus the actuation strain $\delta L/L$ is defined as $\delta L/L = (L_2 - L_1)/L_1$. It is instructive to plot dy as a function of y for a given amount of actuation, i.e. setting $\delta L/L$ to a constant, as shown in Figure 4-16. The parameters L_0 of 430nm and $\delta L/L$ of 0.0001 (corresponding to an actuation of 0.01%) were used.

The value of dy decreases sharply with increasing y . Once this particular tube has been stretched past $y=18\text{nm}$ the value of dy becomes less than 1nm. In order to observe actuation with the AFM tip, the nanotube must be under some tension but the amount of initial stretch needs to be small in order to have any sensitivity to the effect.

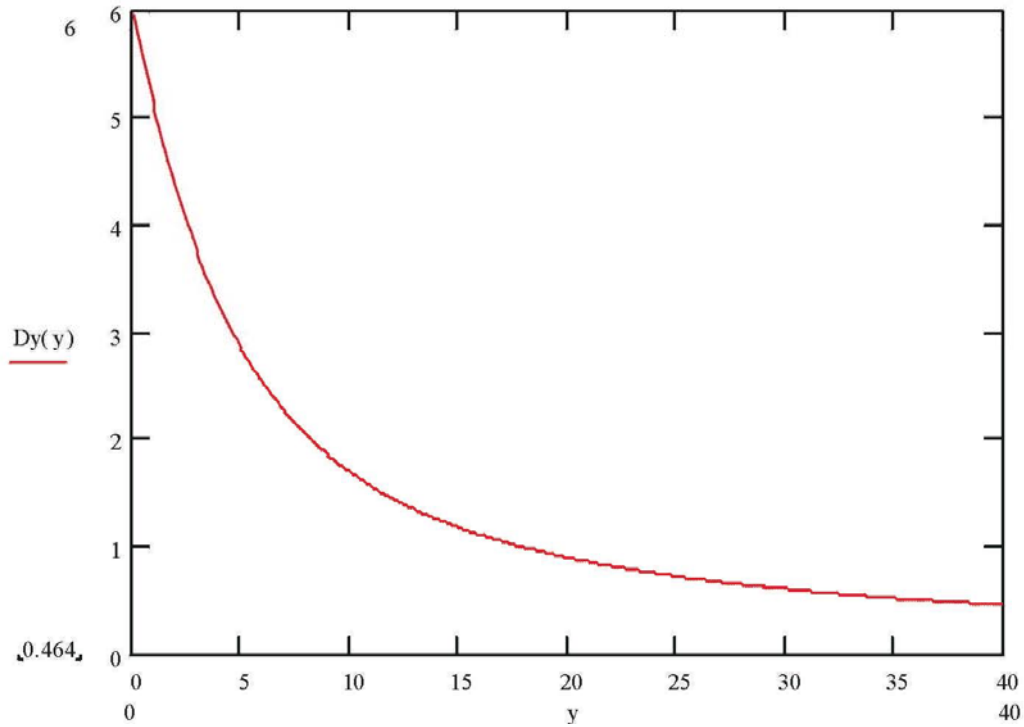


Figure 4-16: Plot of dy versus y for $L_0=430\text{nm}$ and $\delta L/L=0.0001$. Both y and dy are plotted in nanometers.

After the tip tensioned the nanotube by the amount y , as measured by the force calibration curve, voltage was applied to the electrodes through the piezo cap of the AFM. Elongation or contraction of the nanotube resulting from the applied voltage will cause a deflection of the cantilever. A Princeton Applied Research Potentiostat/Galvanostat model 283 controlled all applied voltages to the three electrodes. A square wave potential with a low frequency of either 0.5Hz or 1 Hz was used. Data of the applied voltage, current, and piezo movement in the Z direction was recorded with a Labview program. Usually, data was taken for different values of pre-tension y and different applied voltages on each nanotube. Several runs were taken with each variation in parameter.

CHAPTER 5

RESULTS AND DISCUSSION OF CHARGE INDUCED ACTUATION OF SUSPENDED CARBON NANOTUBES

5.1 Results of Actuation Measurements

The experiment was performed on 35 suspended nanotubes. Several distinct electrolytes were used. Aqueous NaCl, aqueous NaNO₃, LiClO₄ in acetonitrile, and LiBF₄ in acetonitrile were employed in concentrations ranging from 0.1 M to 1 M. The organic solvents were used to obtain a larger voltage window than the hydrolysis of water permits. Square wave voltages were applied up to 2 Volts peak to peak. During some runs only negative voltage was applied to the sample since the bond length changes are expected to be greater for electron injection compared to electron withdrawal. The parameter monitored to detect dimensional changes in the nanotube was the Z voltage supplied to the piezo, a change of 1 V corresponded to 12.9nm. Changes in the nanotube length caused the AFM tip to either relax below or be pushed above the setpoint. The sample stage would move to compensate for this change in length so that the setpoint was restored. Out of the 35 samples only 3 nanotubes displayed length changes that could be duplicated in more than one run.

Sample 1 is shown in Figure 5-1. As measured from the SEM image the parameter L_0 is 484nm. This sample was immersed in 1M aqueous NaCl solution. An example data run is shown in Figure 5-2 and a summary of all the data runs for this nanotube is listed in Table 5-1. The parameter y is the initial vertical deflection of the tube as measured by the force calibration curves, dZ is the voltage change in the AFM piezo corresponding to the vertical nanotube changes, dy is the dZ voltage from the

piezo converted into nanometers (12.9nm/Volt), and % dL/L is the percentage strain of the nanotube.

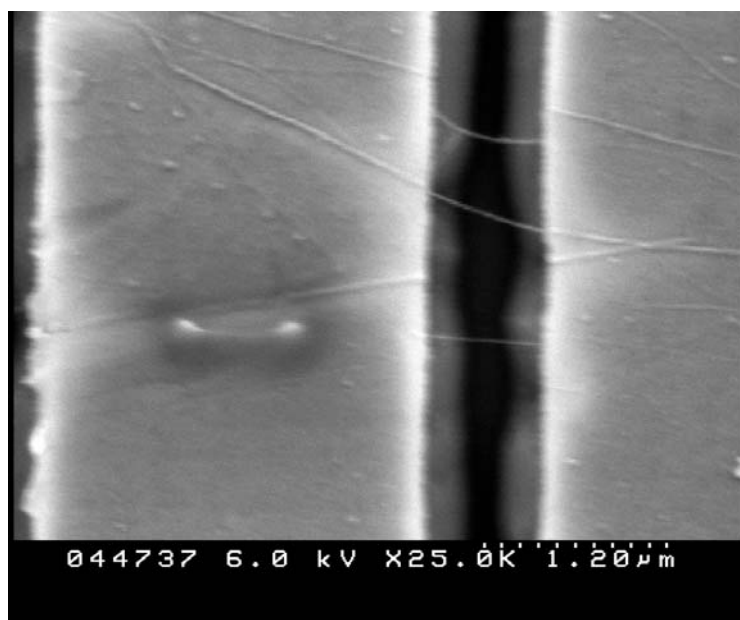


Figure 5-1: SEM image of nanotube sample 1. The nanotube of interest is the thin tube directly to the right of the mark

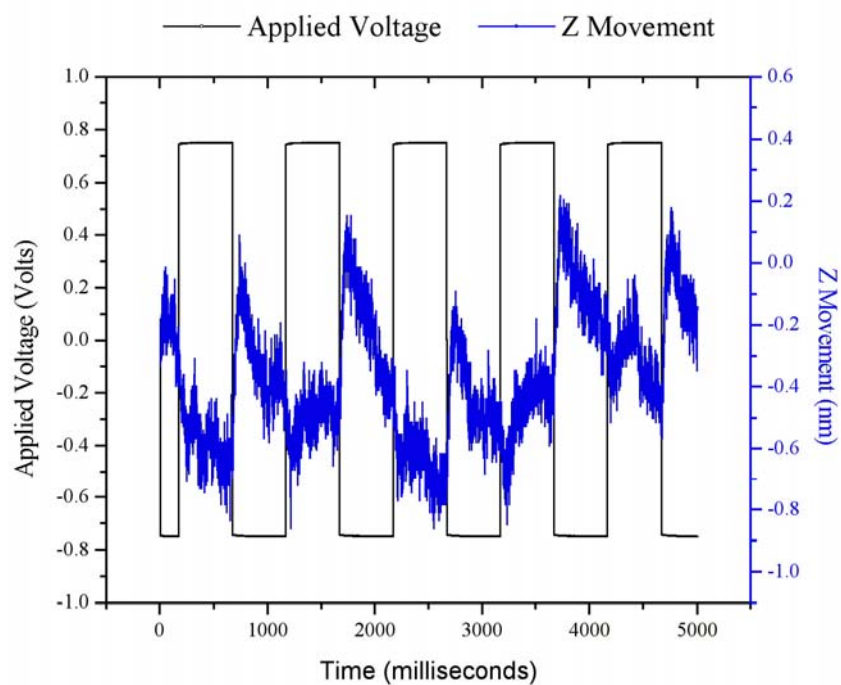


Figure 5-2: A data file from sample 1. The applied voltage is shown in black with its scale on the left. The Z piezo movement is shown in blue

Table 5-1: Summary of data from sample 1

Run	Y (nm)	dZ (V)	Dy (nm)	% dL/L
1	36.9	0.0269	0.346	0.00544
2	36.9	0.0175	0.225	0.00354
3	14.3	0.0206	0.265	0.00163
4	14.3	0.0189	0.243	0.00150

Nanotube sample 2 is shown in Figure 5-3. This sample was exposed to polyethylene imine (PEI) prior to loading in the AFM electrochemical cell. PEI has been shown to n-dope the nanotubes.⁴² In graphite, bond length changes for the same amount of charge transfer are smaller if the sample is already p-doped but larger if the sample is n-doped. PEI is an extremely viscous liquid and was dissolved in methanol from concentrations starting at 2.5% and increasing to 20%. The suspended nanotube sample was first carefully submerged in methanol which was slowly exchanged for the 2.5% PEI solution. This was repeated 4 times with subsequently higher concentrations of PEI solution with the final step resulting in the sample residing in the 20% PEI mixture. To adsorb the PEI onto the nanotubes the sample was left submerged overnight. The following morning the sample went through the reverse of the process, with the liquids being exchanged for lower concentration solutions of PEI. The PEI solution was exchanged for pure methanol and that was exchanged for water at which point another freeze dry was performed. From the SEM image of this sample the parameter L_0 was determined to be 429nm. This experiment was performed in 0.5M LiBF₄ in acetonitrile. As sample of a data file is shown in Figure 5-4 and a summary of the parameters from all data files for sample 2 is shown in Table 5-2

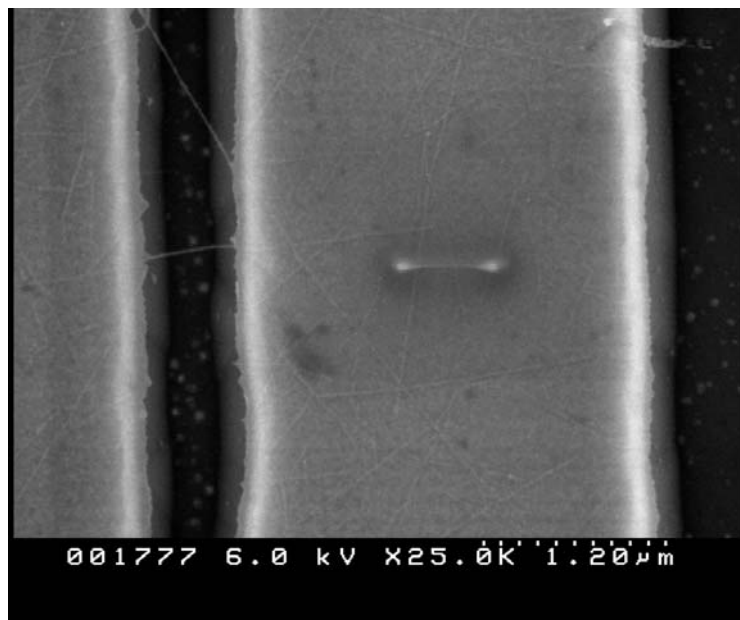


Figure 5-3: SEM image of nanotube sample 2. The nanotube is to the left of the mark.

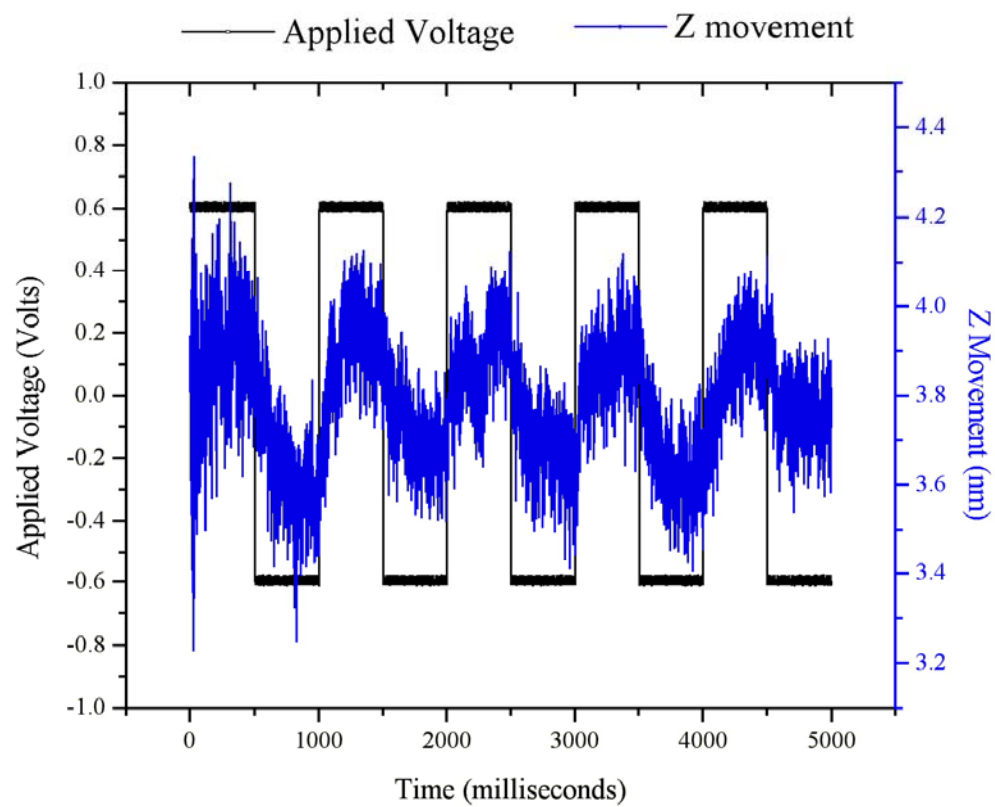


Figure 5-4: Sample 2 data

Table 5-2: Summary of data for sample 2.

Run	y (nm)	dZ (V)	Dy (nm)	% dL/L
1	18.4	0.0134	0.172	0.00178
2	18.4	0.0104	0.134	0.00134
3	11.4	0.0151	0.194	0.00121
4	11.4	0.0230	0.296	0.00186

Sample 3 was also submerged in 0.5 LiBF₄ in acetonitrile. From the SEM image shown in Figure 5-5 the parameter L_0 was determined to be 444nm. Figure 5-6 displays the data from one run and Table 5-3 is a summary of all the data runs for sample 3.

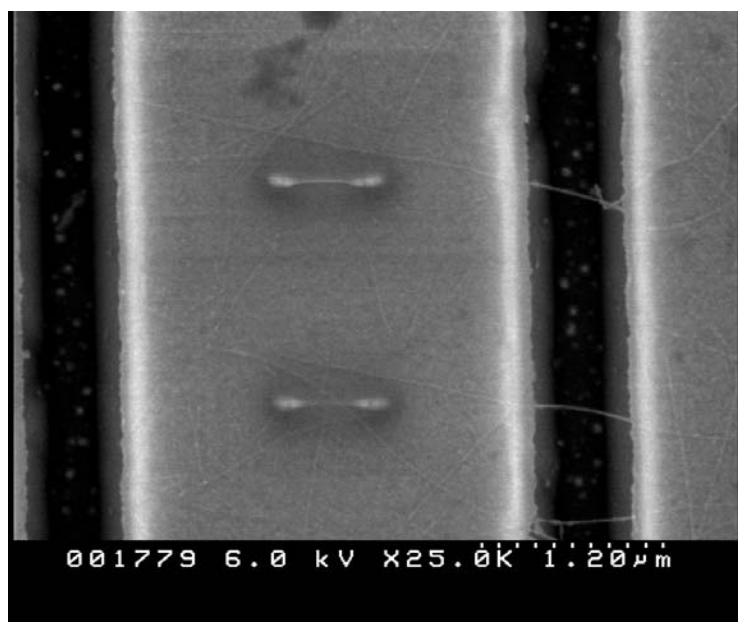


Figure 5-5: Image of sample 3. The nanotube measure is the one to the left of the lower marking.

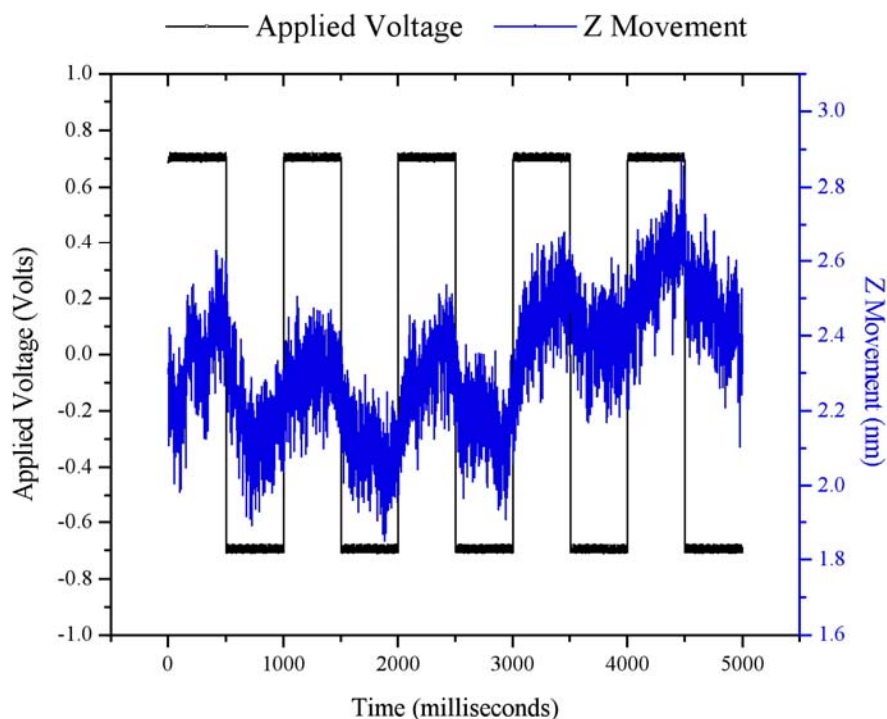


Figure 5-6: Sample data file from nanotube 3.

Table 5-3: Summary of all data from sample 3

Run	y (nm)	dZ (V)	dy (nm)	% dL/L
1	16.8	0.0102	0.131	0.00112
2	16.8	0.0112	0.144	0.00123
3	16.8	0.00800	0.103	0.000878
4	14.6	0.0115	0.148	0.00110
5	14.6	0.0119	0.153	0.00114
6	14.6	0.0109	0.140	0.00104

To ascertain whether the discrete jumps observed in the in the Z movement from the application of voltage to the nanotubes where a result of nanotube actuation or from some type of chemical reaction in the cell other data files were also taken. These include monitoring the Z movement while the tip was suspended in the electrolyte but not in contact with anything as shown in Figure 5-7. Additionally data was taken with the tip in contact with the bottom of the silicon trench, Figure 5-8.

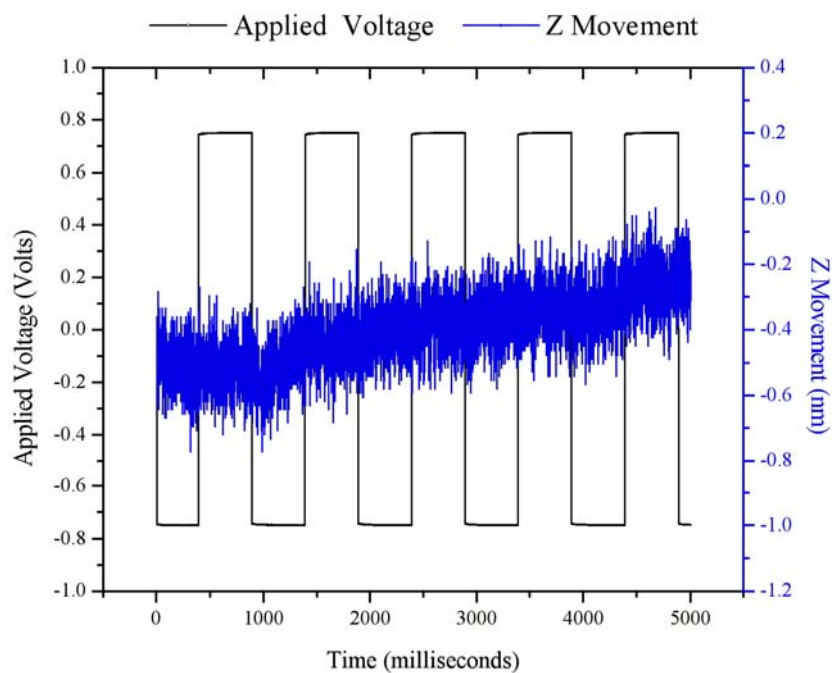


Figure 5-7: Data of the Z Movement and applied voltage while the AFM was suspended in free space

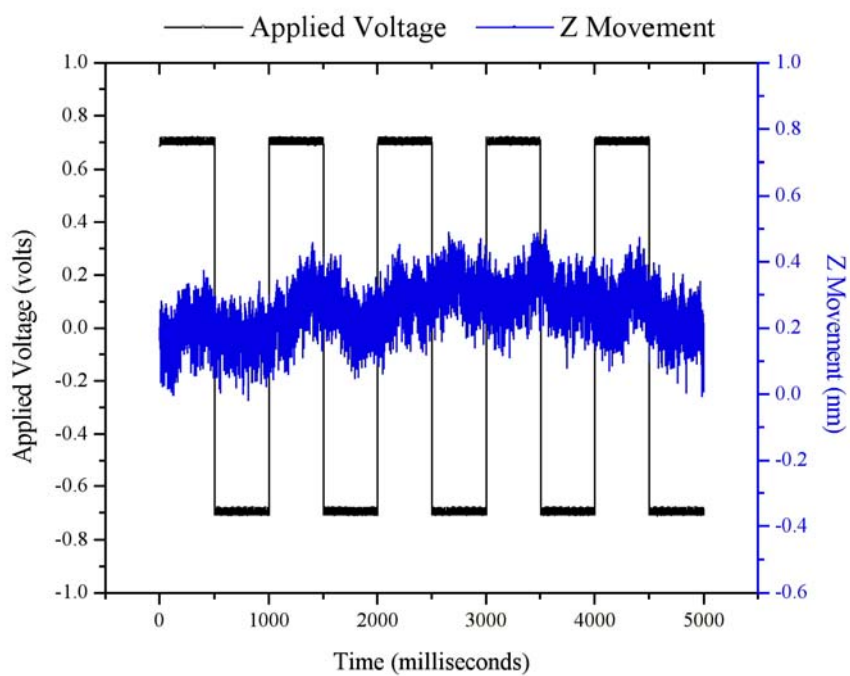


Figure 5-8: Data of Z Movement and applied voltage while the AFM tip was in contact with the bottom of the trench.

A summary of all the data with average actuation values is listed in Table 5-4.

Table 6-4: Summary of the actuator data

Sample	Electrolyte	Applied Voltage (peak to peak)	L_0 (nm)	Y (nm)	D_y (nm)	% Actuation
1	1M NaCl in H ₂ O	1.5 V	484	36.9	0.285	0.0045
2	0.5M LiBF ₄ in CH ₃ CN	1.2 V	429	11.4	0.245	0.0015
3	0.5M LiBF ₄ in CH ₃ CN	1.4 V	444	14.6	0.147	0.0011

5.2 Discussion of Results

The experiment performed by Baughman *et al.*⁸ observed much higher actuation strains in the macroscopic sheets. For an applied voltage of 0.9 V_{pp} the strain was nearly .1%. Since the nanotubes were bundled, with only the outer nanotubes presumed to be undergoing actuations, these values were estimated to be lower limits to nanotube actuation. Based on their results, the authors speculated that the maximum strain for individual nanotubes could reach ~1%/V. Our measurements fall far short of that prediction and are smaller than that observed for the nanotube sheets.

This lack of evidence for charge-induced actuation in our work led us to reexamine some of our fundamental assumptions. The first question that needed to be asked was “how much charge can a nanotube hold?” And once that has been determined, “how much strain is predicted for this amount of charge injection. To answer the first question we calculated the capacitance of a carbon nanotube under these conditions. Previously, Krüger *et al.*⁴³ and Rosenblatt *et al.*⁴⁴ had used MWCT and SWNT in electrolyte gated transistors. Both groups had calculated the capacitance per unit length of the nanotube within the electrolyte solution using the geometry of two concentric cylinders.

$$C = 2 \pi \epsilon_0 \epsilon / \ln(R_2/R_1) \quad (5.1)$$

The inner cylinder is the nanotube whose radius is given as R_1 in the equation. The value they used for the outer cylinder diameter R_2 was that of the nanotube, R_1 , plus the Debye length, λ_D , for the ionic concentration of the solution. They also used the accepted value of $\epsilon=80$ for dielectric constant of water. Both groups used electrolyte concentrations of 1mM which gives a Debye length of $\lambda_D=1\text{nm}$. Using these values the two groups calculated gate capacitance values of $\sim 10\text{ nF/m}$ or 10^{-17} F/nm ($62.5\text{ e}^-/\text{nm/V}$). This use of the bulk dielectric constant of water responsible for such large capacitance values is however not correct in the case of electrolytes where the effective spacing between electrodes is the width of the electric double layer.

In electrolyte solutions, when a voltage appears on an immersed electrode (in this case the nanotube) the ions of the opposite polarity will migrate toward the electrode to neutralize the charge. Thus the composition of the electrolyte solution near the interface is different than the rest of the bulk solution generating the outer half of the electrochemical double layer (the inner half being the charge on the electrode). The layer of charge at the surface of the electrode and the concentration of opposite charges in the solution surrounding the electrode generate a capacitance. However calculation of the double layer capacitance is non trivial and remains an active area of research and debate (e.g. see chapter 2 reference 45). For example, what is the location of the counterions surrounding the electrode? The most accepted arrangement is the Gouy-Chapman-Stern-Grahame model. In this model part of the potential drop occurs from a layer of fairly closely packed counterions near the surface, the Helmholtz layer. The rest of the potential drop occurs over a diffuse section of ions in which electrostatic forces compete with Brownian motion. For solutions with a concentration of 1M or higher generally the entire drop takes place over the compact Helmholtz layer and the influence from the

diffuse layer is only a minor correction. The positions of the ions near the electrode are also influenced by the dipole moments of the water molecules surrounding them.

Conversely, the electric fields generated by the ions in solution and the electrode also affect the water dipole moments and can change the dielectric constant. This effect was noticed as early as 1948 by Hasted *et al.*⁴⁶ who tried measuring the modified dielectric constant in aqueous salt solutions. The ions in solution orient the water molecule dipoles. The water molecules in the immediate vicinity of an ion are immobilized by the ion's electric field. The ion is referred to as hydrated. Figure 5-9 shows an illustration of hydrated Na and Cl ions

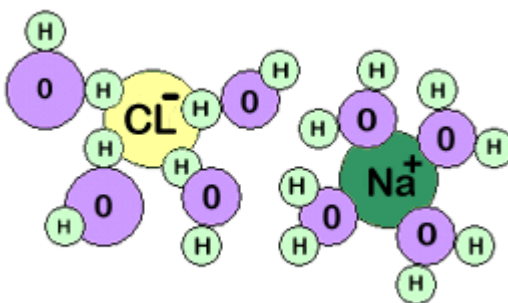


Figure 5-9: Hydrated Cl^- and Na^+ ions

The polar water molecules are no longer free to rotate in response to the applied external electric field, which is what imparts to water its large bulk dielectric constant. The presence of ions in the water breaks up the water network and decrease the overall dielectric strength, something known as dielectric saturation. The dielectric strength for a water-counterion complex for Na is $\epsilon_{\text{Na}} \sim 2$ and the radius of a hydrated Na ion is $r = 0.36 \text{ nm}$.^{47,48} If we use this radius as the distance to the outer cylinder in our capacitance equation we have to use the drastically reduced value of $\epsilon_{\text{Na}} = 2$ for the dielectric constant. Using these values (and $R_1 = 1.36 \text{ nm}$, the diameter of a (10,10) nanotube) the calculated capacitance goes to $C = 2.6 \times 10^{-19} \text{ F/nm}$ ($1.6 \text{ e}^-/\text{nm/V}$). This value

is more than order of magnitude smaller than what was estimated by Krüger *et al.*⁴³ and Rosenblatt *et al.*⁴⁴. In one nanometer of length for a SWCNT with a diameter of $d=1.36\text{nm}$ we have 160 C atoms. Using this information we can convert to electrons per carbon atom.

$$C=(1.6\text{ e}^-/\text{nm/V})(1\text{ nm}/160\text{ C atoms})=0.01\text{ e}^-/\text{C-atom/V}. \quad (5.2)$$

So for sample 1 that had 1.5 volts peak to peak applied to it, we can expect that the amount of charge injection was $q = \pm 0.0075\text{ e}^-/\text{C-atom}$. The theoretical work on SWCNT dimensional changes discussed in Chapter 3 give an average of 0.1% strain for the addition of $0.01\text{ e}^-/\text{C}$. Hence for $0.0075\text{ e}^-/\text{C-atom}$ calculated from the capacitance we should expect a strain of 0.075%. While acetonitrile (bulk $\epsilon=37.5$) was used as the solvent in a number of the experiments the same considerations can be expected to apply.

Results from a spectro-electrochemical study on carbon nanotube thin films in the Appendix give further support to this capacitance estimate. Carbon nanotubes have optical absorbance peaks centered around 1650 nm and 900 nm. These peaks are due to photoinduced electronic transitions between valence to conduction band van Hove singularities. The 1650 nm and 900 nm peaks correspond to the 1st and 2nd van Hove singularities for semiconducting nanotubes. The peaks are broad because of the range of nanotube diameters in the sample and also because of perturbations to the electronic structure from tube to tube interactions. The absorbance peaks can be reduced or even eliminated by shifting the Fermi level. If electrons (holes) are added then the singularity in the conduction (valence) band will be filled (depleted) and no electronic transitions, and thus absorption of photons, will be possible.

From these measurements we can determine at what applied voltage the first van Hove singularity is either depleted or filled. At an applied voltage of negative -0.7 V the

first peak has started to shift but the second has not, Figure A-4. Note that the peak has not been completely removed. That is to be expected the sample contains bundles of nanotubes. At low applied voltages the Fermi level of an outlying nanotube has been shifted while the Fermi level of an inner lying tube remains untouched. Since there is no change in the second peak we assume that even the outer tubes have not had their Fermi levels shifted into the second singularity yet. We determined the additional e^-/C atom when the Fermi level was shifted to the point just before the second semiconducting van Hove singularity by using a program that calculated the density of states for nanotubes of any indices (n,m). The method was based on zone folding of the tight binding 2D energy dispersion relations of graphite (Equation 2-11) and a simple rotation transformation of k_x and k_y into k_\perp and k_\parallel (relative to the nanotube axis).⁴⁹ A graph of the density of states for a (10,11) semiconducting nanotube and the shifted Fermi level are shown in Figure 5-10. Integrating the density of states up to the dashed line in this figure gives 0.005 e^-/C -atom. From the results in the appendix an applied voltage of -0.7Volts therefore corresponds to an additional charge of 0.005 e^-/C . We also did the same calculation for a (10,10) metallic nanotube with the Fermi level shifted the same amount and found an additional 0.007 e^-/C -atom. Using $V=0.7V$ in our capacitance calculations (Equation 5.3) yields .007 e^-/C -atom which is in reasonable agreement for the two values. It should be noted that the calculation for the capacitance (Equation 5.3) assumes the nanotube is a perfect metal able to accommodate unlimited additional electrons. Since the nanotubes are limited in the number of additional electrons they can contain by the density of states, the derived formula for capacitance is likely an overestimate.

Despite the reduced capacitance, the results of Baughman *et al.*⁸ are around what would expected so capacitance alone cannot explain our small results. However, their

sample also contained bundled nanotubes. Since the strain would be shared by the inner nanotubes, which would not be undergoing dimensional changes, the actual strain of the outer nanotubes would be greater than that displayed by the nanotube sheet.

Additionally, their results display some reversals in the actuations (Figure 3-2) at voltages of 0.5V and up that cannot be explained by bond length changes from additional charges in the π orbital system. That behavior is very similar to an effect caused by double layer charging in porous graphite in which changes in the interfacial tension within the pores cause dimensional changes in the graphite.⁵⁷

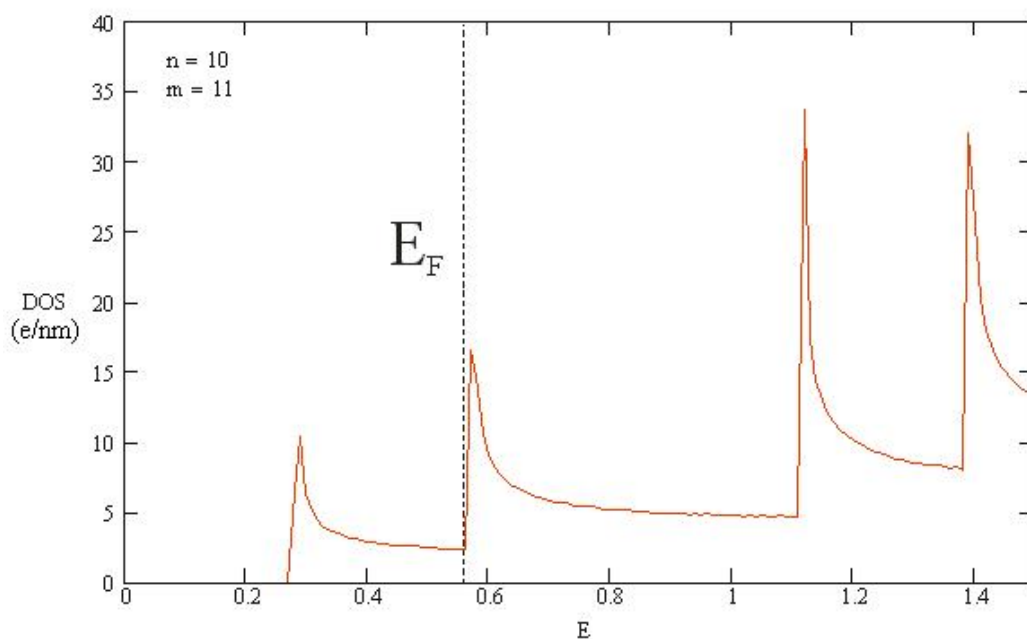


Figure 5-10: Density of states for a (10,11) SWCNT.

The SWCNT film used in the spectroelectrochemical experiment in the Appendix was baked to remove any dopants acquired during purification. However, the transmittance minimum for the peak associated with the first semiconducting optical transitions occurred between -0.2V and -0.4V . That is where the point of zero charge (PZC) on the nanotube film would occur. This indicates that the nanotubes were p-doped

by their exposure to electrolyte (which has its own chemical potential) atmosphere despite the desorbing bake. The experiment by Baughman *et al.*⁸ used aqueous 1M NaCl. For graphite in 1M NaCl the PZC is -0.2 V ^{55,56,57} so it is likely the PZC of the nanotube film would also be negative. As mentioned, the dimensional changes in graphite (for the same amount of charge transfer) that is already p-doped will be smaller than the changes in un-doped graphite.

Even accounting for the reduced dielectric constant, the predicted strain is still larger than what we measured. One of the difficulties within the nanotube field has been making good contacts to the one dimensional SWCNTs. SWCNT field effect transistors (FETs) made with metals that were consistent with our fabrication process have been found to be consistently p-type, even with good ohmic contacts for the on state.^{50,51,52,53,54} It has been suggested that strong dipole moments of adsorbed gases (particularly oxygen) at the contacts modifies the barriers and this effect leads p-type behavior.⁵³ Additionally, there is a barrier introduced by mismatch in work functions of the contact metal and the nanotube.

Rosenblatt *et al.*⁴⁴ formulated water gated nanotube FETs. Like our work, they used an electrolyte solution to gate the nanotube and also contacted the tubes with Cr/Au electrodes. They found that small diameter nanotubes (3nm and under) were still p-type. Even using the electrolyte gate they could not push across the band gap to get electron transport. The results in the Appendix show that nanotube films can be pushed across the gap. However only a very small portion of the nanotubes in a film are in contact with the metal contact electrode and thus only that small portion would be p-doped by the contacts. But individual nanotubes (like the ones used in our experiment and that of

Rosenblatt *et al.*⁴⁴) are sufficiently p-doped by the contacts so that the Fermi level cannot be shifted into the conduction band.

These issues result in two factors that explain why charge induced dimensional changes in these experiments is so small. Contact barriers with nanotubes prevent electron injection in semiconducting nanotubes. And perhaps more importantly, the fact that the nanotubes are p-doped puts the nanotubes into the portion of the strain versus charge transfer curve where the length changes are smaller (see Figure 3-3). Attempts to inject sufficient electrons to take the nanotubes to the steeper part of the curve require pushing the semiconducting tubes across the gap while the metal electrode contact with the nanotubes result in Schottky barriers that further impede such electron injection. Using an extremely low work function metal (such as Ca) would n-dope the nanotubes and cause barriers favorable to electron injection. However, those metals are incompatible with the processes required to the suspended nanotube samples. Thus we are prevented from measuring significant charge induced dimensional changes in individual nanotube because of effects resulting from the contacts.

CHAPTER 6

CONDUCTANCE CHANGES IN CARBON NANOTUBES DUE TO HYDROGEN

The work in this chapter demonstrates the utility of carbon nanotubes as hydrogen gas sensors. Parallel efforts demonstrated that sputtering of metals onto SWCNT decreases the intrinsic conductance of the nanotubes.

6.1 Carbon Nanotube Sensor Background

The first demonstrated use of nanotubes as chemical sensors was by Kong *et al.*⁵⁸ They monitored the charge transport changes of semiconducting SWCNTs when exposed to NH₃ and NO₂. These early sensors patterned source and drain electrodes on individual nanotubes in a field effect transistor (NFET) configuration. Upon exposure to electron-withdrawing NO₂ the turn on voltage of the NFET was shifted by +4V. When exposed to electron donating NH₃ the turn on voltage was shifted by -4V. The interaction of these molecules with the SWCNT shifted the Fermi level, through the density of states of the nanotubes, modulating their response to the gate voltage.

Other groups have since then tested the effect of various gases on the conductance of carbon nanotubes using either individual tubes, bundles of tubes, or thin films of SWCNTs.^{59,60,61,62} The observation has been that electron donating species cause a decreased conductance of the p-type semiconducting nanotubes and electron withdrawing molecules increase the conductivity. These sensors all had long recovery times (hours) although exposure to UV light or elevated temperatures helped speed up the desorption process.

Recent efforts have focused more on using thin films of nanotubes as sensors. Novak *et al.*⁶³ used chemical vapor deposition to grow a nanotube network on a SiO₂/Si substrate that was just above the percolation threshold. These films were used to detect several electron donating molecules including dimethyl methylphosphonate, DMMP (a simulant for the nerve agent sarin). This group was the first to use the clever method of applying a positive back gate to refresh the device. They surmised that the Coulombic repulsion between the negative charges induced by the gate and the negative charge donated by the DMMP was enough to lower the desorption barrier and drive off the DMMP. Although these devices are in some sense easier to manufacture than individual nanotube FETs, consistent growth of a nanotube film near the percolation threshold can be difficult.

The number of chemicals forming charge transfer complexes with the nanotubes, and which may therefore be detected by this mechanism, is rather limited. Y. Lu *et al.*⁶⁴ first demonstrated the detection of methane, which does not by itself undergo charge transfer with SWCNTs, by loading the SWCNT film with palladium particles. The sensors were formed by first sputtering a 10nm thick layer of Pd onto SWCNT powder and mixed by shaking this concoction. The metal-coated powder was dispersed in deionized water, sonicated, and drop-dried onto an interdigitated electrode pattern. This work certainly showed the utility of loading SWCNTs with metals but the method of associating the nanotubes with the metal was poorly controlled as was the density of the nanotubes bridging the electrodes.

The work presented here focuses on using SWCNTs loaded with Pd particles for the detection of hydrogen gas. During the course of this work another group published a

paper also using Pd-SWCNTs as H₂ sensors.⁶⁵ This group deposited Pd onto the nanotubes by RF sputtering and also by using a technique in which a Pd salt solution (containing SWCNTs) was reacted with toluene to deposit Pd particles on the nanotubes. After Pd loading, the SWCNT films were deposited by airbrushing a suspension of nanotubes in ethanol onto an aluminum substrate. Contrary to the high sensitivity of sputtered Pd-SWCNT presented here, this group had no sensitivity to H₂ with the sputtered Pd-SWNT samples. Additionally, we observed higher $\delta R/R$ ratios for amounts of H₂ at least an order of magnitude smaller.

Palladium is an interesting choice for metal loading of SWCNT H₂ sensors for a couple of reasons. At room temperature and atmospheric pressure palladium can adsorb up to 900 times its own volume of hydrogen. Additionally, palladium has been shown to make ohmic contacts with carbon nanotubes. Javey *et al.*⁵⁴ used Pd electrodes to form semiconducting nanotube FETs. Upon exposing the devices to H₂ they demonstrated a decrease in the conductance of the p-type semiconducting nanotubes. It was speculated that this was because the adsorbed H₂ lowers the work function of the palladium. Earlier experiments testing the change in resistance of discontinuous Pd films upon exposure to hydrogen claimed an increase in the palladium work function.^{66,67,68} As pointed out by Bari⁶⁶ the relevant mechanism is that hydrogen adsorption lowers the Fermi level of the palladium, thus causing an increased Schottky barrier for hole transport.

Hydrogen detection is important in a variety of areas including semiconductor fabrication clean rooms, space missions where H₂ is used as fuel and wherever H₂ could cause an explosive mixture. The current efforts toward a hydrogen based fuel economy

further emphasize the need to find dependable low power H₂ sensors. The goal of this work was to produce a reliable, easy to fabricate, H₂ sensor made from carbon nanotubes.

6.2 Carbon Nanotube Sensor Fabrication

We fabricated two types of SWCNT sensors, both coated with a thin layer of Pd metal. The first involved tens of CVD grown nanotubes wired between parallel electrodes spaced roughly 1 micron apart. The second type involved ultra thin nanotube films made from pulsed laser vaporization bulk produced SWCNTs .

The first type, from hereon called the micro-device sensor, was fabricated using p type <100> silicon chips with a 600nm thermal oxide layer. Using the same techniques discussed in Chapter 4, the chips were cleaned, nanotubes grown by CVD, and photolithography used to form an interdigitated¹⁴ electrode pattern. The lengths of the electrodes are 500 μm so there are many nanotubes in parallel between two adjacent electrodes. The pattern is shown in Figure 6-1.

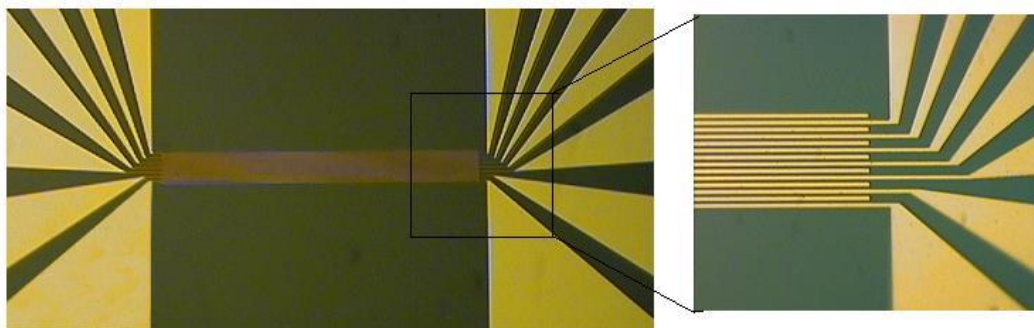


Figure 6-1: Electrode pattern on micro-device nanotube sensor.

The ultra thin nanotube film sensors were manufactured using a technique described by Wu *et al.*⁶⁹ Purified SWCNTs grown by laser ablation were suspended in an aqueous 0.5% Triton-X solution with a nanotube density of 0.001 mg/mL. The nanotube film was formed on a membrane by vacuum filtering the solution onto a mixed

cellulose ester membrane (0.1 μm pore size, Millipore). After the film was formed the Triton-X was washed away with DI water. The film thickness was easily controlled by the amount of the nanotube suspension filtered. To transfer the nanotube film to the desired substrate the film was adhered to the substrate by wetting with water and pressing between metal plates until the water dried. The mixed cellulose ester membrane was then dissolved away by acetone leaving the ultra thin nanotube film behind. Films made with this technique can be as thin as a few nanometers.

The nanotube thin film sensors were fabricated on cleaned silicon substrates with a 600 nm SiO_2 layer. Nanotube films with nominal thickness of 7nm and 25nm were used are shown in Figure 6-2. Step heights of thicker films (50 nanometers) were measured by AFM and correlated to the amount of nanotube solution used. The 7nm and 25nm heights of the films are estimates found by scaling down the amount of solution. As seen in Figure 6-2b, the 7nm film effectively sub-monolayer.

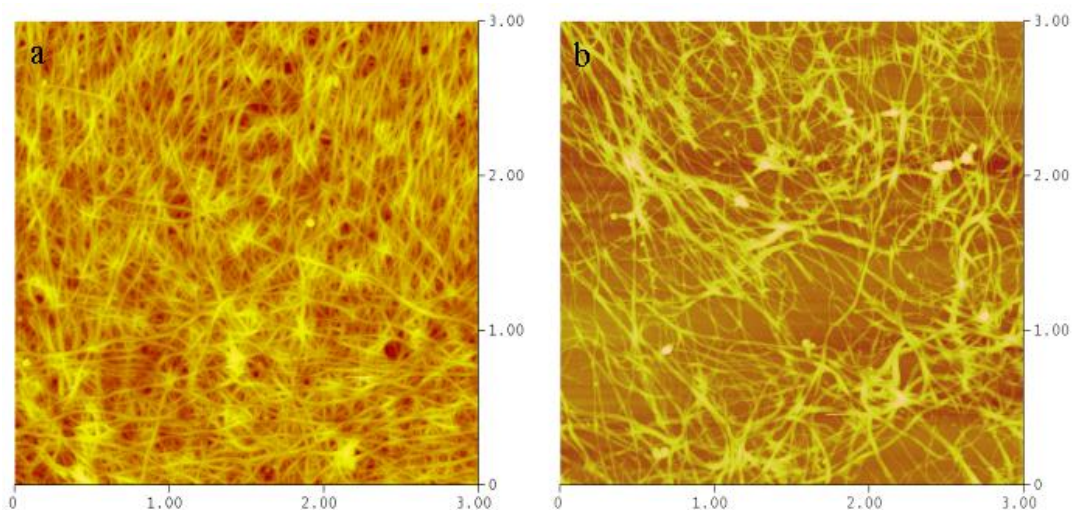


Figure 6-2: AFM images of a) 25nm SWCNT film and b) 7nm SWCNT film

The films were deposited on the silicon chips as follows. After washing the nanotube film on the membrane it was allowed to dry. Pieces, of the ultimately desired

film size were then cut from the membrane, wetted with DI water and placed nanotube side down onto the silicon chip. The substrate was sandwiched between several pieces of filter paper for cushioning and pressed by spring clamps between two metal plates. After the water evaporated, aided by placing the samples in a 95° C oven for an hour, the nanotube film/filter membrane was attached to the substrate. To remove the mixed cellulose ester filter, the silicon chips were transferred to an acetone vapor bath. The membranes dissolved in the acetone vapors leaving only the nanotube film. The samples subsequently went through five additional acetone baths followed by a methanol wash to ensure the complete removal of the membrane polymer. The samples were baked in an inert gas to desorb remaining contaminants and nanotube dopants. To give volatiles a chance to escape before they reacted with the nanotubes the oven was ramped at a slow rate under the following schedule: 5° C/min to 110° C, held for 30 min, then 1° C/min to 600° C, held at temperature for 2 hours and and powered off to cool to room temperature. Contact pads of Cr/Pd were deposited across the ends of the SWCNT film by either sputtering or thermal evaporation. A photograph of the SWCNT film sensor device is shown in Figure 6-3.

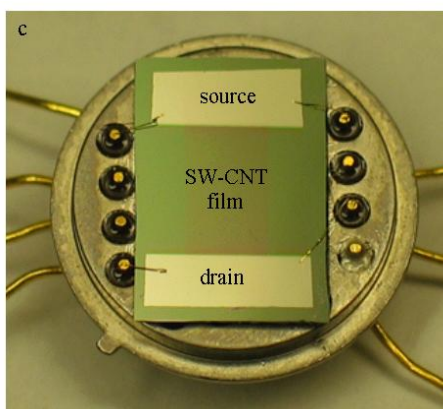


Figure 6-3: SWCNT thin film sensor wired for measurement. Bright regions labeled source and drain are Pd metal pads. Voltage is applied across the source and drain while the current, passed through the SWNT film, is measured

6.3 Resistance Changes from Metal Deposition

As will be discussed in the next section, both the micro-device and the film sensors show miniscule response to H_2 at this stage. To be sensitive to the gas we deposited thin, in some cases non-percolating, layers of palladium on top of the nanotubes by either sputtering or thermal evaporation. The samples were masked such that Pd was deposited only onto the nanotube films. Surprisingly, the resistance of all the nanotube samples coated with sputtered Pd increased. As this situation is analogous to two parallel conductance paths (the nanotube film and the metal layer) the increase in resistance is contrary to expectations, which would have the resistance decreasing. Table 6-1 shows the increase in the resistances of three samples, a micro-device sample, a 7nm film and a 25nm film, (AJA International ST10 magnetron source, 3 W power, 5 mT Ar, 5 s deposition time). 600 nm oxide-on-silicon witness chips, having the same source/drain electrodes but no nanotube films rode along with each nanotube sample during the thin Pd layer deposition. These showed the Pd films to be sub-percolation in all these cases.

Table 6-1: Resistance changes of nanotube samples with sputtered Pd

Sample	R_{before}	R_{after}	$R_{\text{after}}/R_{\text{before}}$
Micro-device	1.33 k Ω	5.32 k Ω	4.0
7nm film	3.18 k Ω	6.69 k Ω	2.1
25nm film	829 Ω	1.34 k Ω	1.6

The resistance of several SWCNT films was monitored before and after the deposition of thermally evaporated Pd incorporating similar witness chips. In several of these cases the witness chips exhibited finite resistances demonstrating that the amount of metal deposited was above the percolation threshold. This point and the resulting resistance will of course depend on the substrate upon which the metal is deposited

(nanotubes for the films and SiO₂ for the chips), nevertheless to first order, we take the resistance of the metal layer measured on the witness chips to be that of the metal layer on the nanotubes. Table 6-2 lists the before and after resistance of several nanotube film samples with varying amounts of thermally evaporated Pd, as well as the resistance of the witness chips. . In each instance the resistance of the nanotube films decreased however the decrease varied with the amount of Pd. Films 1 and 4 had roughly a 5nm thick Pd film deposited on top (measured *in situ* by an Inficon quartz crystal thickness monitor). The resistance of the Pd layer on top of Film 1 is smaller than the resistance of Film 1 itself and is comparable in height. The final resistance is greater than the value calculated by combining the resistance of the nanotube and the Pd film in parallel ($R_{||}=1.24\text{ k}\Omega$ compared to $R_{\text{after}}=1.72\text{ k}\Omega$). Similarly the final resistance of Film 4 is also larger than the calculated parallel resistance ($R_{||}=0.785\text{ k}\Omega$ compared to $R_{\text{after}}=0.993\text{ k}\Omega$). Films 2 and 3 had Pd layers between 2nm and 2.5nm deposited. The final resistance of these films is smaller than the calculated parallel resistance.

Table 6-2: Resistance changes on SWCNT films with thermally evaporated Pd

Sample	Nanotube film height	R_{before}	R_{after}	$R_{\text{Pd film}}$	$R_{\text{after}}/R_{\text{before}}$
1	7nm	5.72 k Ω	1.72 k Ω	1.58 k Ω	0.30
2	7nm	8.86 k Ω	3.45 k Ω	90.0 k Ω	0.39
3	7nm	5.76 k Ω	4.82 k Ω	non-percolating	0.84
4	25nm	1.46 k Ω	0.993 k Ω	1.70 k Ω	0.69

Both metallic and semiconducting nanotubes have been shown to be ballistic conductors with resistances per nanotube approaching the theoretical limit of 6.5 k Ω .^{70,54} However, the resistance across nanotube films between macroscopically spaced electrodes is dominated by the resistance across tube to tube contacts, which constitute tunnel junctions.^{71,72,73} The data shows that when less metal is evaporated on the

nanotube films the resistance across the films is lowered by an amount greater than consideration of the parallel (nanotube/metal) conductance while when more is evaporated the resistance (while still lowered) is lowered by an amount less than the parallel conductance. Given the ballistic on tube conductance a simple view would suggest that by increasing the electrical contact area across tube-tube contacts the resistance across the films should be greatly lowered. We can make sense of the data by recognizing that it is naïve to assume that a singled walled nanotube associated with metal along its length retains its ballistic conductance. We conclude that the better than parallel path resistances of films 2 and 3 are due to lowered tube to tube resistance arising from increased contact area at the junctions due to the Pd particles which however are discontinuous and do not coat long sections of the nanotubes. Too much metal, which coats long sections of the nanotube sidewalls, interferes with their ballistic conductance. Both theoretical calculations and experimental evidence support this view.^{74,75}

Regardless of the method of deposition the palladium coated the nanotubes. Figure 6-4 shows AFM images of two 7nm films, one coated with sputtered Pd and the other by thermally evaporated Pd. The morphological differences between the two films are likely due to the variation in the rates of deposition. Both films are ~10-30 Angstroms thick but the sputtered film was deposited in 10 seconds while the thermally evaporated film was grown in 80 seconds. Higher deposition fluxes result in smaller grain sizes and more even coverage while slower rates allow the metal time to diffuse along the nanotubes and coalesce into the larger grains seen in Figure 6-4b.⁷⁶

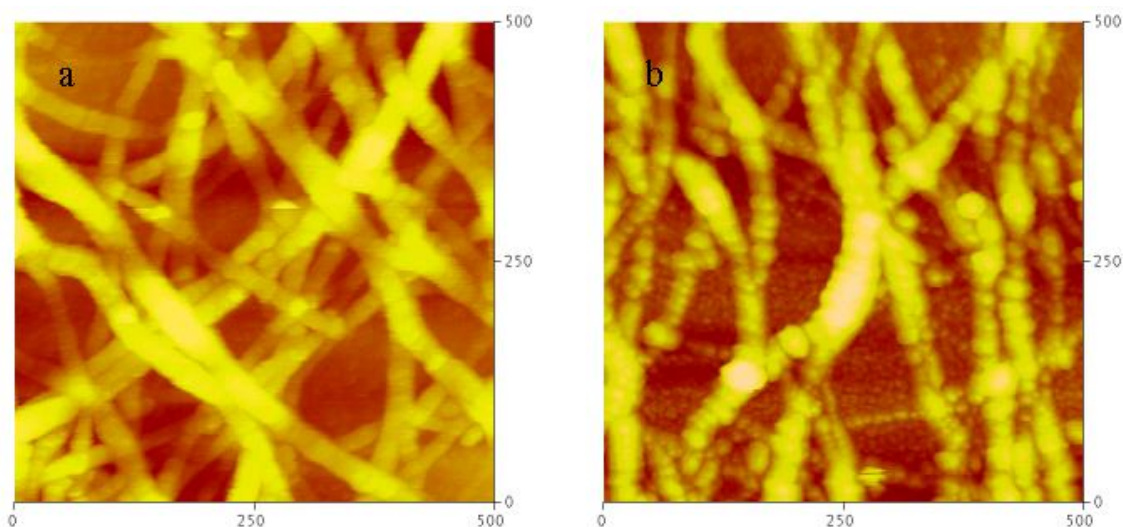


Figure 6-4: AFM images of Pd coated nanotube films a) sputtered and b) thermally evaporated

To determine if the increase in nanotube resistance after sputter deposition was confined to Pd we also sputter deposited a thin film of Au onto similar samples (in a different sputtering system), again obtaining an increased resistance. . In light of these results we additionally conclude that sputtering damages the nanotubes changing their intrinsic conductance. The three sputtered samples in Table 6-1 had the Pd deposited at the same time so the amount of Pd was the same for each sample. The 25nm film had the smallest amount of resistance increase, a factor of 1.6, while the micro-device resistance increased by a factor of four. Every nanotube in the micro-device would be exposed to and damaged by the sputtering plasma causing the largest change in resistance. In the thicker sample (25nm film) many of the underlying nanotubes would be shielded from the plasma by the tubes on top. Thus only a portion of the nanotubes would be damaged resulting in a smaller increase in resistance.

6.4 Conductance Changes due to Hydrogen Exposure

Resistance changes in the nanotube devices upon exposure to H_2 were monitored for several different samples. Data was taken for samples both with and without the thin Pd layer. We also compare the response of a 7nm film coated with thermally evaporated Pd to that of a sputter coated film. Additionally, the response to H_2 of a thin Pd film without nanotubes was monitored.

The samples were exposed to H_2 at room temperature and atmospheric pressure in a quartz flow tube with electrical feed-throughs for voltage and current leads. The gases were fed via mass flow controllers to maintain a total flow of 450 sccm of either pure nitrogen, 500 ppm hydrogen in nitrogen or a mixture of the two to obtain reduced concentrations of hydrogen, or compressed air humidified by passing through a water bubbler. Electrical measurements were performed with an HP4156B source-meter.

6.4.1 Pure SWCNT Samples

A micro-device sensor, a 7nm film and a 25nm film without any additional metal besides the contact pads were all tested for sensitivity to H_2 (Figures 6-5, 6-6 and 6-7 respectively). The current was monitored as a function of time at constant bias (0.5V) for varying H_2 concentrations. At $t=14$ minutes the samples were exposed to air to recover their initial conductance.

The pure nanotubes in the micro-device sensor show absolutely no sensitivity to H_2 . At the highest H_2 concentration of 500ppm the uncoated 7nm and 25nm films show decreases in the current of 1.5% and 1.6% respectively. These comparatively small changes (compare below) are probably entirely due to changes occurring within the nanotubes at the Pd/nanotube contacts as opposed to the bulk uncoated nanotube film.

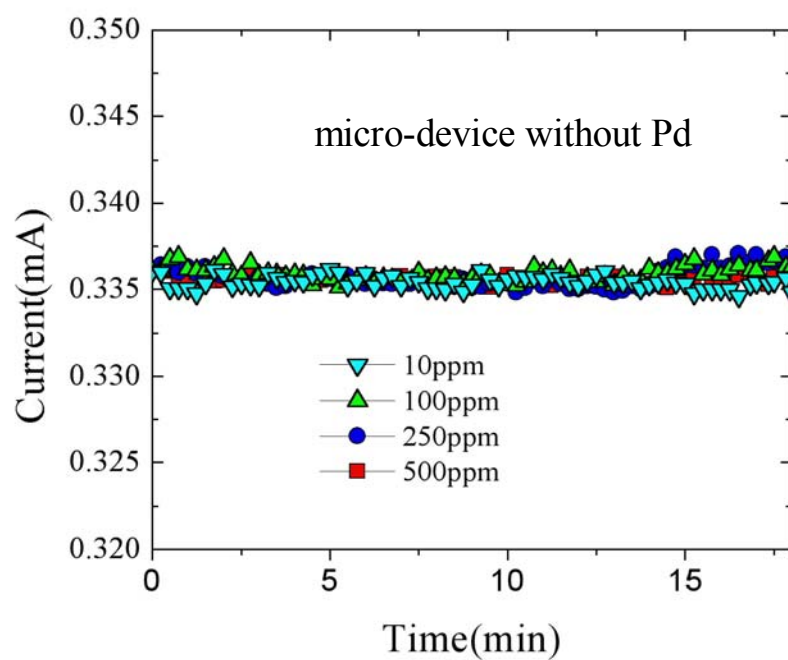


Figure 6-5: Current vs. time measurement for micro-device sensor exposed to different H₂ concentrations.

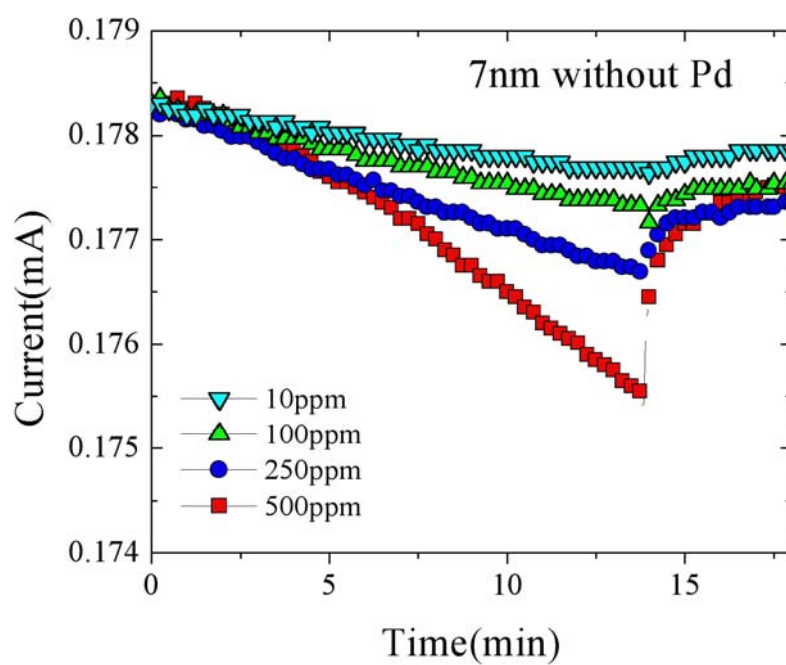


Figure 6-6: Current vs. time measurement for 7 nm film exposed to different H₂ concentrations.

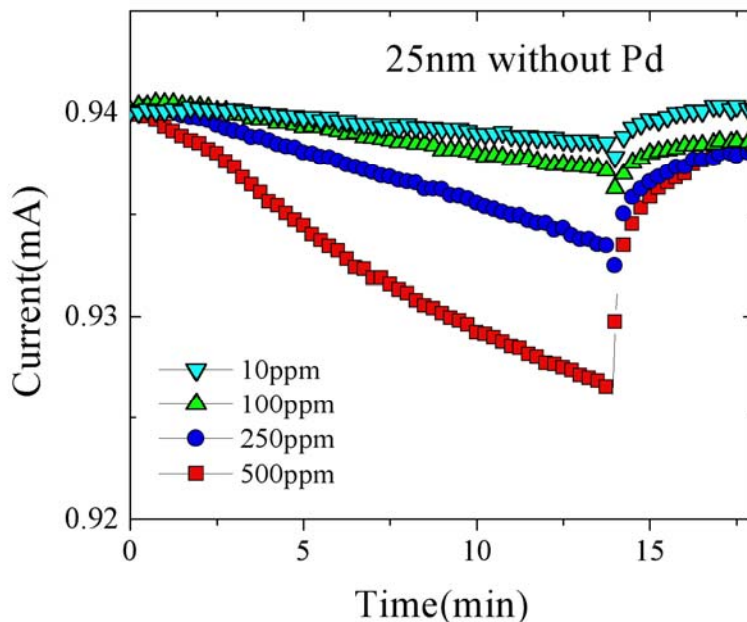


Figure 6-7: Current vs. time measurement for 25nm sensor exposed to different H₂ concentrations..

6.4.2 SWCNT Samples Coated with Sputtered Pd

The three sputter coated samples listed in Table 6-1 were tested for their response to hydrogen (Figures 6-8, 6-9, and 6-10). Again, the current vs. time for a 0.5 V bias was monitored during exposure to hydrogen. The samples were exposed to air at $t=14$ min to recover their nearly original conductance. A summary of $\Delta I/I$ at $t=14$ min and 500 ppm H₂ concentration is listed in Table 6-3.

The Pd coated sensors all show decreased conductance upon exposure to H₂. The 7 nm film shows the highest sensitivity while the micro-device sensor shows the lowest. Optimization of the sensitivity would occur by finding the optimum ratio of Pd to SWCNTs. The micro-device sensor appears to have too much Pd for the amount of nanotubes while the 25 nm film probably doesn't have enough.

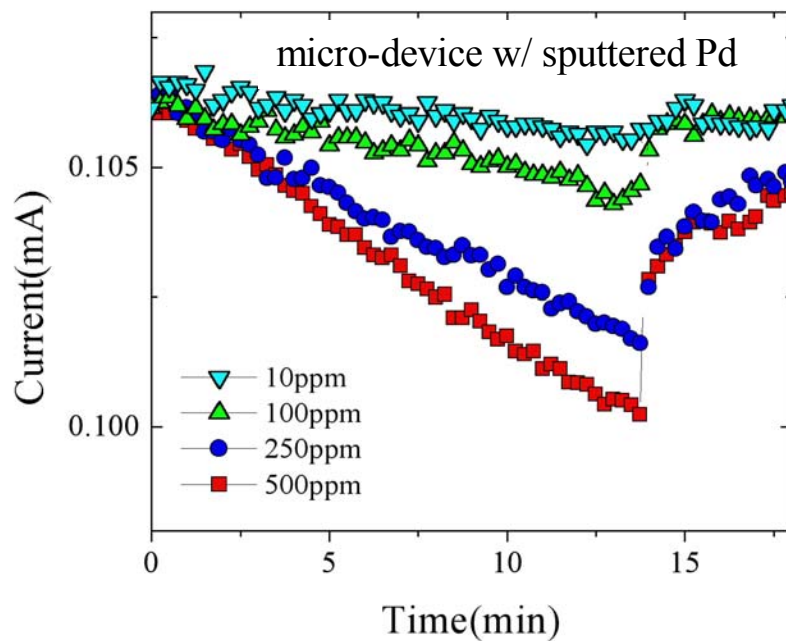


Figure 6-8: Current vs. time for micro-device sensor with sputtered Pd for different H_2 concentrations.

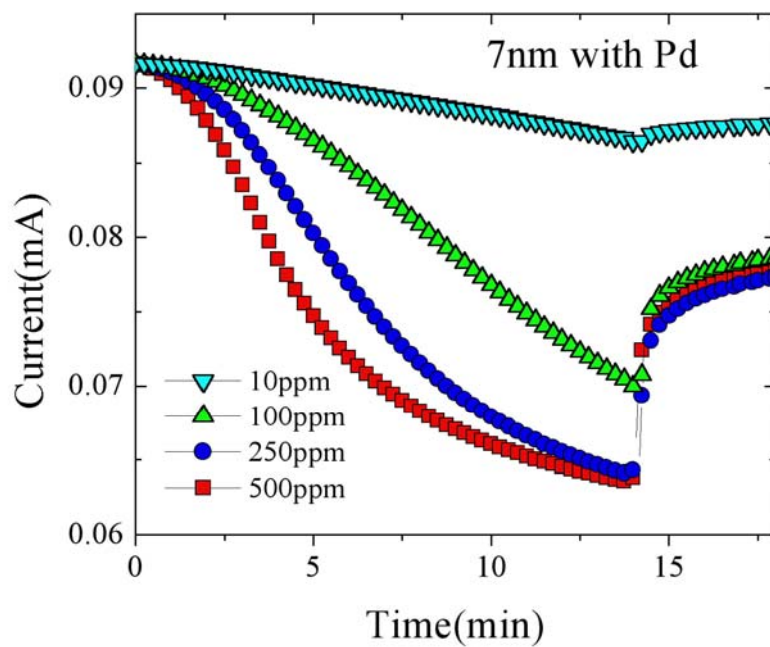


Figure 6-9: Current vs. time for 7 nm film with sputtered Pd for different H_2 concentrations

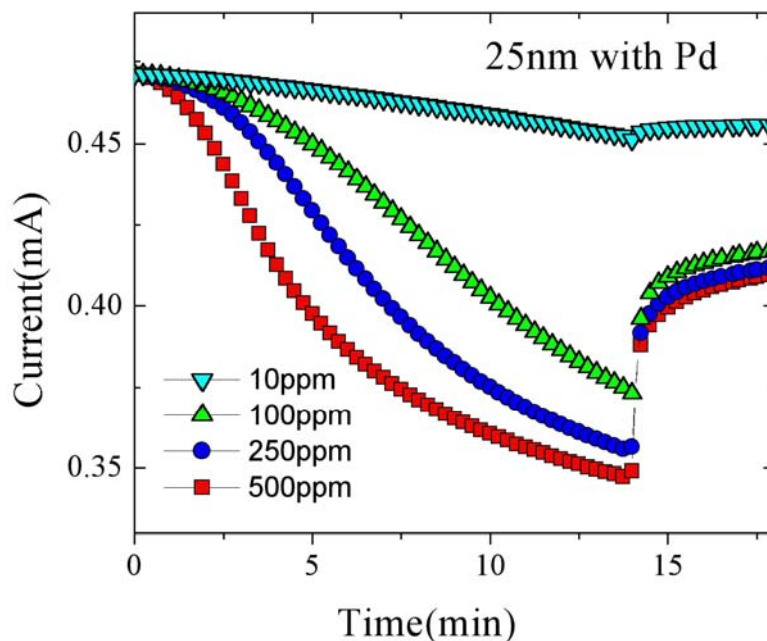


Figure 6-10: Current for time for 25 nm film with sputtered Pd for different H₂ concentrations.

Table 6-3: Conductance changes in sputtered Pd/SWCNT samples at t=14 min for 500 ppm H₂.

Sample	$\Delta I/I$ (%)
Micro-device	5.6
7 nm film	30.
25 nm film	25.9

6.4.3 SWCNT Samples Coated with Thermally Evaporated Pd

A 7nm film with a non-percolating layer of thermally evaporated Pd was tested for H₂ sensitivity. The current vs. time graph for 500ppm H₂ and 0.5V bias voltage is shown in Figure 6-11. The total change in resistance is 24%, which is smaller than the sputtered Pd/7nm film sample (30.4%). However, the response rate is much faster. Within one minute this sample shows a change in conductance of 12% (50% of the total change). At t=5 minutes the current has changed by 23% (96% of the total change). By comparison

the sputtered 7nm film shows a $\Delta I/I$ of only 1.2% (or 3.9% of the total change) at $t=1$ minute. After 5 minutes the change is 18.5% (60.9% of the total resistance change).

The recovery rate is also much faster. One minute after exposure to air the thermally evaporated Pd/SWCNT sample recovers 77.4% of the H_2 induced conductance change. After 5 minutes the recovery is 95%. The sputtered Pd/SWCNT sample only recovers 35.9% after 1 minute and 45.7% after 5 minutes. The differences in the total change between the sputtered and evaporated samples might be due to different amounts of Pd. The rapid response of the evaporated Pd/SWCNT film makes it a more promising candidate for real world applications. Optimizing the amount of Pd might increase its sensitivity to match the sputter Pd/SWCNT sensor.

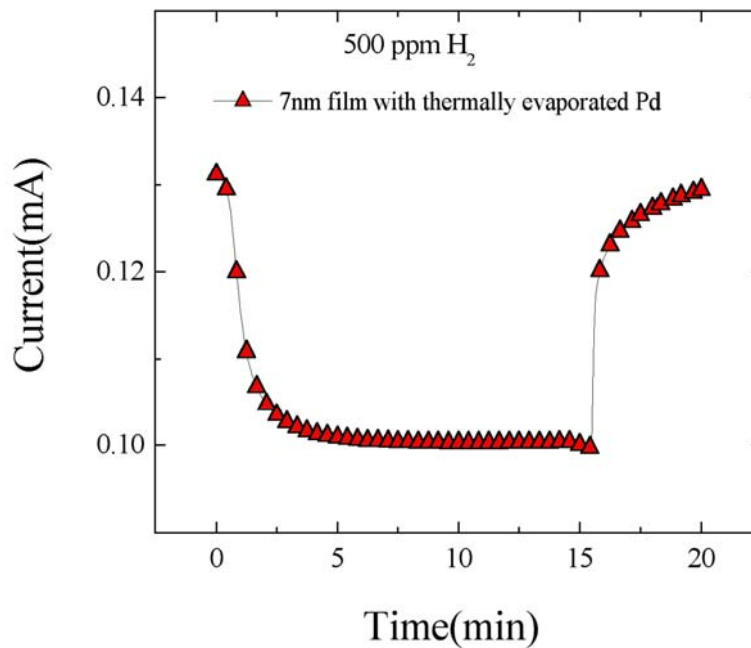


Figure 6-11: Current vs. time for 7nm film with thermally evaporated Pd exposed to 500ppm of H_2 .

6.4.4 Thin Pd Film

The current vs. time was monitored for a very thin layer of thermally evaporated Pd to 500ppm of H_2 , Figure 6-12. The initial resistance of the film was 55.6 k Ω . The current first increased and then decreased upon exposure to H_2 . After the sample was exposed to air the current increased again, without recovery of the initial resistance. These results are very different than those exhibited by the Pd/SWCNT samples. From this we can conclude that the effects seen in the Pd/SWCNT samples are due to changes in the resistance of the nanotubes and are not simply an effect caused by changes in the Pd resistance.

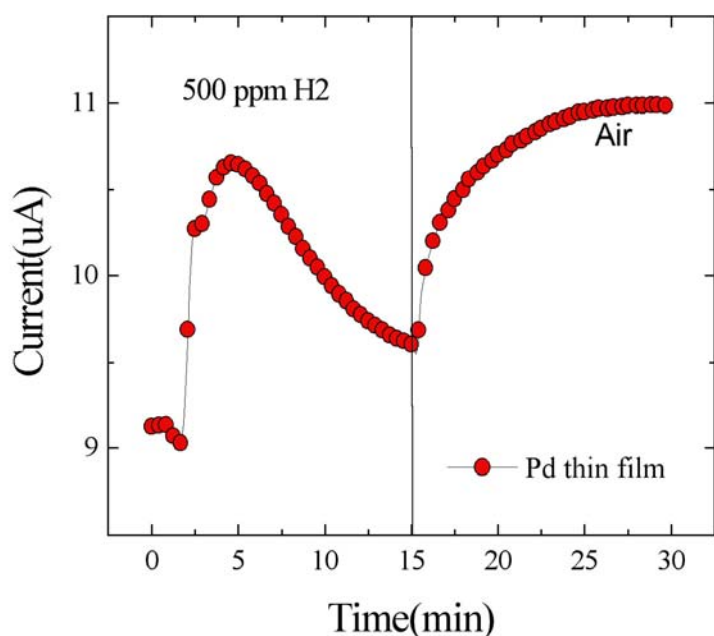


Figure 6-12: Current versus time for a thin Pd film.

6.4.5 Conclusion

Carbon nanotubes coated with Pd have been shown to be sensitive to H_2 levels as low as 10ppm within 10 minutes exposure. Although nanotube samples with Pd deposited by

both sputtering and thermal evaporation show sensitivity to H_2 , the latter shows a much faster response and recovery. It has been shown that nanotubes subjected to sputtered deposition of metals exhibit a decrease in their conductance, likely due to damage.

APPENDIX

SPECTROELECTROCHEMICAL STUDY OF CARBON NANOTUBE THIN FILMS

Spectroelectrochemistry is a field of study which combines spectroscopy with electrochemistry. Spectroelectrochemistry can provide valuable information about thin films, such as the effects of different applied voltages on the optical transmittance of the thin film. Aqueous electrolyte is commonly used in many electrochemical applications. However, water is not ideal in spectroelectrochemistry because it has strong absorption bands which make it almost impossible to gain information about a thin film at certain wavelengths. Additionally, water has a narrow potential window. Water can only be taken to -0.81V or +1.23V before it breaks down into its byproducts (H_2 gas and OH^- ions at negative voltage, O_2 gas and H^+ ions at positive voltage).⁷⁷ To circumvent these types of problems, a nonaqueous solvent must be used.

The experiment was performed using the nonaqueous solvent acetonitrile. And involved a SWCNT thin film. In this experiment potentials were applied to the thin film (versus a platinum wire counter electrode using a silver wire pseudoreference electrode) while changes in the transmittance spectrum were monitored. We infer that these changes in the spectrum occur as a consequence of changes in the Fermi level. From this inference, we are able to locate the intrinsic doping level of the semiconducting nanotubes.

A chemically resistant cell and identical reference cell were developed for use in these experiments. One of these cells is displayed in Figure A-1. The bodies of the cells are composed of Teflon®. They use Simriz® SZ485 O-rings and have quartz optical

windows. All of these components have high chemical resistances to most substances. Nylon tubing was used for getting solutions into and out of the cells. Additionally, Teflon® valves were used to control the flow of the solution, and a steel poppet valve was attached so that any gasses produced would be able to leave the cells without allowing atmospheric contaminants to enter. There were three types of electrodes used in the cell. The working electrode was the film under study contacted by a graphite rod, the counter electrode was platinum, and the reference electrode was silver. A Perkin-Elmer {model} potentiostat supplied the potentials in a three terminal set-up, where in the counter electrode voltage is varied to make the voltage difference between the working electrode and reference electrode the desired value. The benefit of this is that the desired potential on the working electrode is maintained versus a well-defined reference independent of any Faradaic electron transfer occurring at the working electrode. The cells were designed in an attempt to keep out water vapor and air. The cells served their purpose well, and substantial impurity peaks were only observed after the cells were exposed to the environment for periods of over 24 hours.

A.1 Carbon Nanotube Experiment

When taking a transmittance spectrum of a thin film of SWCNTs one observes three broad peaks. Our study focuses on the peak centered at 1650nm. This peak corresponds to photons absorbed during electronic transitions from the highest occupied semiconducting valence band (V1) to the lowest unoccupied semiconducting conduction band (C1).

Figure A-2 shows that the valence and conduction states for carbon nanotubes have sharp peaks in the density of states known as Van Hove singularities. This would imply very sharp absorption bands. However, a thin film of SWCNTs is composed of

semiconducting nanotubes of different diameters and chiralities. As a result of this assortment of types of nanotubes, the peaks in the transmittance spectrum end up being broad and smooth.

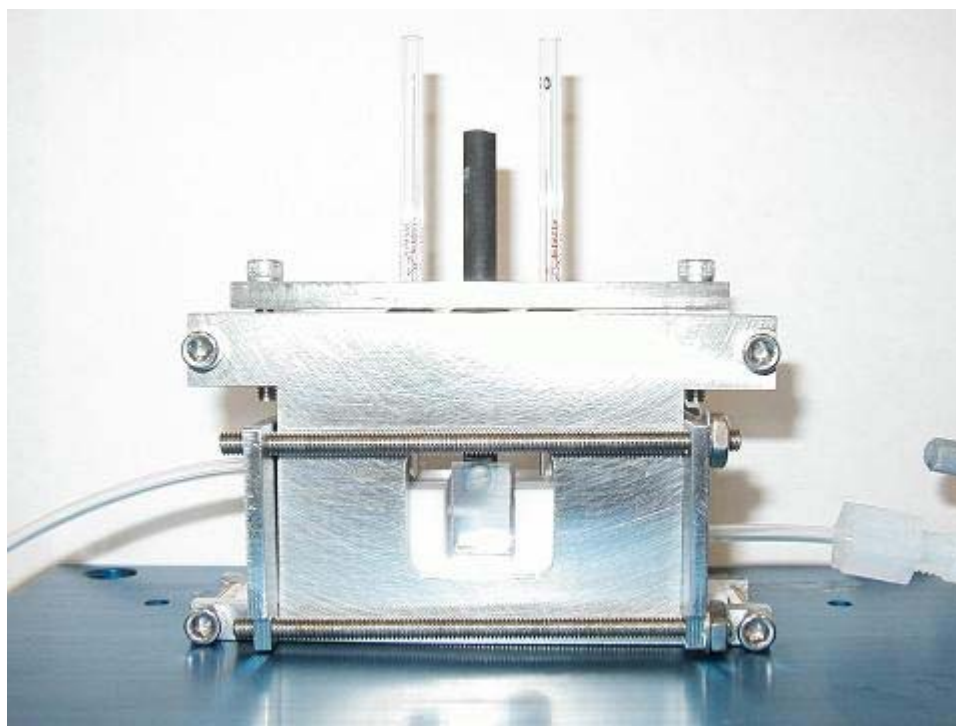


Figure A-1: The spectroelectrochemical cell used in the experiments.

By applying a voltage to the SWCNT sample, one can shift the Fermi level. One can see in Figure A-2a that if the valence state (V1) becomes more depleted, then fewer electrons will be available to undergo the transition to the conduction state (C1). Therefore there will be less absorption of photon energy, and the absorbance peak will diminish. Similarly, if the Fermi level is increased, as in Figure A-2b, so that some electrons already occupy the conduction state (C1), then there will be fewer available states for the remaining valence state electrons to move into and the peak will also diminish. Based on this knowledge, one can then determine the intrinsic doping level of the semiconducting nanotubes. If the peak is largest at 0V then the semiconducting

nanotubes will be intrinsically undoped. Using this method, one can only determine the amount of doping qualitatively.

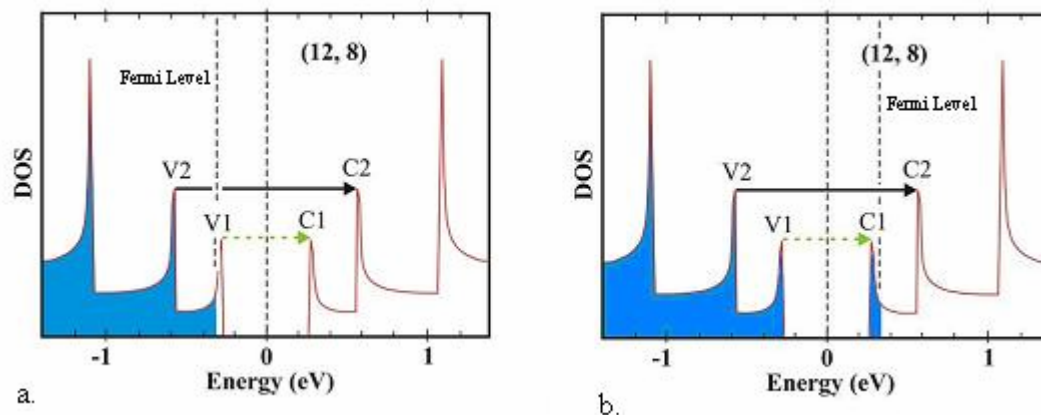


Figure A-2: Diagram of the Fermi Level of a semiconducting (12,8) SWCNT which is a) p-doped or b) n-doped

A.2 Experimental Section

This experiment is similar in nature to an experiment performed by Kavan *et al.*⁷⁸ Our experiment mainly differs from that one in that the SWCNT thin film that we use is mounted directly on quartz instead of ITO (Indium Oxide doped with Tin Oxide). We can do this because the nanotube samples also contain metallic nanotubes and we have learned how to make ultrathin (and hence transparent) films of SWCNTs that are in contiguous electrical contact with each other.⁶⁹

A SWCNT film was prepared and attached to a piece of quartz. This sample was baked in flowing argon gas in a Thermolyne 79300 tube furnace to drive off chemical dopants. The temperature was ramped at 5°C per minute until it reached 110°C, stayed at 110°C for 30 minutes, and then ramped at 1°C per minute to 600°C. The temperature remained here for 2 hours. A reference piece of quartz was also baked in the same way to be used in a reference cell.

Once the two pieces of quartz were allowed to cool, they were removed from the tube furnace and attached to the graphite working electrodes inside the electrochemical cell and reference cell described in the introduction. Next, both cells were heated to 75°C under flowing argon atmosphere for approximately 24 hours. Upon removal from the tube furnace, the cells were sealed by closing their Teflon® valves. The cells were then placed inside of an argon glove box and allowed to remain in there for 24 more hours with their valves open. This argon glove box had 1-2ppm oxygen.

Inside the argon glove box, the solvent and electrolyte were added to the two cells. The solvent we used was Acetonitrile obtained from Fisher Scientific, and the electrolyte was 0.5 M LiBF₄. This solution was also placed inside glass tubes which held the reference and counter electrodes. Once the solvent and electrolyte were added, the cells were resealed, and removed from the argon glove box. Potentials were applied with a Perkin-Elmer Model 283 Potentiostat, while transmission spectra were recorded with a Perkin-Elmer Lambda 900 UV/Vis/NIR spectrometer. With the reference cell (no nanotube film but including the quartz plate, cell windows and electrolyte) in the reference beam of the spectrometer, and the sample cell in the sample beam, the absorbance of the sample cell itself (windows, electrolyte, quartz substrate) could be normalized out, leaving only the spectrum of the nanotube film.

A.3 Results and Discussion

Voltage was only applied to the cell with the nanotube thin film. We applied voltages ranging from -1.0V to +0.8V and recorded their spectra. The spectra observed at positive voltages are displayed in Figure A-3, and the spectra at negative voltages are displayed in Figure A-4. As can be seen in Figure A-3, the transmittance peak is smaller at +0.2V than it is at 0.0V. However, one can see in Figure A-4 that the peak size is the

greatest at -0.4V. After +0.2V and -0.6V the transmittance peaks change dramatically with a change in voltage.

One problem encountered with the two cells was that they were not exactly the same thickness. We could only minimize the difference to within 0.2mm. This variance caused some acetonitrile peaks to show up in the spectra. Since these peaks were the same in all spectra, they were removed and the figures were smoothed prior to presentation in Figures. A-3 and A-4.

A.4 Conclusions

We determined that the maximum size of the transmittance peak occurs at -0.4V. At this voltage, the Fermi level is in the band gap between the first valence state and first conduction state of the most semiconducting nanotubes. This conclusion indicates that at 0.0V, the Fermi level has been shifted toward the positive side. Therefore the nanotube film is intrinsically slightly p-doped.

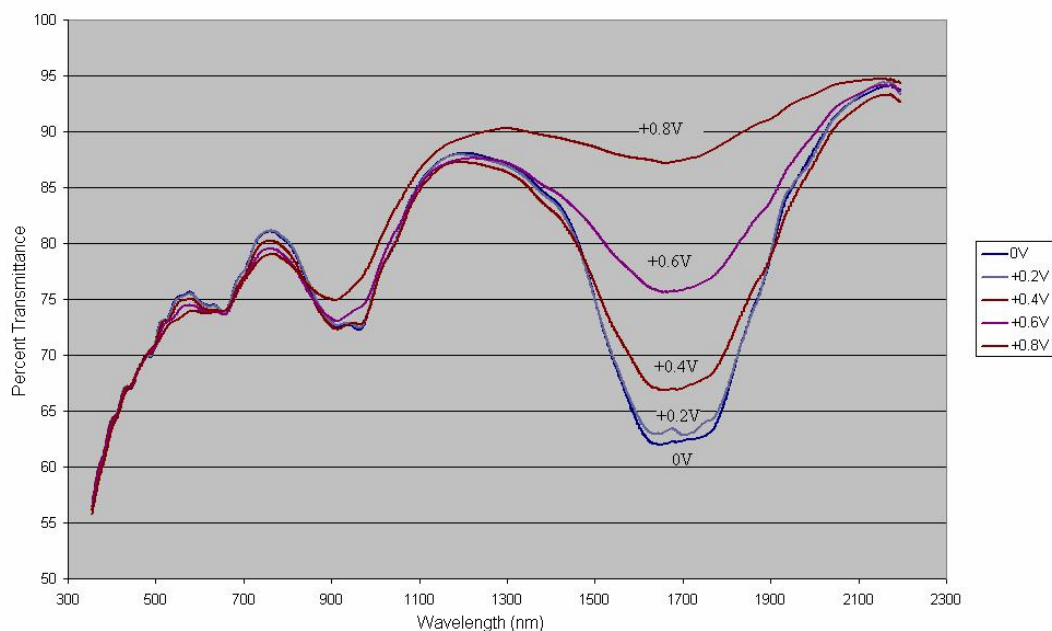


Figure A-3 Percent Transmittance vs. Wavelength for SWCNT thin-film at various positive applied potentials.

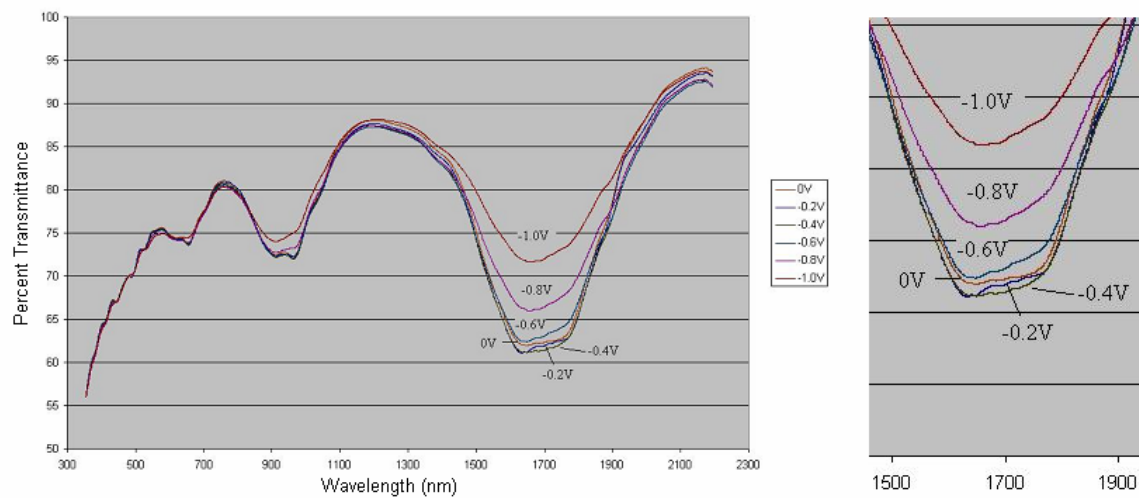


Figure A-4: Percent Transmittance vs. Wavelength for SWCNT thin-film at various negative applied potentials.

LIST OF REFERENCES

1. S. Iijima, *Nature* **354**, 56 (1991)
2. D.S. Bethune, C.H. Kiang, M.S. de Vries, G. Gorman, R. Savoy, J. Vazques. and R. Beyers,. *Nature* **363**, 605 (1993)
3. S. Iijima and T. Ichihashi, *Nature* **363**, 603 (1993)
4. L.X. Zheng, M.J. O’Connel, S.K. Doorn, X.Z. Liao, Y.H. Zhao, E.A. Akhadov, M.A. Hoffbauer, B.J. Roop, Q.X. Jia, R.C. Dye, D.E. Peterson, S.M. Huang, J. Liu, and Y.T. Zhu, *Nature Mat.* **3** 673 (2004)
5. M.M.J. Treacy, T.W. Ebbesen, and J.M. Gibson, *Nature* **381** 678 (1996)
6. H.D. Wagner, O. Lourie, Y. Feldman, and R. Tenne, *Appl. Phys. Lett.* **72** 188 (1998)
7. D.A. Walters, L.M. Ericson, M.J. Casavant, J. Liu, D.T. Colbert, K.A. Smith, and R.E. Smalley, *Appl. Phys. Lett.* **74** 3803 (1999)
8. R. Baughman, C. Cui, A. Zakidov, Iqbal, J. Barisci, G. Spinks, G. Wallace, A. Mazzoldi, D. De Rossi, A. Rinzler, O. Jaschinski, S. Roth, and M. Kertesz, *Science* **284**, 1340 (1999)
9. A. Thess, R. Lee, P. Nikolaev, H.J. Dai, P. Petit, J. Robert, C.H. Xu, Y.H. Lee, S.G. Kim, A.G. Rinzler, D.T. Colbert, G.E. Scuseria, D. Tomanek, J.E. Fischer, and R.E. Smalley, *Science* **280**, 483 (1996)
10. Y. Li, W. Kim, Y. Zhang, M. Rolandi, D. Wang, and H. Dai, *J. Phys. Chem. B.* **105** 11424 (2001)
11. N.R. Franklin, Y. Li, R.J. Chen, A. Javey, and H. Dai, *Appl. Phys. Lett.* **79** 4571 (2001)
12. P. Nikolaev, M.J. Bronikowski, R.K. Bradley, F. Rohmund, D.T. Colbert, K.A. Smith, and R.E. Smalley, *Chem. Phys. Lett.* **313**, 91 (1999)
13. M.S. Dresselhaus, G. Dresselhaus, and R. Saito, *Phys. Rev. B.* **45** 6234 (1992)
14. J.W. Mintmire, B.I. Dunlap, and C.T. White, *Phys. Rev. Lett.* **68** 631 (1992)
15. N. Hamada, S. Sawada, and A. Oshiyama, *Phys. Rev. Lett.* **68** 1579 (1992)

16. J.W.G Wildoer, L.C. Venema, C. Dekker, A.G. Rinzler, and R.E. Smalley, *Nature* **391**, 59 (1998)
17. T. Odom, P. Kim, J.-L. Huang, and Ch. Lieber, *Nature* **391**, 62 (1998)
18. R. Saito, G. Dresselhaus, and M.S. Dresselhaus, *Physics Properties of Carbon Nanotubes* (Imperial College Press, London 1998)
19. D. Nixon and G. Parry, *J. Phys. C* **2**, 1732 (1969)
20. M.E. Preil, J.E. Fischer, S.B. Diczko, and G. K. Wertheim, *Phys. Rev. B* **30**, 3536 (1984)
21. J.E. Fischer, H.J. Kim, and V.B. Cajipe, *Phys. Rev. B* **36**, 4449 (1987)
22. F. Baron, S. Flandrois, C. Hauw, and J. Gaultier, *Solid State Commun.* **42**, 759 (1982)
23. R.S. Markiewicz, J.S. Kasper, and V. Interrante, *Synth. Met.* **2**, 363 (1980)
24. Y. Murakami, T. Kishimoto, H. Suematsu, *J. Phys. Soc. Jpn.* **59**, 571 (1990)
25. L. Pietronero and S. Strassler, *Phys. Rev. Lett.* **47**, 593 (1981)
26. M. Kertesz, *Mol.Cryst. Liq. Cryst.* **125**, 103 (1983)
27. M. Kertesz, F. Vonderviszt, and R. Hoffman, *Intercalated Graphite* (Elsevier, New York, 1983) p. 141
28. C. Chan, W. Kamitakahara, K. Ho, and P. Eklund, *Phys. Rev. Lett.* **58**, 1528 (1987)
29. Y.N. Gartstein, A.A Zakhidov, and R.H. Baughman, *Phys. Rev. Lett.* **89**, 045503 (2002)
30. Y.N. Gartstein, A.A. Zakhidov and R.H. Baughman, *Phys. Rev. B* **68** 115415 (2003)
31. M. Verissimo-Alves, B. Koiller, H. Chacham, and R.B. Capaz, *Phys. Rev. B* **67** 121401 (2003)
32. G. Sun, J. Kürti, M. Kertesz, and R. Baughman, *J. Am. Chem. Soc.* **124**, 15076 (2002)
33. G. Sun, J. Kürti, M. Kertesz, and R. Baughman, *J. Phys. Chem. B* **107**, 6924 (2003))
34. A. G. Rinzler, J. Liu, H. Dai, P. Nikolaev, C.B. Huffman, F.J. Rodrigues-Macia, P.J. Boul, A.H. Lu, D. Heymann, D.T. Colbert, R.S. Lee, J.E. Fischer, A.M. Roa, P.C. Eklund, and R.E. Smalley, *Appl. Phys. A* **67**, 29 (1998)

35. J. Bahr, E. Mickleson, M. Bronikowski, R. Smalley, and J. Tour, *Chem. Commun.*, 193 (2001)
36. J. Liu, A.G. Rinzler, H. Dai, J. Hafner, R.K. Bradley, P.J. Boul, A. Lu, T. Iverson, K. Shelimove, C.B. Huffman, F. Rodriguez-Macias, Y.S. Shon, T.R. Lee, D.T. Colbert, and R.E. Smalley, *Science* **280** 1253 (1998)
37. M.F. Islam, E. Rojas, D.M. Bergey, A.T. Johnson, and A.G. Yodh, *Nano Lett.* **3**, 269 (2003)
38. J. Hafner, C. Cheung, T. Oosterkamp, and C. Lieber, *J. Phys. Chem. B* **105**, 743 (2001)
39. Y. Li, W. Kim, Y. Zhang, M. Rolandi, D. Wang, and H. Dai, *J. Phys. Chem. B* **105**, 11424 (2001)
40. A. Patil, J. Sippel, G.W. Martin, and A.G. Rinzler, *Nano Lett.* **4** 303 (2004)
41. M. Tortonese and M. Kirk, *SPIE Micromachining and Imaging* **3009** (1997)
42. M. Shim, A. Javey, N.W.S. Kam, and H. Dai, *J. Am. Chem. Soc.* **123** 11512 (2001)
43. M. Krüger, M.R. Buitelaar, T. Nussbaumer, and C. Schönenberger, *Appl. Phys. Lett.* **78** 1291 (2001)
44. S. Rosenblatt, Y. Yaish, J. Park, J. Gore, V. Sazonova, and P. McEuen, *Nano Lett.*, **2** 869 (2002)
45. E. Gileadi and M. Urbakh, *Thermodynamics and Electrified Interfaces* (Wiley-VCH, 2002)
46. J.B. Hasted, D.M. Ritson, and C.H. Collie, *J. Chem. Phys.* **16** 1 (1948)
47. F. Booth, *J. Chem. Phys.* **19** 391 (1951)
48. R. Pottel, *Water, A Comprehensive Treatise* edited by F. Franks (Plenum Press, New York, 1973) Chapter 8.
49. A. Kemper, H.H.P. Gommans and A.G. Rinzler, unpublished result
50. S. Tans, A. Verschuere, and C. Dekker, *Nature* **393** 49 (1998)
51. R. Martel, T. Schmidt, H. Shea, T. Hertel, and Ph. Avouris, *Appl. Phys. Lett.* **73** 2447 (1998)
52. C. Zhou, J. Kong, and H. Dai, *Appl. Phys. Lett.* **76** 1597 (2001)
53. R. Martel, V. Derycke, C. Lavoie, J. Appenzeller, K. K. Chan, J. Tersoff, and Ph. Avouris, *Phys. Rev. Lett.* **87** 256805 (2001)

54. A. Javey, J. Guo, Q. Wang, M. Lundstrom and H. Dai, *Nature* **424** 654 (2003)
55. J.-P. Radin and E. Yeager, *Electroanal. Chem. Interfacial Electrochem.* **36** 257 (1972)
56. H. Gerischer, R. McIntyre, D. Scherson, and W. Storck, *J. Phys. Chem.* **91** 1930 (1987)
57. Y. Oren, I. Glatt, A. Livnat, O. Kafri, and A. Soffer, *J. Electroanal. Chem.* **187** 59 (1985)
58. J. Kong, N.R. Franklin, C. Zhou, M.G. Chapline, S. Peng, K. Cho, and H. Dai, *Science* **287** 622 (2000)
59. P.G. Collins, K. Bradley, M. Ishigami, and A. Zettl, *Science* **287** 1801(2000).
60. J. Kong and H. Dai, *J. Phys. Chem. B* **105** 2890 (2001)
61. G.U. Sumanasekera, B.K. Pradhan, H.E. Romero, K.W. Adu, P.C. Eklund, *Phys. Rev. Lett.* **89** 166801 (2002)
62. K. Bradley, J-C P. Gabriel, A. Star, and G. Grüner, *Appl. Phys. Lett.* **83**, 3821 (2003)
63. J.P Novak, E.S. Snow, E.J. Houser, D. Park, J.L. Stepnowski, and R.A. McGill, *Appl. Phys. Lett.* **83** 4026 (2003)
64. Y. Lu, J. Li, J. Han, H.-T. Ng, C. Binder, C. Partridge and M. Meyyappan, *Chem. Phys. Lett* **391** 344 (2004)
65. I. Sayago, E. Terrado, E. Lafuente, M.C. Horrillo, W.K. Maser, A.M. Benito, R. Navarro, E.P. Urriolabeitia, M.T. Martinez and J. Gutierrez, *Synth. Met.* **148** 15 (2005)
66. A. Barr, *Thin Solid Films* **41** 217 (1977)
67. F. Wu and J.E. Morris, *Thin Solid Films* **246** 17 (1994)
68. J.E. Morris, A. Kiesow, M. Hong and F. Wu, *Int. J. Electronics* **81** 441 (1996)
69. Z. Wu, Z. Chen, X. Du, J.M. Logan, J. Sippel, M. Nikolou, K. Kamaras, J.R. Reynolds, D.B. Tanner, A.F. Hebard and A.G. Rinzler, *Science* **305**,1273 (2004)
70. W. Liang, M. Bockrath, D. Bozovic, J. Hafner, M. Tinkham, and H. Park, *Nature* **411** 665 (2001)

- 71. M.S. Fuhrer, J. Nygard, L. Shih, M. Forero, Y.-G. Yoon, M.S.C. Mazzoni, H. J. Choi, J. Ihm, S. G. Louie, A. Zettl, and P.L. McEuen, *Science* **288** 494 (2000) H.W.Ch. Postma, M. de Jonge, Z. Yao, and C. Dekker, *Phys. Rev. B.* **62** R10653 (2000) J.W. Park, J. Kim and K.-H. Yoo, *J. Appl. Phys.* **93** 4191 (2003)
- 74. S. Dag, O. Gülseren, S. Ciraci, and T. Yildirim, *Appl. Phys. Lett.* **83** 3180 (2003)
- 75. J. Nygard, D.H. Cobden, M. Bockrath, P.L. McEuen, and P.E. Lindelof, *Appl. Phys. A.* **69** 297 (1999)
- 76. R. Anton, *Thin Metal Films and Gas Chemisorption*, edited by P. Wissmann (Elsevier, New York, 1987) Chap. 1, p. 3.
- 77. K. Izutsu. *Electrochemistry in Nonaqueous Solutions* (Wiley-Vich, Weinheim, 2002)
- 78. L. Kavan, P. Rapt, L. Dunsch, M.J. Bronikowski, P. Willis, and R.E. Smalley, *J. Phys Chem. B.* **105** 10764(2001)

BIOGRAPHICAL SKETCH

Jennifer was born May 28th, 1977 in Spencer, Iowa to Rick and Cindy Sippel. Jennifer developed an interest in science early on and was greatly influenced by her father's interest in astronomy. She has always been curious about understanding how the universe, and everything in it, works. This led her to the University of Iowa after graduating from Ames High School. At the University of Iowa she earned a double major B.S. in both physics and astronomy. As an undergraduate she studied eclipsing binary star systems under Dr. Robert Mutel and also worked from him as an operator of the university's Automated Telescope Facility. She also did research for Dr. Steven Spangler and operated a 4.5m radio telescope under his tutelage.

In between her junior and senior years in college Jennifer participated in the Walt Disney World college program. She took a break from research for a summer to work at the Magic Kingdom in Orlando, Florida telling bad jokes on the Jungle Cruise attraction. Jennifer immensely enjoyed this experience and it prompted her to look into coming to Florida for graduate school.

Jennifer started her graduate program in Physics at the University of Florida in the fall of 1999. She began working for Dr. Andrew Rinzler during the summer of 2000 studying carbon nanotubes. She has enjoyed working with these fascinating materials and learning many instrumentation skills during the course of her research.

While at the University of Florida Jennifer met Garrett Oakley. He was a fellow graduate student but in the field of Chemistry. They were married on the beach in October of 2004.